

**Robust high resolution models of the continental lithosphere:
Methodology and application to Asia**

Robuuste hoge resolutie modellen van de continentale lithosfeer:
Methode en toepassing in Azië
(met een samenvatting in het Nederlands)

Proefschrift

ter verkrijging van de graad van doctor aan de Universiteit Utrecht op gezag
van de rector magnificus, prof.dr. G.J. van der Zwaan, ingevolge het besluit
van het college voor promoties in het openbaar te verdedigen op maandag 9
september 2013 des middags te 2.30 uur

door

Ward Stolk

geboren op 20 februari 1985

Amersfoort

Promotor: Prof.dr. S.A.P.L. Cloetingh

Co-promotoren: Dr. W.W.W. Beekman
Dr. M.K. Kaban

This thesis was accomplished with financial support from the Netherlands Space Office (NSO).

A geologist, a geophysicist and a modeller travel to a conference together. At some point the question arises as to what is the answer to 4 times 2. The geologist is of the opinion that the answer lies somewhere between 7.5 and 9. The geophysicist states the answer is 7.956831. The modeller remains quiet for a very long time. When asked what he thinks, he exclaims: 'I can't figure it out, just tell me what the answer is supposed to be and I will make it work.'

Members of the Assessment Committee

Prof.dr. E.B. Burov	UPMC (Paris IV), France
Prof.dr. F.D. van der Meer	University of Twente, The Netherlands
Dr. W.D. Mooney	US Geological Survey, United States
Prof.dr. J.D.A.M. van Wees	Utrecht University, The Netherlands
Prof.dr. M.J.R. Wortel	Utrecht University, The Netherlands

The research on which this thesis is based was carried out at:

*The Netherlands Research Centre for Integrated Solid Earth Science (ISES),
Utrecht University, Faculty of Geosciences, The Netherlands*

*Helmholtz Centre Potsdam, GFZ German Research Centre for Geosciences, Sec-
tion 1.3, Potsdam, Germany*

ISBN: 978-90-6266-331-6

© 2013 Ward Stolk

This book is in copyright. No reproduction without permission of the author.
All rights reserved.

Printed by Wöhrmann Print Service, Zutphen

Cover: View from the Laken Pass, Tibet, at 5190m altitude

Contents

Acknowledgements	vii
Summary	xi
Samenvatting	xv
1 Introduction	3
1.1 Thesis outline: A top-down approach	3
1.2 Geology of the Asian continent	4
1.3 Funding and support	5
2 Datasets used in this study	9
2.1 Topography	9
2.2 Sediment thickness model	11
2.3 Seismic data	11
2.4 Seismic tomography data of the mantle	13
2.5 Gravitational data	22
3 Sediment velocity and density model	25
3.1 Velocity-depth relation in sedimentary cover	25
3.2 Division into regions and function fitting	26
3.3 Analysis of results	26
4 Depth to Moho	35
4.1 Remove isostatic topographic effect	35
4.2 Compute residual depth to Moho on regular grid	38
4.3 Restore topographic adjustment	38
4.4 Quality control	41
4.5 Discussion of Results	41
5 Crustal P-wave velocities	49
5.1 Phase 1: Normalizing depths	49
5.2 Phase 2: Determination of boundary depths	50
5.3 Phase 3: Determination of velocity profiles	52
5.4 Phase 4: Correction for average velocity	52
5.5 A new crustal velocity model for Asia	52
5.6 Statistical analysis	56
5.7 Conversion to density	58

6 Thermal, density and compositional model of the lithospheric mantle	63
6.1 Temperature and density modelling	63
6.1.1 Mineral properties	66
6.1.2 Voigt-Reuss-Hill averaging	70
6.1.3 Anelasticity correction	70
6.2 Forward gravity field modelling	72
6.2.1 Theory of gravity field modelling	72
6.2.2 Evaluation of the Green's function for earth	73
6.3 Mantle gravity anomalies	76
6.4 Compositional changes	77
6.4.1 Composition, density and temperature	78
6.4.2 Updating composition	79
6.5 Results	83
7 Models of lithospheric strength: A first assessment	93
7.1 Rheology of the lithosphere	93
7.1.1 Brittle failure	95
7.1.2 Viscous creep	95
7.2 Strength of the Asian lithosphere	97
7.3 Uncertainties in strength modelling	104
7.4 Future outlook	111
A Data binning	113
B Coefficient of determination	115
C Ordinary Kriging	117
C.1 Assumptions	117
C.2 Experimental covariogram and covariogram model	118
C.3 The Ordinary Kriging scheme	119
C.4 Considerations on the use of Ordinary Kriging	121
Nomenclature	127
About the author	129
Bibliography	130

Acknowledgements

Strange it is to start a thesis with something that is written last. It falls out of pace with the rest of the thesis, since it does not describe the results of the research, nor does it describe the road that led to these results. It is an account of the people met along the way. Some of them are fellow travellers, aiming to finish their own PhD's, others are acquaintances, only briefly met at the wayside inn, but with whom I had fruitful discussions none the less. Then there are those that have provided guidance, those who have shown which paths to pursue. It is these latter that I would like to acknowledge first.

On a drowsy autumn day in 2008 I received an e-mail from Mikhail Kaban, who had been my supervisor during an internship at the GeoForschungsZentrum in Potsdam, Germany, a year before. The e-mail came down to the following: 'We are starting a new project together with Sierd Cloetingh, would you care to apply?' Though I was at that time still working on my master thesis, I had thought a bit about life after graduation and the project fitted my ideas. It turned out to be the right choice. Over the years the guidance given by Mikhail proved to be the most fruitful input into my research and without it this thesis would not be lying in front of you. I wish to thank you for the many discussions we have had and for putting up with my stubbornness, which must have given you quite a headache from time to time.

Little after Mikhail's e-mail, I found myself in an office with Fred Beekman, a good natured, open and helpful fellow, with usually too much work on his plate. It was a pleasant meeting. In the end I was offered the job and did not hesitate to take it. Over the years Fred has been a mentor, who not only gave me input for my research, but also taught me how to write abstracts and articles, make posters, and present myself at conferences. I have learned from you the second most important thing in science, how to sell yourself and your work.

In the same hour that I met Fred, I also briefly met Sierd. Somehow, you meet him briefly most of the time, busy man as he is. However he was around and took his time when it was needed, reading manuscripts and giving valuable suggestions. Another upshot of such an active professor to lead the group is that it offers an enormous amount of opportunities in international contacts. Furthermore, in Dimi, Ernst, Liviu and Fred he acquired around him a strong team to guide the Tectonics group. Sierd, your speeches will not soon be forgotten.

During my frequent stays at the GFZ in Potsdam, I always shared an office with Magdala Tesauero. She had finished her PhD on the European lithosphere more or less when I started mine on the Asian lithosphere. If I have been able to improve over your methodology it was because you kindly provided me with all your programs, knowledge and work of past and current years, preventing me from having to reinvent the wheel. Other colleagues at the GFZ with whom

I shared many a meal and discussion include Roelof, Indridi, Maiko, Christoph (Förste), Franz, Sveta, Jürgen, Hartmut, and the always helpful secretary Angelika. Then there are those colleagues of 'the new Sektion 1.3', to which Mischa, Magdala en I were moved after reorganizations at the GFZ: Inga, Robert, Henryk, Jan, Volker, Hannes, Julian, Christof (whom I had previously met during my studies in Delft), Alexey, Irina (with whom I shared an office in my last year of the PhD, five years after first sharing an office with her during my internship), Ingo, Jan, Sara, Tobias, Ronny, Liangjing, and Veronika. The cries of 'Kaffee, Kaffee' down the hallway will be remembered. A special thank you to Maik Thomas, whom, apart from being a good colleague and leader of the 'new' Sektion 1.3, invited me to accompany him and Mikhail on a work visit to the China University of Geosciences in Wuhan, and consecutively on a trip to Tibet.

Even though doing a PhD can feel lonely at times, I have never been truly alone. There were other PhD's and PostDocs, struggling, or having struggled, with the same problems every young scientist encounters. We were not so much sailing the same ship to a single destination, but rather a fleet. Each a ship to his or her own and with our own destinations, but sailing on the same ocean, looking after each other. In the beginning I shared an office with Nico, with whom I had some very interesting discussions on overlapping parts of our work. Though I was left alone at the office when Nico continued his career at the TUDelft (with Damien coming in from TNO about once every two months to pick up his mail), there were plenty of colleagues down the hall. There were the experienced PhD's: Javier, Stefan, Maarten, Suzanne, Mohamed and Herman as well as those that had started around the same time as I did, and with whom I spend a lot of my time, at the office, the 'donderdorst' and at conferences, Marten and David. Thank you all for your company.

Others became part of the group as well. There always was Inge of course, who after a long career as Ms (or was it Mrs?) Teclab joined the ranks as a PhD-student. Melody (who had been a guest before) and Elisa came as Marie Curie fellows and others where there for a shorter time, such as both Andrea's and Ioan. With Sierd as a professor, you can be sure there will be a lot of visitors. Many of them worked with Liviu, such as Miloš, Endre and others. Thank you all for being such good colleagues.

Geosciences being a fairly small community, you meet the same people over and over again, at conferences, courses and workshops. Some of them I had known before, others I met on travels during my PhD work. Thank you Wouter, Anneleen and Taco from TUDelft for those memorable evenings at the NAC and other places. Thank you Elco, for a good time, and a transpiring bike ride in San Fransisco. Thank you Ron (VU Amsterdam), Rob (Utrecht) and Hans and Irina (Copenhagen) for organizing some wonderful courses. It was on a course organised by the latter that I met Jens, a PhD-candidate at GFZ-Potsdam, however in a completely different department than I was in. We met often during courses and conferences and generally took way too many pictures, which had to be exchanged on my next trip to Potsdam. Jens, thanks for all the evenings in Potsdam and elsewhere.

Lots of new input I received from Jeroen during the last few months of my PhD-career. We had many discussions over a coffee, tea or sometimes a beer,

on the most varying topics. We could discuss the added value as well as the shortcomings of my work. And even though research is never finished, you helped me see when it was done.

On finishing the thesis, it is send to a review committee. Since they have not been involved in the project, they were able to look at it from an fresh perspective and give some valuable suggestions for improvement of this manuscript. I wish to thank them for their efforts.

Repeated visits to Potsdam where of course part of the project. In the beginning I rented a room in Dietrich's house, but after those initial five months he just let me stay over on my numerous visits to Potsdam. When he moved to a smaller house, Hildegard and Björn opened up their home in the downtown Holländisches Viertel. In between I stayed a few weeks at Krister's place. I want to thank all of you for your kindness and hospitality and the many good conversations we have had.

In the end, it is not only the people from the scientific community that have been there for me these four and a bit years. Here I wish especially to thank my parents, Ad and Gerda, my brother and sister, Wisse and Lianne, you have always been a warm family for me. Renske, thanks for supporting me, especially during times when this thesis got more attention than you did. Liz and Adriaan, I want to thank both of you in advance for agreeing to act as paranymphs, as well as for the intellectual stimulation the both of you have always given me over the years.

And last, but not least, to all of whom I have not mentioned but who were there at some point along the road I travelled, I offer my sincere thanks.

Summary

This thesis presents a novel method for and the results of the construction of a robust high resolution three dimensional model of the structure of the Asian continental lithosphere. This model is obtained using a top-down approach, meaning that a snap-shot view of the lithosphere is created based on available data. Starting from the Earth's surface, each geological layer (sediment, crust, lithospheric mantle) is reconstructed. The main advantage of this approach is that all heterogeneities in an overlying layer are first modelled and subsequently removed from the data before reconstructing a deeper lying layer. Disadvantage is that, despite all precautions, there might still be inaccuracies in top layers which are propagated into deeper layers.

Following the top-down approach, first a model of the sedimentary cover is constructed (chapter 3). Although detailed studies of this layer show a very complicated structure, only large scale features are relevant when constructing a crustal model for an area like Asia. Based on a map of sedimentary thickness Asia is divided into 24 'sedimentary regions', with each region generally defined as having a thick sedimentary cover in the centre and a thin cover at the border. In a region filled with sediments, the density of the sediments generally increases with depth because of mechanical compaction. These densities can be derived from observed P-wave velocities, which show a similar increase with depth. Thus the regions can be divided into continental and oceanic settings, with a subdivision into 'fast', 'intermediate' and 'slow' regions, indicating the relative velocity of P-waves.

This new model of the sedimentary cover is subsequently used to improve the estimate of the depth to Moho by using an innovative application of the remove-compute-restore technique (chapter 4). Starting from the original observations, first the isostatic topographic effect is removed, leading to residual observations. This greatly reduces the variance in depth between the observations. Secondly, the residual observations are interpolated using Ordinary Kriging. By interpolating the residual observations rather than the original observations, the uncertainty of the interpolation is reduced by on average 30%. Finally, the removed isostatic topographic effect is restored to the interpolated Moho depth, leading to the full interpolated depth to Moho. The resulting model shows anomalous deep Moho ($> 50km$) running from the Anatolian Plateau in the west to the Tibetan Plateau ($> 60km$) in the east, coinciding with the Alpine-Himalayan convergence zone. The deepest reconstructed Moho depths are found in the convergence zone just west of the Tarim Basin and at the southern edge of the Tibetan Plateau (both $75km$). North of this zone a major anomalous intraplate feature is found in Central Asia, with deep Moho extending from just west of the Tarim Basin to just west of Lake Baikal ($55 - 60km$), clearly separated from the

Tibetan Plateau by a shallow Moho in the Tarim Basin ($35 - 40km$), and coinciding with a region of major Cenozoic intraplate tectonic deformation occurring in response to the collision between the Indian subcontinent and the Eurasian plate. Large parts of the model of the reconstructed Moho depth have an estimated 1σ -accuracy (of the interpolation) of less than $2km$. Regions with lower accuracy are characterised by lack of data (Arabian Peninsula, Afghanistan and Pakistan, Mongolia and far east Russia), or by abrupt, large lateral variations in Moho depth (western China). Accuracy in these regions can be improved by increasing the amount of observations.

Once a high resolution Moho map has been obtained, the internal structure of the crust can be analysed in terms of wave velocities and densities (chapter 5). For the velocity modelling, the crust is divided into three velocity layers, in which the velocity can vary laterally, but is assumed to be constant in the vertical direction. Three major regions with a characteristic velocity range can be identified: northern and western Asia ($V_p \approx 6.6 - 6.8km/s$), south-east Asia ($V_p \approx 6.3 - 6.4km/s$), and the Tibetan region ($V_p \approx 6.2km/s$). The coefficient of determination (R^2), a measure for the quality of the fit of the velocity-depth relation to the data, is on average 66.5%, but varies substantially throughout the research area. Central China as well as the southern part of Russia are well resolved ($R^2 > 75\%$), whereas the areas around Japan and the Barents Sea remain poorly resolved ($R^2 < 20\%$). Closer analysis of the latter reveals that the crustal velocity distribution in this area can not be easily approximated by the three layer model.

Using the complete crustal model consisting of the model of the sedimentary cover, depth to Moho and lateral variations in density in the crust, the crustal gravity anomaly signal can be removed from observed gravity anomalies derived from satellite missions and field campaigns. The residual anomalies are attributed to density heterogeneities in the uppermost mantle. This approach, therefore, allows for an integrative study of the uppermost mantle, by combining these residual gravity anomalies with seismic tomography data (chapter 6). The results reveal the presence of a cold lithospheric mantle root below the Siberian Craton and the East European Platform, up to a depth of $150km$ and $200km$, respectively. The cold root of the Indian Craton is less thick, being mostly indiscernible at depths below $100km$. The Sino-Korean Craton seems to lack any cold lithospheric mantle root. The mantle beneath the Alpine-Himalayan convergence zone is warmer than ambient, which is most pronounced at depths of $100km$ and $150km$. Differences of up to $200^\circ C$ exist with previous studies of the uppermost mantle temperatures. The uncertainties in the thermal modelling are of the order of $100^\circ C$ and inaccuracies in the composition could add at most $100^\circ C$ to this uncertainty.

The full 3-D model of the lithosphere thus obtained can be used in other studies to assess for example the strength of the lithosphere and model present day deformations (chapter 7). Important spatial variations in the lithospheric strength are predicted throughout the study area. In the crust, this heterogeneity is largely related to variations in crustal thickness, while in the mantle, the mantle temperature is of primary importance. The derived lithospheric strength models should be treated with care since many of the parameters that influence

lithospheric strength are not well determined. Uncertainties of around $100^{\circ}C$ in the mantle temperature model can have a significant effect on the integrated strength of the lithosphere, as do uncertainties in the hydrostatic pore fluid factor, the (static) sliding friction coefficient and variations in actual strain rate. The exact composition of an olivine dominated mantle on the other hand is of minor influence.

Samenvatting

Het doel van dit proefschrift is de constructie van een robuust, drie dimensionaal model met hoge resolutie van de structuur van de Aziatische lithosfeer. Dit model wordt verkregen met behulp van de zo genoemde 'top-down'-aanpak. Bij een 'top-down' aanpak wordt op basis van beschikbare data een momentopname van de lithosfeer gecreëerd. Deze reconstructie begint aan het oppervlak, bij de sedimentaire laag, gevolgd door de (kristallijne) korst, en tenslotte het lithosferische deel van de mantel. Deze aanpak heeft als groot voordeel dat alle diversiteit uit hoger liggende lagen eerst gemodelleerd wordt en haar effecten vervolgens uit de data verwijderd kunnen worden, alvorens dieper liggende lagen gemodelleerd worden. Een nadeel is dat, alle voorzorgsmaatregelen ten spijt, er in hoger liggende lagen nog steeds onzekerheden kunnen sluipen die doorwerken op onderliggende lagen.

Allereerst wordt er een model gemaakt van de sedimentaire bovenlaag (hoofdstuk 3). Hoewel lokale studies tonen dat deze sedimenten een zeer complexe structuur kunnen hebben, zijn bij het construeren van een model voor het continent Azië enkel grootschalige structuren van belang. Op basis van een gecompileerde kaart van sediment diktes wordt Azië onderverdeeld in 24 regio's, waarbij de sedimentlaag in elk gebied het dikst is in het centrum en dun aan de randen. Als een regio gevuld wordt met sedimenten, dan zal de dichtheid van die sedimenten, door mechanische compactie, toenemen met de diepte. De dichtheden kunnen worden afgeleid uit de snelheid van seismische golven (V_p). Op basis van deze snelheden kunnen de 24 regio's worden verdeeld in regio's met continentale en met een oceanische setting, met een onderverdeling in 'snelle', 'gemiddelde' en 'langzame' regio's.

Dit nieuwe model voor de sedimentaire bovenlaag wordt vervolgens gebruikt om schatting van de diepte tot de Moho (de grens tussen de kristallijne korst en de onderliggende mantel) te verbeteren (hoofdstuk 4), gebruikmakend van de remove-compute-restore (verwijder, bereken, herstel) techniek. Hierbij wordt eerst het isostatische effect van de topografie van de originele waarnemingen verwijderd, waardoor de residuele waarnemingen overblijven. Dit leidt tot een sterke verkleining van de variantie tussen de waarnemingen. Met behulp van 'Ordinary Kriging' worden vervolgens deze residuele waarnemingen geïnterpoleerd in plaats van de originele waarnemingen, wat resulteert in een reductie van de interpolatie onzekerheid met gemiddeld 30%. Tenslotte wordt het eerder verwijderde isostatische effect van de topografie hersteld. Het resulterende model toont een diepe Moho ($> 50km$) tussen de Anatolische hoogvlakte in het westen en Tibetaanse hoogvlakte ($> 60km$) in het oosten. Dit is de Alpiene-Himalaya convergentie zone. De diepste Moho ($75km$) vindt men in deze convergente zone, net ten westen van het Tarim bekken en langs de zuidelijke rand van de

Tibetaans hoogvlakte. Ten noorden hiervan vindt men een intraplaat structuur met verdiepte Moho (55 – 60km) die zich uitstrekt van net ten westen van het Tarim bekken tot net ten westen van het Baikalmeer. Deze wordt door het Tarim bekken (35 – 40km) duidelijk gescheiden van de Tibetaanse hoogvlakte. Deze structuur kan worden gekoppeld aan de grootschalige deformatie tijdens het Cenozoïcum ten gevolge van de botsing van de Indische plaat met de Aziatische plaat. In grote delen van het Moho diepte model is de geschatte 1σ -onzekerheid (van de interpolatie) kleiner dan 2km. Gebieden met een hogere onzekerheid worden gekenmerkt door een gebrek aan beschikbare waarnemingen (het Arabisch schiereiland, Afghanistan en Pakistan, Mongolië en het meeste oostelijke deel van Rusland) of door sterke en abrupte verschillen in Moho diepte (West-China). De interpolatie onzekerheid in deze gebieden kan verkleind worden door het aantal beschikbare waarnemingen uit te breiden.

Als eenmaal de diepte tot de Moho is bepaald, kan de interne structuur van de korst worden geanalyseerd in termen van seismische golfsnelheden en dichtheden (hoofdstuk 5). In dit snelheidsmodel wordt de korst in drie lagen verdeeld, waarbij de golfsnelheid horizontaal kan variëren, maar in verticale richting constant is binnen de betreffende laag. Het snelheidsmodel voor de Aziatische korst toont een onderverdeling in drie gebieden: noord-westelijk Azië (gemiddelde golfsnelheid $V_p \approx 6.6 - 6.8 \text{ km/s}$), zuid-oostelijk Azië ($V_p \approx 6.3 - 6.4 \text{ km/s}$), en de regio rond de Tibetaanse hoogvlakte ($V_p \approx 6.2 \text{ km/s}$). De determinatiecoëfficiënt (R^2), welke aangeeft hoe goed de gemodelleerde golfsnelheids-diepte functie de data verklaart, is gemiddeld 66.5%. De variatie in R^2 is echter groot. Centraal China en het zuidelijk deel van Rusland tonen een hoge R^2 (> 75%), terwijl de gebieden rond Japan en de Barentssee een lage R^2 tonen (< 20%). Een verdere analyse van laatstgenoemde regio laat zien dat de golfsnelheden in de korst zich niet goed laten benaderen door het drie-lagen model. De golfsnelheden worden tenslotte geconverteerd naar dichtheden in de korst.

Het complete korstmodel, bestaande uit het model van de sedimentlaag, Moho diepte en laterale variaties in de dichtheden in de korst, kan gebruikt worden om het gravitatie-signaal van de korst van de waargenomen zwaartekrachtsanomalieën af te trekken. De residuele zwaartekrachtsanomalieën kunnen worden toegeschreven aan dichtheidsvariaties in de bovenste mantel. Hierdoor is een integrale studie van de bovenste mantel mogelijk, waarbij de residuele zwaartekrachtsanomalieën met seismische tomografie gecombineerd worden om dichtheden en temperaturen in de bovenste mantel af te leiden (hoofdstuk 6). Deze studie toont een koude kiel met een diepte tot 150km en 200km in de lithosferische mantel onder respectievelijk het Siberische Craton en het Oosteuropese Platform. De koude kiel onder het Indische Craton reikt minder diep, en is op diepten groter dan 100km nauwelijks waarneembaar. Het Sino-Koreaans Craton lijkt in het geheel verstoken van een koude kiel. De mantel onder de Alpen-Himalaya convergente zone is warmer dan gemiddeld, wat het meest tot uiting komt op diepten van 100km and 150km. Verschillen met voorgaande studies van de bovenste mantel kunnen oplopen tot 200°C. De onzekerheid in de temperatuur modellering, op basis van mineralogische eigenschappen is 100°C en onnauwkeurigheden in de compositie kunnen hier nog ten hoogste 100°C aan toe voegen.

Het op deze manier verkregen drie-dimensionale model van de lithosfeer kan worden gebruikt om de sterkte van de lithosfeer te bepalen en hedendaagse deformaties te modelleren. Een eerste aanzet tot het bepalen van de sterkte van de lithosfeer (hoofdstuk 7) toont grote variaties door het gehele studiegebied. Deze heterogeniteit is, wat de korst betreft, voornamelijk gerelateerd aan variaties in de dikte van de korst, en wat de mantel betreft aan de temperatuurvariaties in die mantel. De verkregen sterktemodellen van de Aziatische lithosfeer moeten echter, net als elk sterktemodel van de lithosfeer, met de nodige voorzichtigheid behandeld worden, aangezien veel van de parameters die van invloed zijn op die sterkte niet voldoende nauwkeurig bepaald kunnen worden. Onzekerheden in de orde van 100°C in het mantel temperatuur model kunnen, evenals onzekerheden in de hydrostatische poriën vloeistof factor, de statische schuifcoëfficiënt en variaties in de daadwerkelijke deformatiesnelheid, een significant effect hebben op de geïntegreerde sterkte. De exacte compositie van een door olivijn gedomineerde mantel is daarentegen van minder belang.

It is that neither you nor anyone else knows for certain what happens in the Earth's interior, given that scarcely a twelve-thousandth part of its radius is known - Jules Verne's 'A Journey to the Centre of the Earth'



Introduction

Density heterogeneities within the crust and upper mantle are main factors in the control of the dynamics of Earth deformation at shallow and deep levels. Tectonic processes thus strongly depend on the thermo-mechanical structure of the lithosphere. The main aim of this PhD-project is to construct a robust high-resolution 3D thermal-density model for the lithosphere of the Asian continent, which is a key natural laboratory for the study of active intra-continental deformation in response to the ongoing collision of India and Eurasia. To better understand the dynamic regime of the lithosphere and tectonics in this area as a whole, an integrated multidisciplinary approach is pursued in this project, closely linking the development of new concepts, methodology and analytical techniques. Recent and ongoing satellite gravity missions like Challenging Minisatellite Payload (CHAMP), Gravity Recovery And Climate Experiment (GRACE) and Gravity Field and Steady-State Ocean Circulation Explorer (GOCE), providing globally complete and homogeneous gravity models with unprecedented accuracy, allow for this integration and joint inversion of the satellite-derived data with terrestrial (primarily seismic) data to construct these novel 3D density and thermal models of the crust and lithosphere.

These models can be used for instance to assess and quantify the 3D spatial strength distribution within the continental lithosphere, which will provide new insights in the localization of intraplate continental deformation. Furthermore these models can be used as boundary conditions on future investigations into the asthenospheric mantle and below.

The remainder of this introductory chapter is dedicated to presenting the outline of this thesis report (section 1.1) and a short introduction to the study area (section 1.2).

1.1 Thesis outline: A top-down approach

In solid earth system modelling, two approaches can be used; bottom-up (with a focus on processes) and top-down (focus on data). In a bottom-up approach physical processes, assumed to be taking place in the Earth's interior, are modelled and actual observations are used as boundary conditions to these processes. Advantages of the bottom-up approach is that, since physical processes are modelled, resulting models are internally consistent. Disadvantages are, amongst

others, the assumption that these physical processes (often assumed to be in steady state) are accurately modelled and the assumption that any factors disturbing the observations, which are used as boundary conditions, are accurately known.

In this project, the alternative top-down approach is applied. A top-down approach does not model any processes, but is a snap-shot view, based on available data. Layer by layer, starting from the top, the sedimentary layer, and working slowly down through the crust and lithospheric mantle, are reconstructed. The main advantage of this approach is that all heterogeneities in an overlying layer are first modelled and can subsequently be removed from the data before attempting to reconstruct a deeper lying layer. Disadvantage is that, despite all precautions, there might still be inaccuracies in top layers which are propagated to deeper layers. Furthermore, physical consistency of the model is not guaranteed, but can be required as additional constraint.

This top-down approach can be recognized in the set-up of this thesis. In each chapter, a new model is presented that is used as a boundary condition on the model presented in the following chapter. The only exception is chapter 2, where the different datasets that are used in this study are introduced. In chapter 3¹ the sedimentary cover of the study area is divided into several regions and each region is analysed, leading to a comprehensive model of the sedimentary cover, consisting of a velocity and density profile for each region. This new model of the sedimentary cover is used in chapter 4 to improve the estimate of the depth to Moho using an innovative application of the remove-compute-restore technique [Stolk et al., 2013]. Once a high resolution Moho map has been obtained, the internal structure of the crust can be analysed in terms of wave velocities and densities (chapter 5). Using the complete crustal model consisting of the model of the sedimentary cover, depth to Moho and lateral variations in density in the crust, the crustal gravity anomaly signal can be removed from gravity anomalies derived from satellite observations and field campaigns. The residual anomalies are attributed to density heterogeneities in the upper mantle. This allows for an integrative study of the upper mantle, by combining these residual gravity anomalies with seismic tomography data. The methodology as well as the 3-D composition, thermal and density models thus obtained are presented in chapter 6. The full 3-D model of the lithosphere thus obtained can be used in opportunities and a short future outlook.

1.2 Geology of the Asian continent

Asia comprises roughly the eastern half of the Eurasian plate and has a long history of reworking due to tectonic deformation, leading to large heterogeneities (figure 1.1, e.g. Artemieva [2009, 2011]). Archean and early Proterozoic crust is found in (parts of) the Siberian Craton (e.g. USGS [1997], Griffin et al. [1999]). During the Paleozoic and Devonian times, slivers of continental crust accreted to the Siberian Craton [Sengör et al., 1993]. During the Middle Carboniferous, the

¹Chapters 3, 4 and 5 are based on Stolk et al. [2013], Tectonophysics, <http://dx.doi.org/10.1016/j.tecto.2013.01.022>

Uralian Ocean (opened in Late Cambrian, Early Ordovician) between the Baltica (containing amongst other the East European Platform) and the Kazakhstanian continent (containing the Siberian Craton) closed [Puchkov, 2002], creating the Uralides. Extension occurred in the Paleozoic, creating what now is the West-Siberian Basin [Sengör et al., 1993] (see figure 1.1).

Further south, the most profound contemporary continent-continent collision is ongoing [Rowley, 1996]. Starting around $50Ma$ the Indian subcontinent collided with Eurasia. India still moves towards Asia with a relative velocity of $50mm/yr$ [White and Lister, 2012]. However, only around $20mm/yr$ is accommodated as shortening across the Himalayas (e.g. Larson et al. [1999]). The remaining shortening is partially accommodated in a south-eastward extrusion of crustal material (e.g. Molnar and Tapponnier [1975]) and partially by the Tibetan Plateau. In the west, the shortening is accommodated in the Pamir-Hindukush mountains, and partially propagated northward, where it re-activates older intra-plate structures in the Tien Shan and Altai Mountain regions. In between lie relatively tranquil basins, the largest of which are the Tarim Basin and the Junggar Basin. North of the India-Asia collision zone, on the south-eastern border of the Siberian Craton the Baikal rift started opening up roughly $30Ma$ [Petit and Déverchère, 2006, Delvaux et al., 1997]. The structure is about $2500km$ long from its south-western extremities to the north-east and consists of several basins of different ages and geometries [Petit and Déverchère, 2006, Logatchev and Florensov, 1978].

Modelling of the Asian crust has a long history as well. One of the first 3-D models of the crust for Central and Northern Eurasia was constructed by Artemjev et al. [1994]. This model describes variations of the depth to basement (sediment thickness) and Moho discontinuity, but also density variations within the sedimentary cover. This model was improved by incorporating new data and providing seismic velocities for the crystalline crust [Kaban, 2001]. Later, the model has been extended to the south to include the entire Asian continent [Kaban et al., 2009]. Several density model studies of the lithosphere and upper mantle have been performed for other parts of Eurasia, such as the East European Platform [Yegorova and Starostenko, 1999] and the southern regions of the former USSR [Kaban et al., 1998]. The results of the various regional studies cannot be directly compared as they usually employ different technologies and data, resolution, reference models, relations between density and velocity etc. Up till now no consistent regional model of the lithosphere in the Asian continent exists, like there exists for the European lithosphere, e.g. Tesauro [2009].

1.3 Funding and support

This research was performed through a grant by the Netherlands Space Organisation (NSO), under the auspices of Netherlands Research Centre for Integrated Solid Earth Sciences (ISES) and in close cooperation with the Helmholtz-Zentrum Potsdam Deutsches GeoForschungsZentrum (GFZ). Partial support from the United States Geological Survey (USGS) National Earthquake Haz-

ards Program is appreciated.

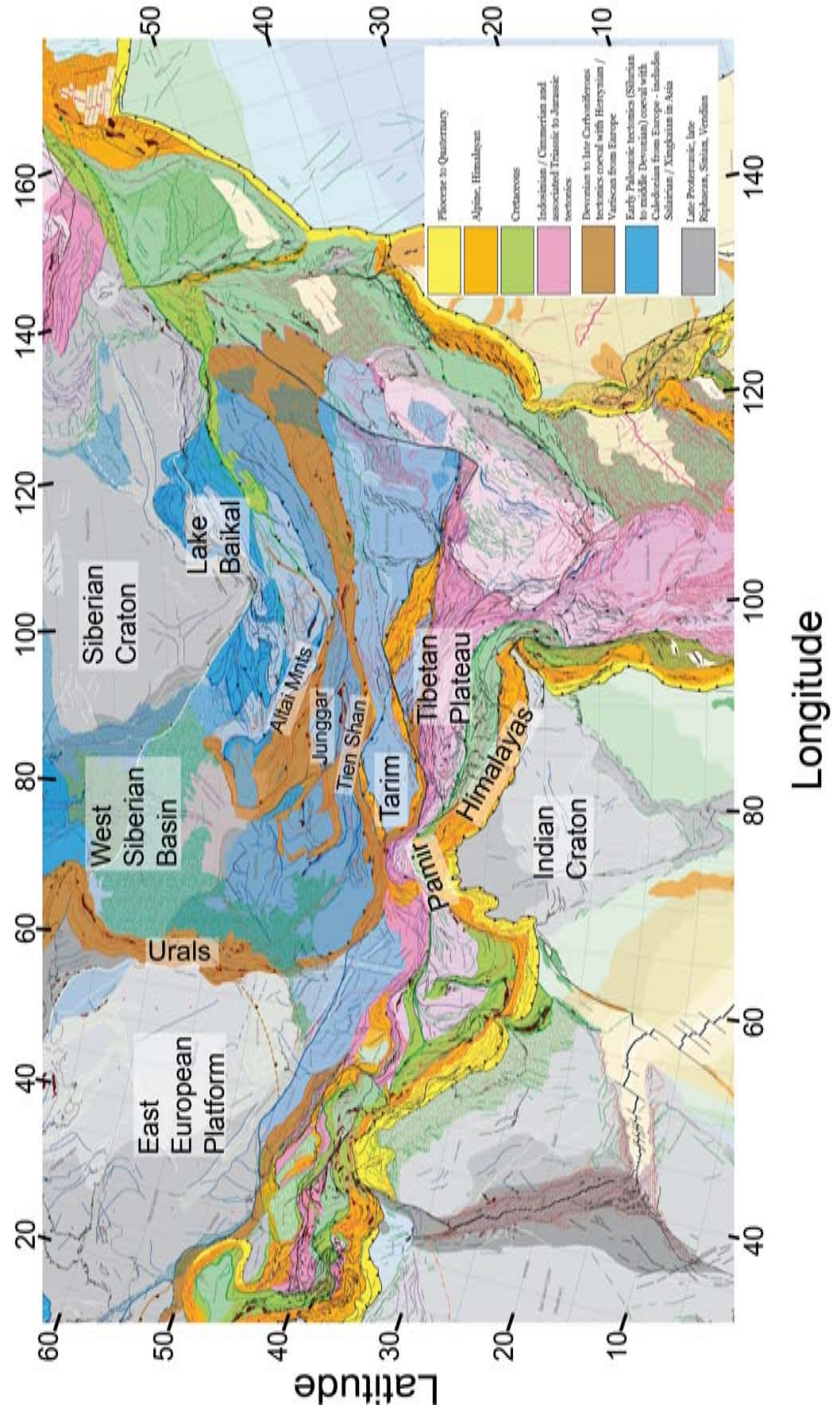


Figure 1.1: Geological map of Asia, modified from Pubellier et al. [2008]

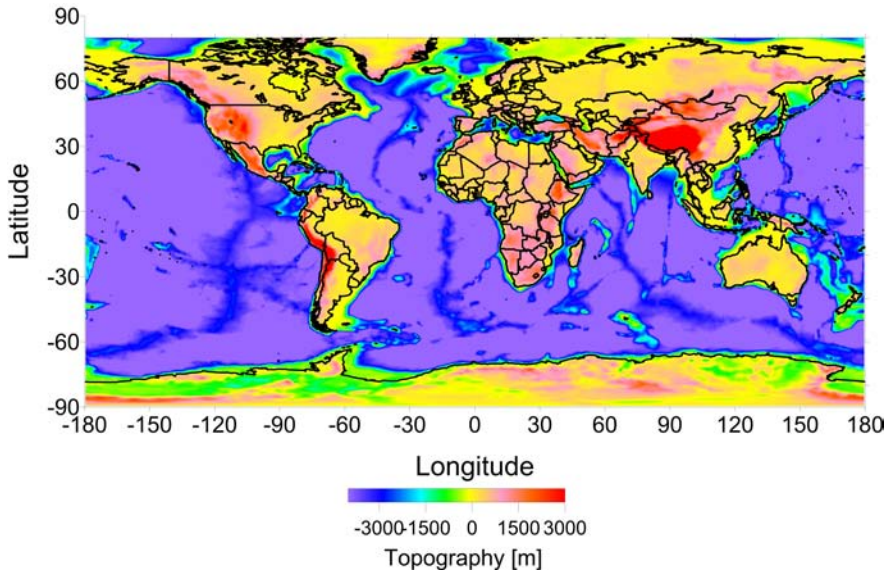


Datasets used in this study

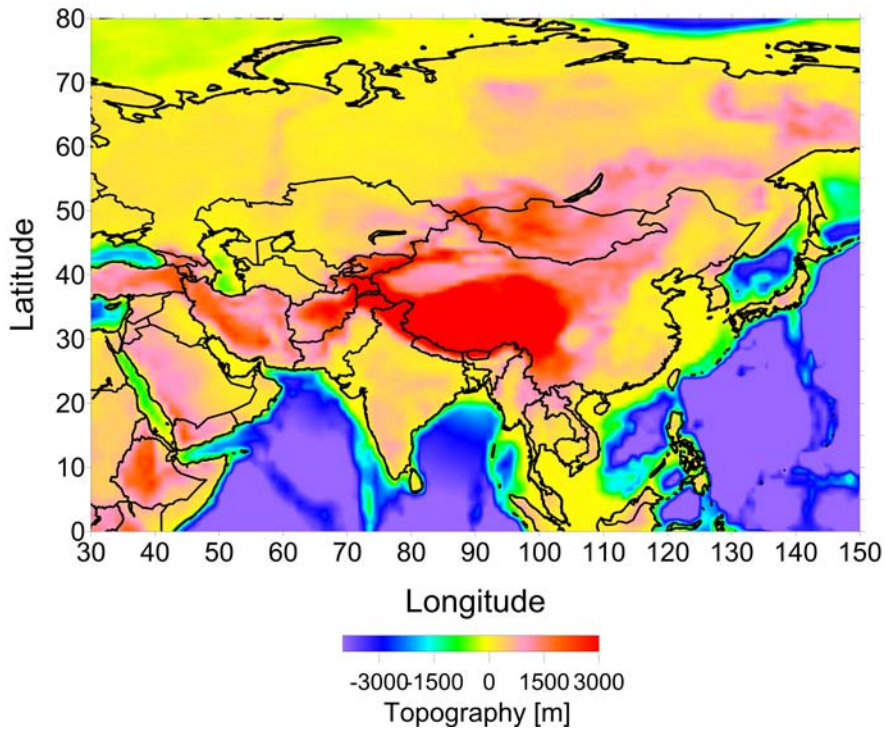
This study makes use of several freely available datasets containing information on topography, sedimentary thickness, crustal and lithospheric properties. In this chapter, these datasets are presented in more detail. Furthermore, slight modifications made to the datasets and mergers of some datasets are also described. When, in the remainder of this thesis reference is made to a dataset, always the data as presented in this chapter is implied. The data that will be treated in this chapter is: **(1)** topography, obtained from the ETOPO1 global relief model of the National Geophysical Data Center (NGDC) [Amante and Eakins, 2009] (section 2.1), **(2)** sediment thickness maps, adapted from Exxon [1985] (section 2.2), **(3)** a database with published seismic and seismological studies (e.g. [Mooney, 2007]) (section 2.3), **(4)** seismic tomography models of the upper mantle [Koulakov, 2011, Ritsema et al., 2011] (section 2.4) and **(5)** gravity anomalies from the Eigen6C Earth gravity field model [Förste et al., 2011] (section 2.5).

2.1 Topography

Topography is obtained from NGDC's ETOPO1 global relief model (figure 2.1 [Amante and Eakins, 2009] and can be downloaded from: <http://www.ngdc.noaa.gov/mgg/global/global.html>. Within our study area ($0 - 80^{\circ}N$, $30 - 150^{\circ}E$), the ETOPO1 model makes use of elevation and bathymetry models of the Space Shuttle Radar Topography Mission (SRTM), Global Land One-kilometer Based Elevation (GLOBE), GTOPO30, Leibniz Institute for Baltic Sea Research Warnemünde (IOW), Caspian Environment Programme, International Bathymetric Chart of the Arctic Ocean (IBCAO), Japan Oceanographic Data Center (JODC) and Mediterranean Science Commission (CIESM). The topography has been downloaded on a 10minute spacing (figure 2.1a) and has been downsampled to 1° by averaging over 6x6-grid cells, which is the general resolution used in this research. The resulting topographic model is displayed in figure 2.1b.



(a) ETOPO topography world wide



(b) Topography in the study area, averaged over $1^\circ \times 1^\circ$ cells

Figure 2.1: Topography (and bathymetry) from ETOPO-1 [Amante and Eakins, 2009]

2.2 Sediment thickness model

In this research the thickness of the sedimentary cover is taken from the "Tectonic map of the World" [Exxon, 1985] (digitized on a $1^\circ \times 1^\circ$ resolution by Laske and Masters [1997]), complemented with more detailed regional maps. For Central and Northern Eurasia north of $30^\circ N$ the map of Kaban [2001] is used. Most parts of this map (except remote North-eastern Russia) have a resolution of $15' \times 15'$ and are based on detailed regional maps. For the adjacent oceans a recent compilation of the National Oceanic and Atmospheric Administration (NOAA)-NGDC is used [Divins, 2003]. The final compiled map of sedimentary thickness in Asia is shown in 2.2 and has an overall resolution of $1^\circ \times 1^\circ$ (Kaban, pers. comm. 2011).

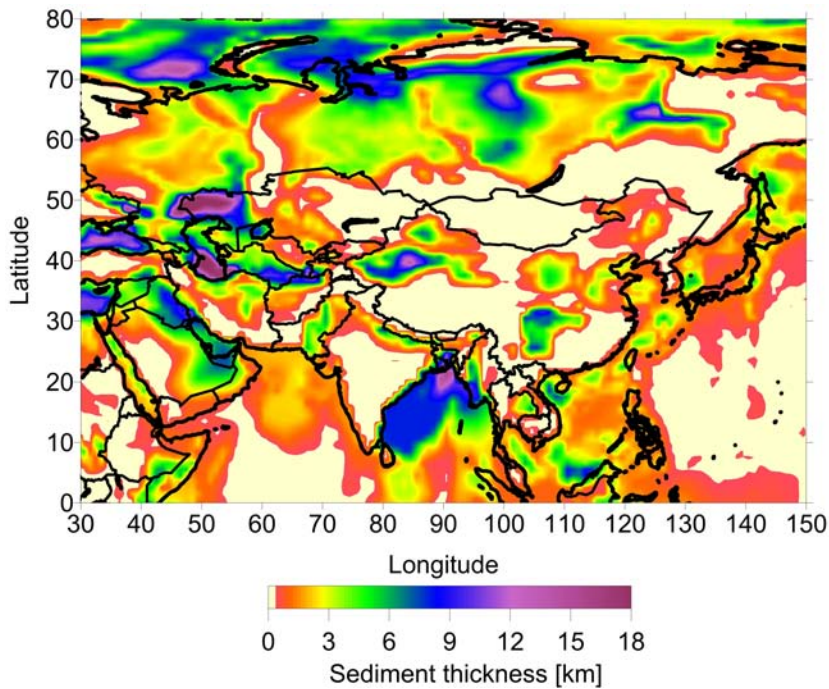


Figure 2.2: Contour map of thickness of the sedimentary cover in the study area. North of $30^\circ N$ Kaban [2001], south of $30^\circ N$ Exxon [1985], adjacent ocean regions Divins [2003].

2.3 Seismic data

Currently the most complete global digital data set of seismic studies is compiled in the USGS database [Mooney, 2007]. This database is regularly updated with new data and in this research the 2011 update (Mooney, pers. comm. 2011) was used. All entries in the database are digitisations from published,

and some unpublished, seismic data (mainly refraction, reflection seismic sections and receiver function results). Observations that make use of gravity data, magnetic anomalies or other have been excluded. For Asia major contributions to the database come from the publications of Egorkin [1991, 1998] and unpublished reports by the GEON [1989, 1992] for Eastern Russia and Vol’vovskii and Vol’vovskii [1975] for the former Union of Soviet Socialist Republics (USSR) territory in general. Verba et al. [1992] is the most important contributor to entries concerning the Laptev Sea, whereas data in the Barents Sea mainly comes from Jackson [2002a]. Data concerning China come from many sources, amongst which Youngsheng et al. [1996] and Wang and Mooney (pers. comm.) are prominent. This list of references is by no means exhaustive, many more publications are considered in the USGS database. In addition to the USGS database, the latest publishings of data on the crust coming purely from seismics and seismology were digitised and used in this research. Locations of all digitised data locations (both M_{obs} and (V,z) -pairs) considered in this research are shown in figure 2.3.

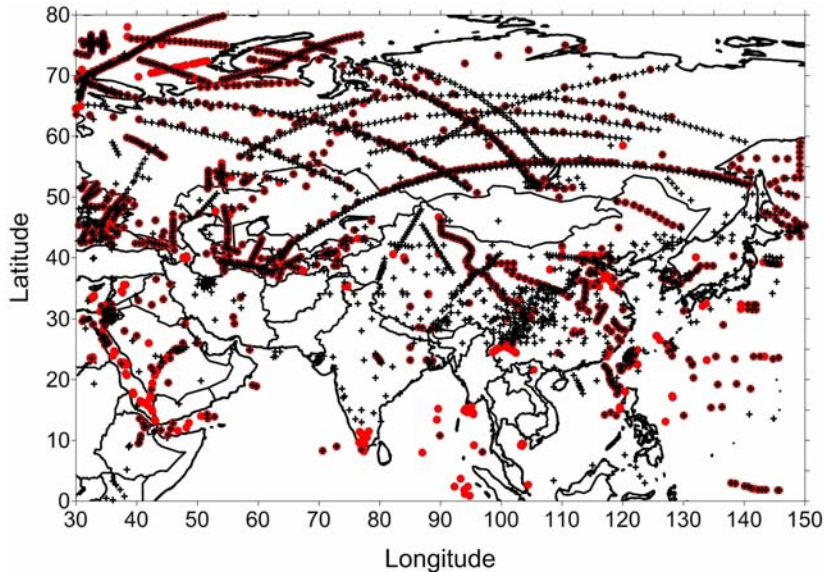


Figure 2.3: Map of the study area with locations of observations (black cross = M_{obs} , red dot = one or multiple (V,z) -pairs)

A typical USGS database entry (table 2.1) contains geophysical and geological information on a vertical crustal column at a certain location on the Earth. The column of crystalline crust is subdivided in several layers and is possibly overlain by one or more layers of sediments. For each crustal layer, the depth from the surface to the top of the layer, as well as thickness of the layer are given. Furthermore, the database contains for each layer P-wave and, if available, S-wave velocities and some other characteristics of that layer. Also the depth from the surface to the Moho boundary at that location is given.

Table 2.1: Example from USGS database, an entry has an identification number (ID), location (Loc) in latitude and longitude, followed by several layers discerned at that location. For each layer the P- and S-wave velocities (V_p and V_s) are given as well as the layer thickness (t_{layer}) and the depth to the top of the layer (z_{top}). A letter indicates the type of the layer (s = sediment, c = crust and m = depth to Moho)

ID	Loc	V_p	V_s	t_{layer}	z_{top}	ind
95	43.94N 59.85W	1.75	.00	1.00	.00	s
		3.10	.00	1.30	1.00	s
	3.80	.00	2.30	2.30	s	
	5.40	.00	9.20	4.60	c	
	6.23	.00	21.20	13.80	c	
	8.00	.00	.00	35.00	m	

Entries from the USGS database within the study area are pre-processed before being used. Reference to data and/or observations in chapters 3, 4 and 5 refers to the data after pre-processing. In pre-processing the data, the average P-wave velocity of each layer is calculated and assigned to the middle of the layer, see equation 2.1. For a layer with constant velocity, this is simply the relocation of that velocity to the middle of the layer. In case of a linear increase, or decrease, of V_p in a layer, the average velocity is calculated and placed at the middle of the layer. The depth to Moho (M_{obs}) at each observation location is also extracted from the database. Figure 2.3 shows all locations of both the Moho observations and (V, z)-pairs. Note z denotes the depths from mean sea level throughout this thesis, i.e. a depth to Moho of $43km$ signifies that the Moho is located $43km$ below mean sea level. A mountain rising $5km$ above sea level will have depth $z = -5km$.

$$\begin{aligned}
 [V, z] &= [V_p, z_{top} + 0.5t_{layer}] && \text{if } V_p \text{ constant in layer} \\
 [V, z] &= [0.5(V_p^{top} + V_p^{bottom}), z_{top} + 0.5t_{layer}] && \text{if } V_p \text{ gradient in layer}
 \end{aligned}
 \tag{2.1}$$

To assess the quality of the database, parts of the dataset have been checked against direct digitisations of the original data [Kaban, pers. comm.], e.g. the data from the peaceful nuclear seismic profiles, performed in the 1970's and 1980's in Russia (e.g. Egorkin [1991, 1998]). No significant differences were found.

2.4 Seismic tomography data of the mantle

Two separate seismic tomography models are used in this research. A high resolution ($30' \times 30'$) V_p -anomaly model covering Asia and adjacent regions (figure 2.4) [Koulakov, 2011] and the global S40 V_s -anomaly model [Ritsema et al., 2011] (figure 2.5), which is truncated at spherical harmonic degree 40, corresponding

to a lower resolution of $4^{\circ}30' \times 4^{\circ}30'$. For gravity field modelling (section 6.2), a global model is preferable. Since high resolution is only required in the area of interest, the S40 model is therefore used as background model against the Koulakov model.

The combination of both models is not trivial. First the Koulakov model needs to be converted to V_s -anomalies. Secondly, the Koulakov tomographic model uses an 10° diameter moving window centred around the evaluation location to compute wave velocities in the upper mantle. As a consequence of this moving window technique, long wave length ($\lambda_{wave} > 2000km$, spherical harmonic degree < 20) signals are filtered out of the model.¹ This can be clearly observed in the power spectrum of the Koulakov model (black line in figure 2.6). Since the S40 model (blue line in figure 2.6) is truncated at degree 40, a combination of both models requires the application of a low pass filter to the S40 model, and a high pass filter to the Koulakov model, figure 2.7.

It can also be observed in figure 2.6 that the power of the Koulakov model in the mid-range wavelengths (spherical harmonic degree 20-40) is 1.5 times lower than that of the S40 model, suggesting an underestimation of the absolute values of velocity anomalies. This analysis is consistent with the technique with which the Koulakov model was derived. Therefore, in addition to the high pass filter, the power of the Koulakov model is increased by a factor 1.5 in order to match the overall power in the S40 model. The resulting model is given in figure 2.8 and its power spectrum is represented by the red line in figure 2.6. When in the remainder of this thesis, reference is made to the tomographic model, tomographic data, tomographic observations etc. the combined model is being referred to.

¹The moving window technique in this case means that the wave velocity anomaly at a grid point is determined based on measurements lying within a 5° radius around the grid point. The resulting wave velocity anomaly is then the anomaly with respect to the average wave velocity in the 10° circle belonging to that grid point. This is an effective method to obtain a smoother model. However, since the anomalies at all grid points are related to the average velocity in that grid point's 10° circle, this moving window technique also essentially filters out any signal with a half wavelength larger than 10° .

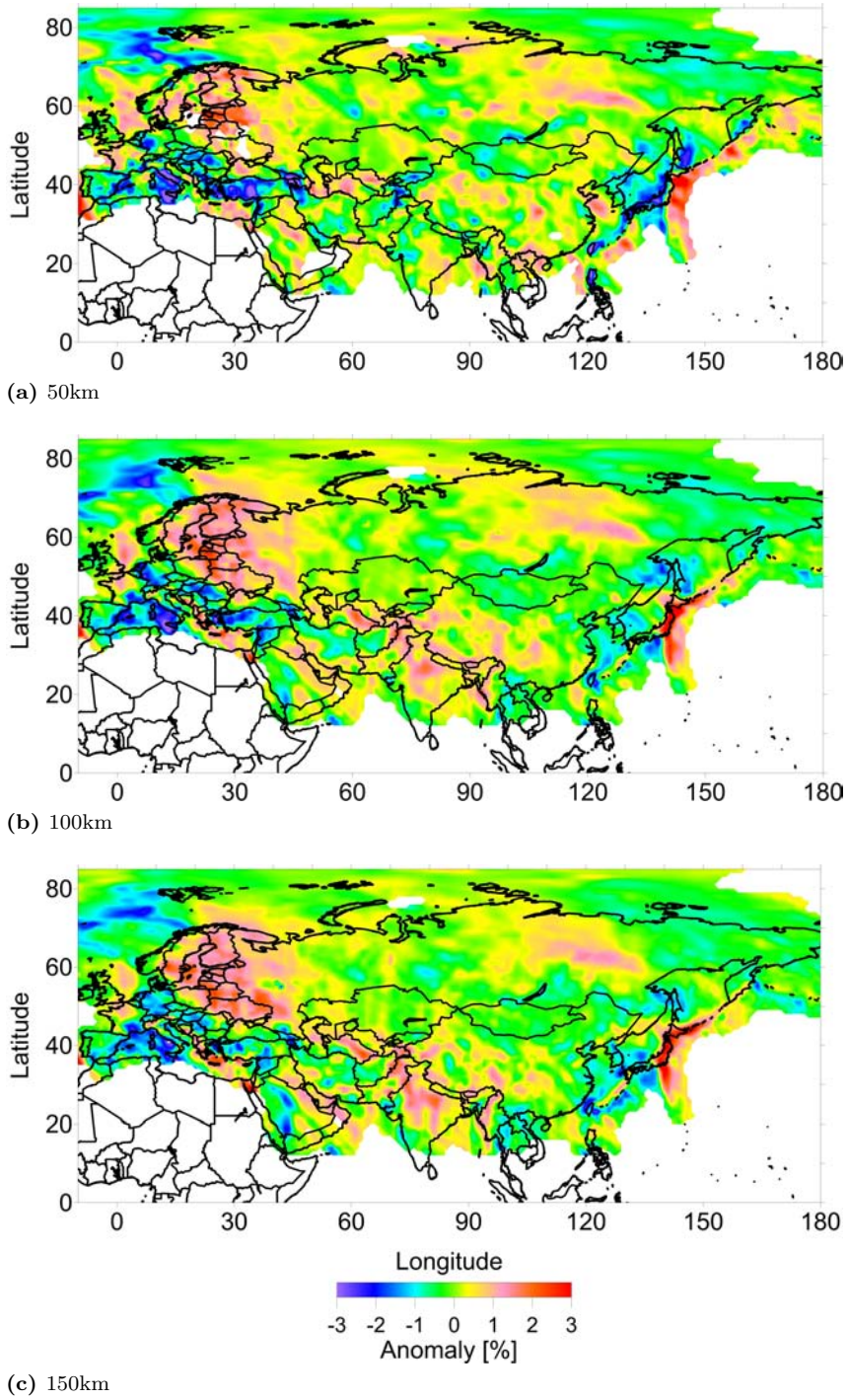


Figure 2.4: P-wave velocity anomalies at different depths for Asia and surroundings inferred from seismic tomography [Koulakov, 2011]

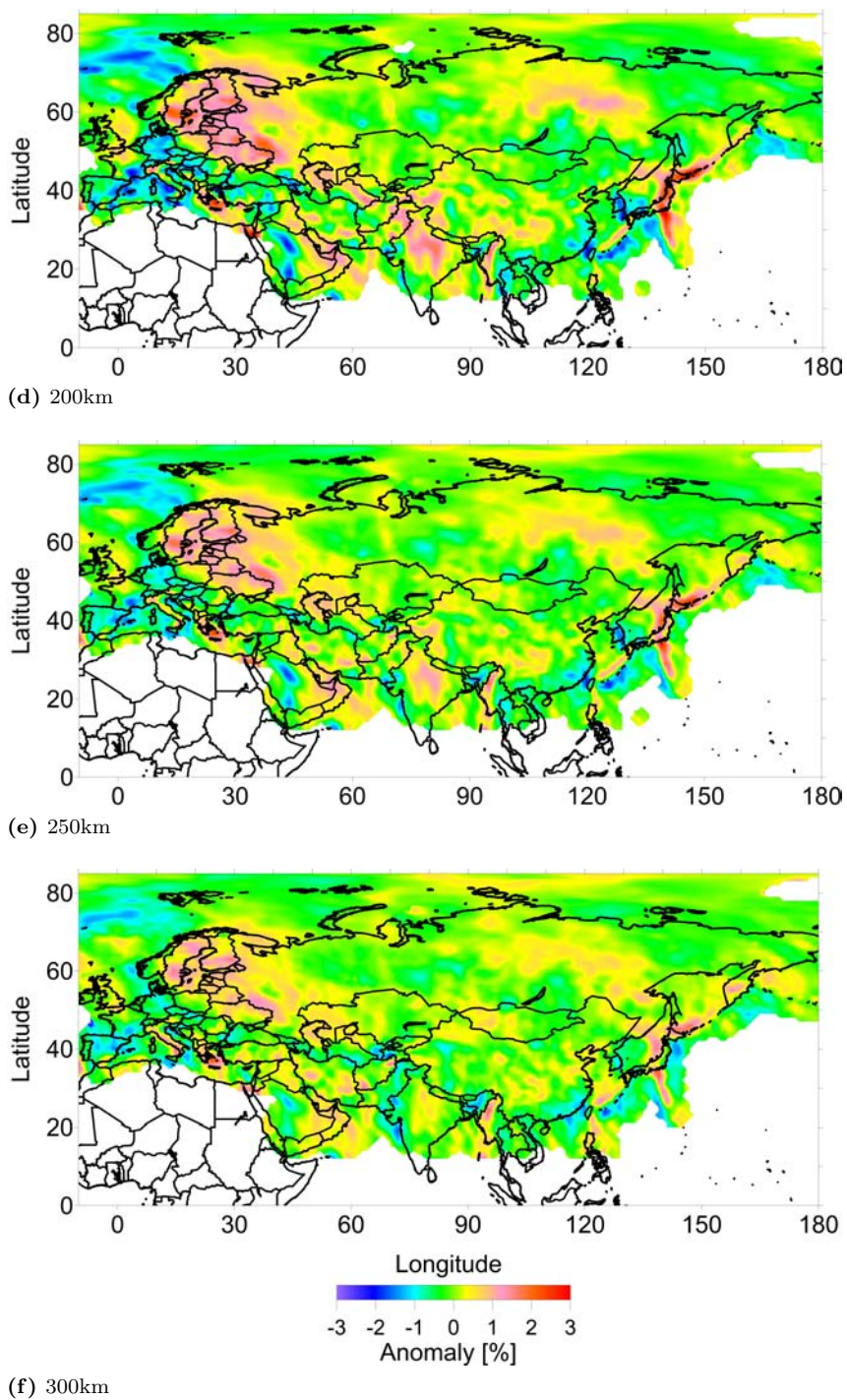


Figure 2.4: P-wave velocity anomalies at different depths for Asia and surroundings inferred from seismic tomography [Koulakov, 2011] (continued)

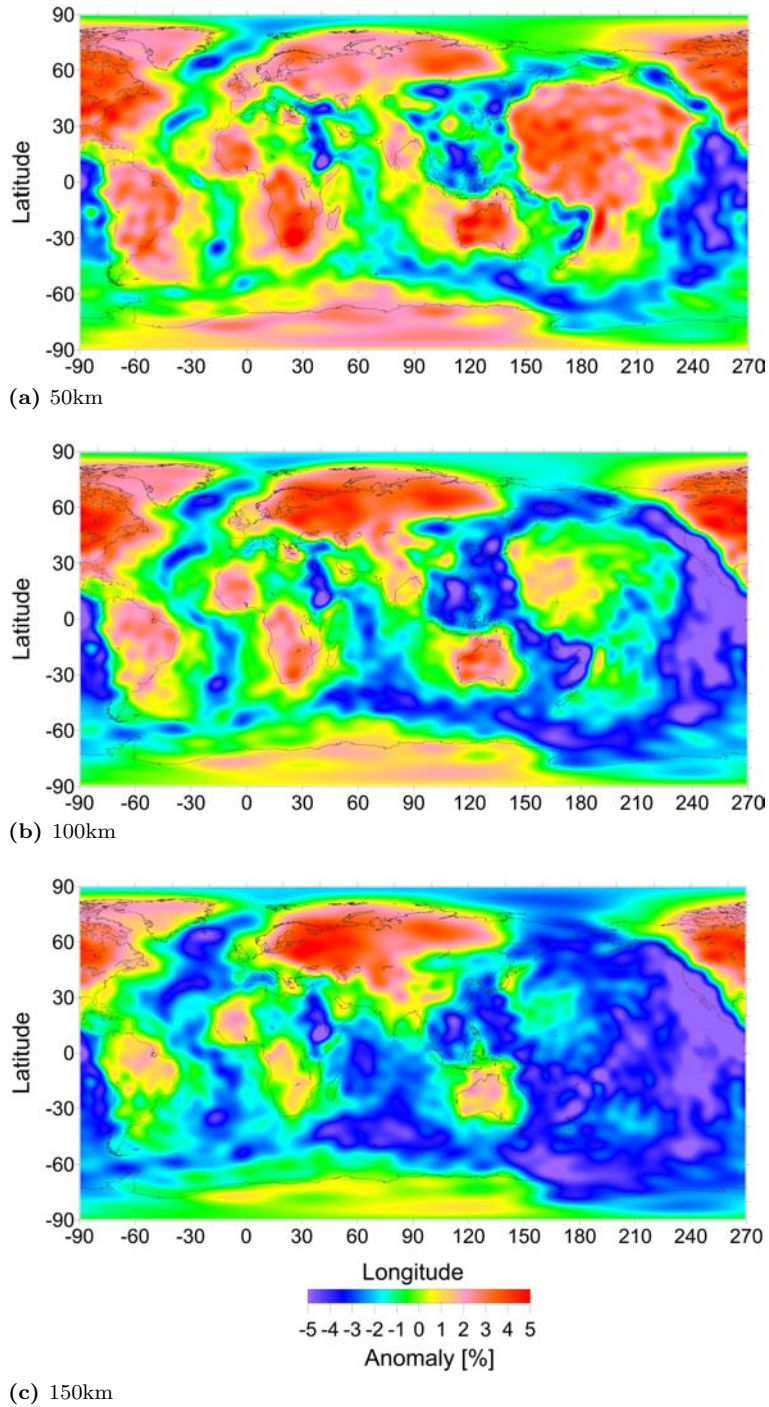


Figure 2.5: S-wave velocity anomalies at different depths from the global S40 model [Ritsema et al., 2011]

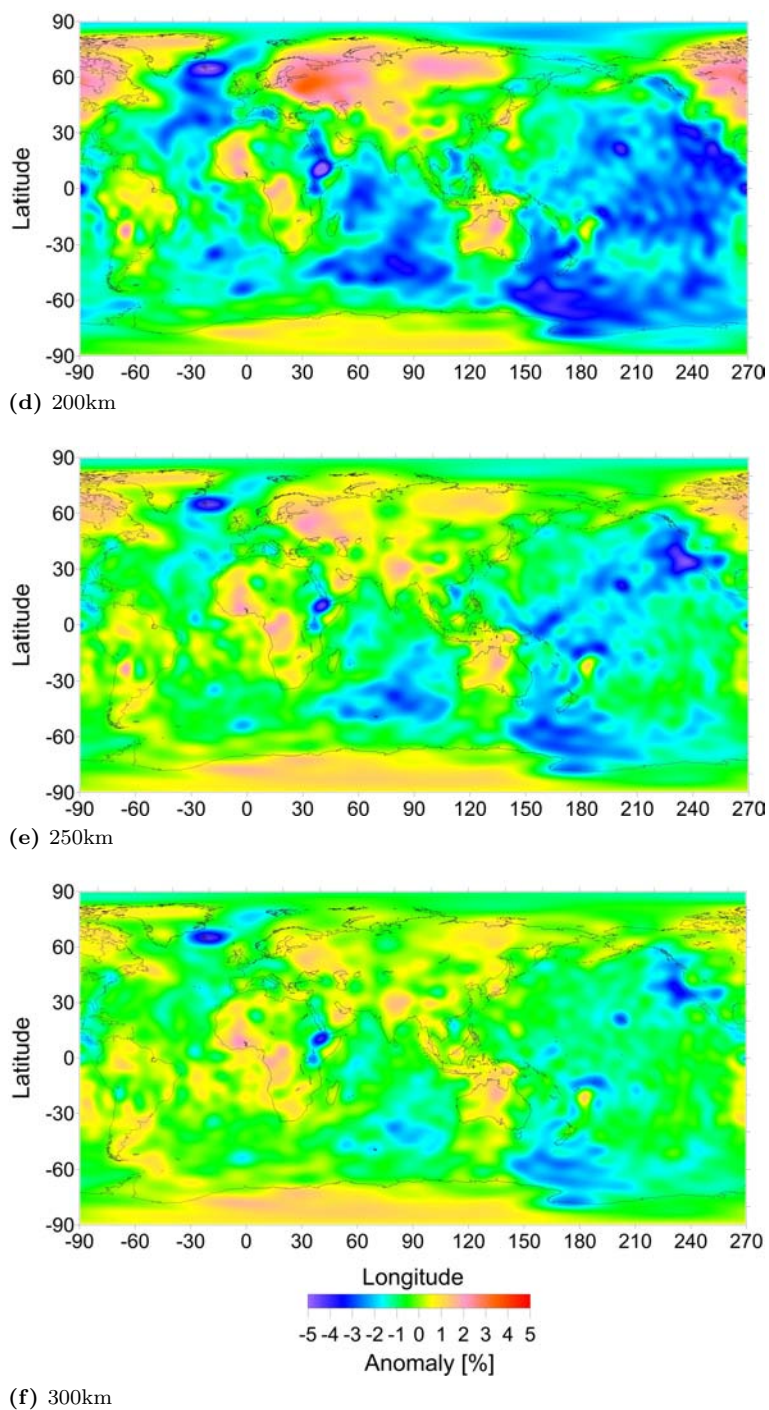


Figure 2.5: S-wave velocity anomalies at different depths from the global S40 model [Ritsema et al., 2011] (continued)

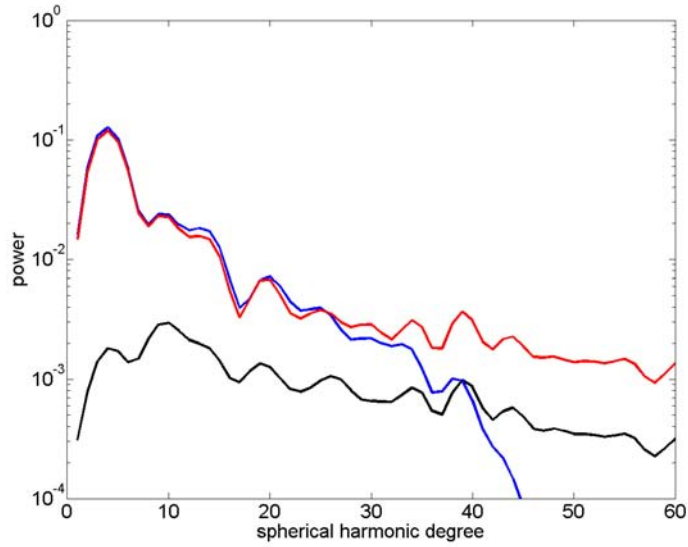


Figure 2.6: Power spectrum of the Koulakov [2011] model (black), S40 (blue) and combined model (green)

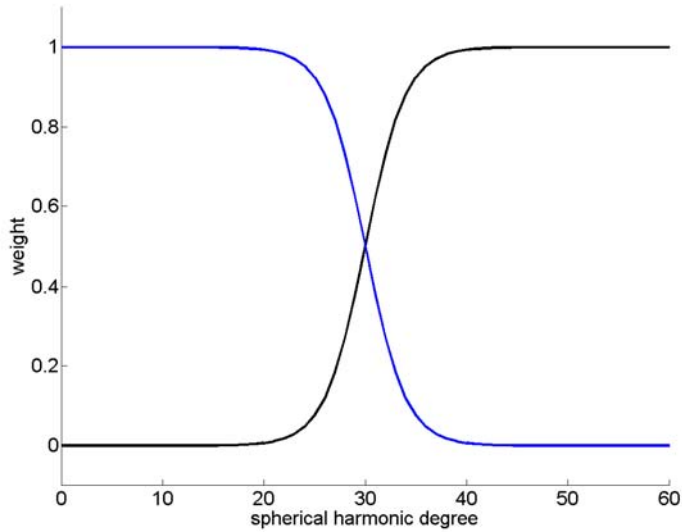


Figure 2.7: Weights assigned to the different spherical harmonic degrees, using a low pass filter for the S40 model (blue) and a high pass filter for the Koulakov [2011] model (black)

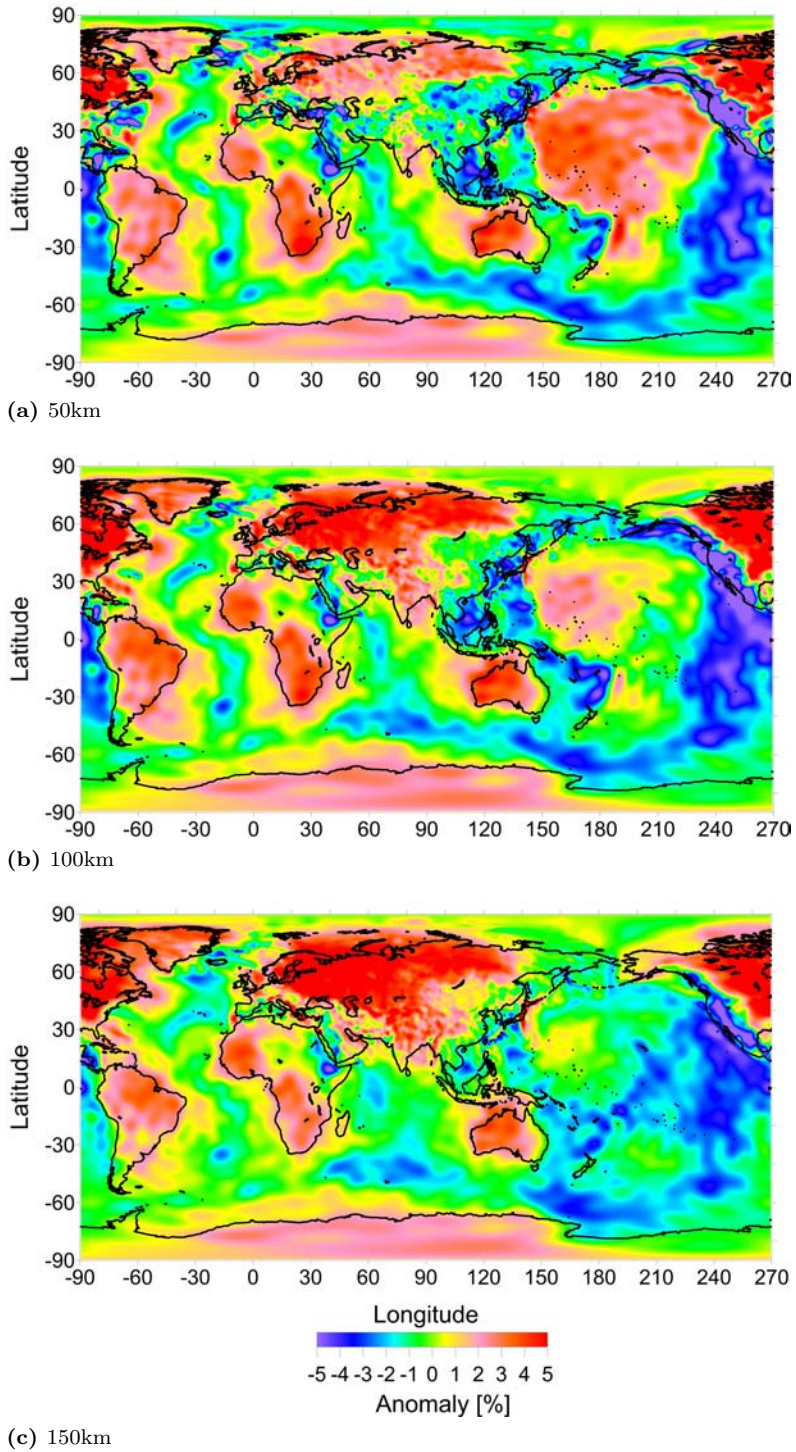


Figure 2.8: S-wave velocity anomalies at different depths for the combined model

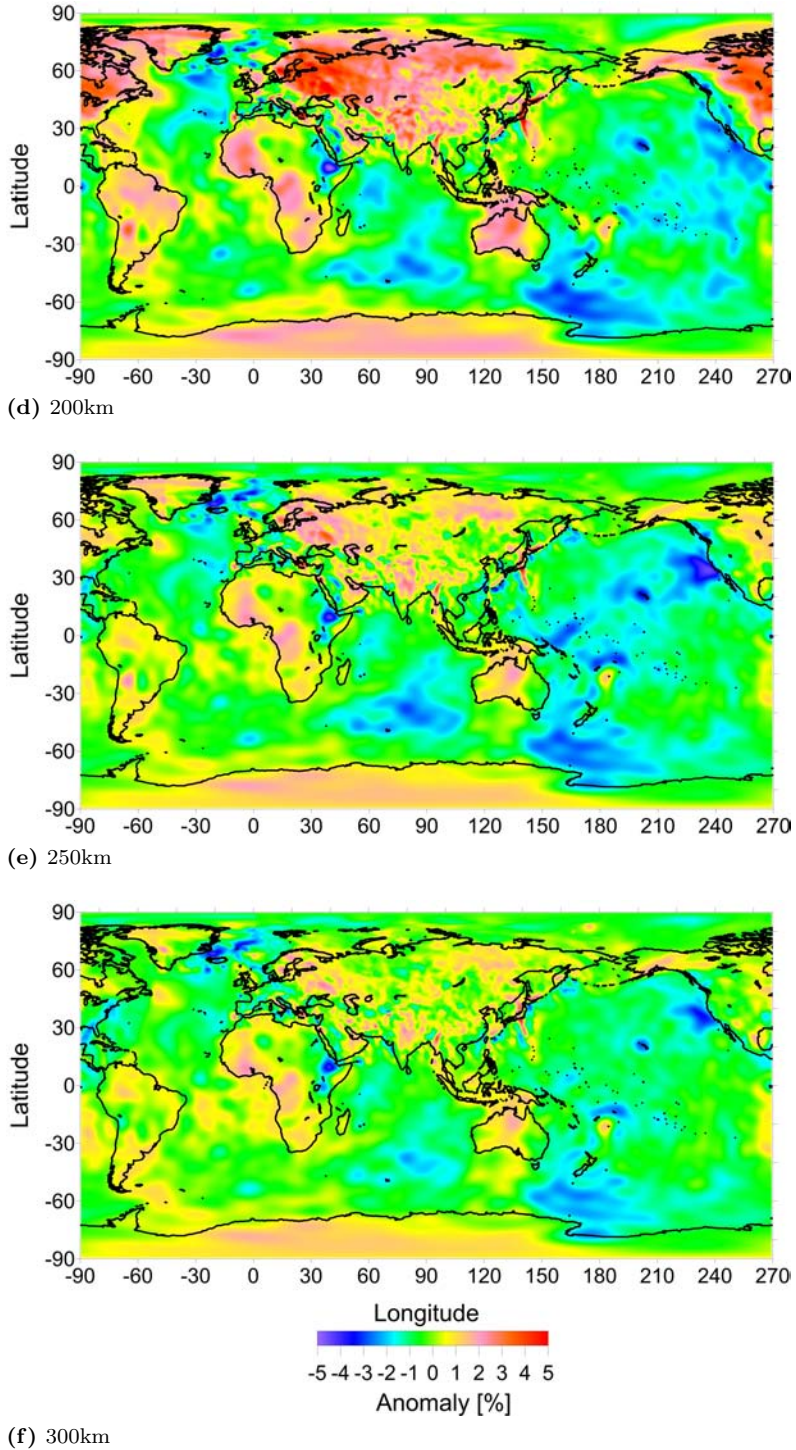


Figure 2.8: S-wave velocity anomalies at different depths for the combined model (continued)

2.5 Gravitational data

The currently most up to date static global gravity field models are provided by the International Centre for Global Earth Models (ICGEM). This research uses the European Improved Gravity Field Model of the Earth by New Techniques (EIGEN)-6C [Förste et al., 2011] gravity field model (figure 2.9), which combines satellite tracking data, gravity data and altimetry data to obtain a gravity field model up to spherical harmonic degree and order 1460. Satellite tracking data is provided by Laser Geodynamics Satellites (LAGEOS) and used in the lowest degrees of the model (up to spherical harmonic degree 30), whereas satellite gravity data from the Gravity Recovery And Climate Experiment (GRACE) and Gravity Field and Steady-State Ocean Circulation Explorer (GOCE) are used for degrees up to 130 and 240 respectively. Technical University of Denmark (DTU) gravity anomaly data is used for degrees 160 to 370 and DTU10 block diagonal data is used for degrees up to 1420. Since all modelling in this thesis will occur on a $1^\circ \times 1^\circ$ grid, the effective resolution of the gravity model is limited to $1^\circ \times 1^\circ$, or spherical harmonic degree 180, despite the higher resolution in the available dataset.

The gravity anomaly is the full gravity field minus a reference field. This reference field is the gravity field exerted by a laterally homogeneous earth (i.e. density ρ depends on depth, but is invariant with respect to latitude and longitude). The gravity anomaly is given in figure 2.9 and when in the remainder of this thesis the observed gravity field is referred to, this gravity anomaly is meant.

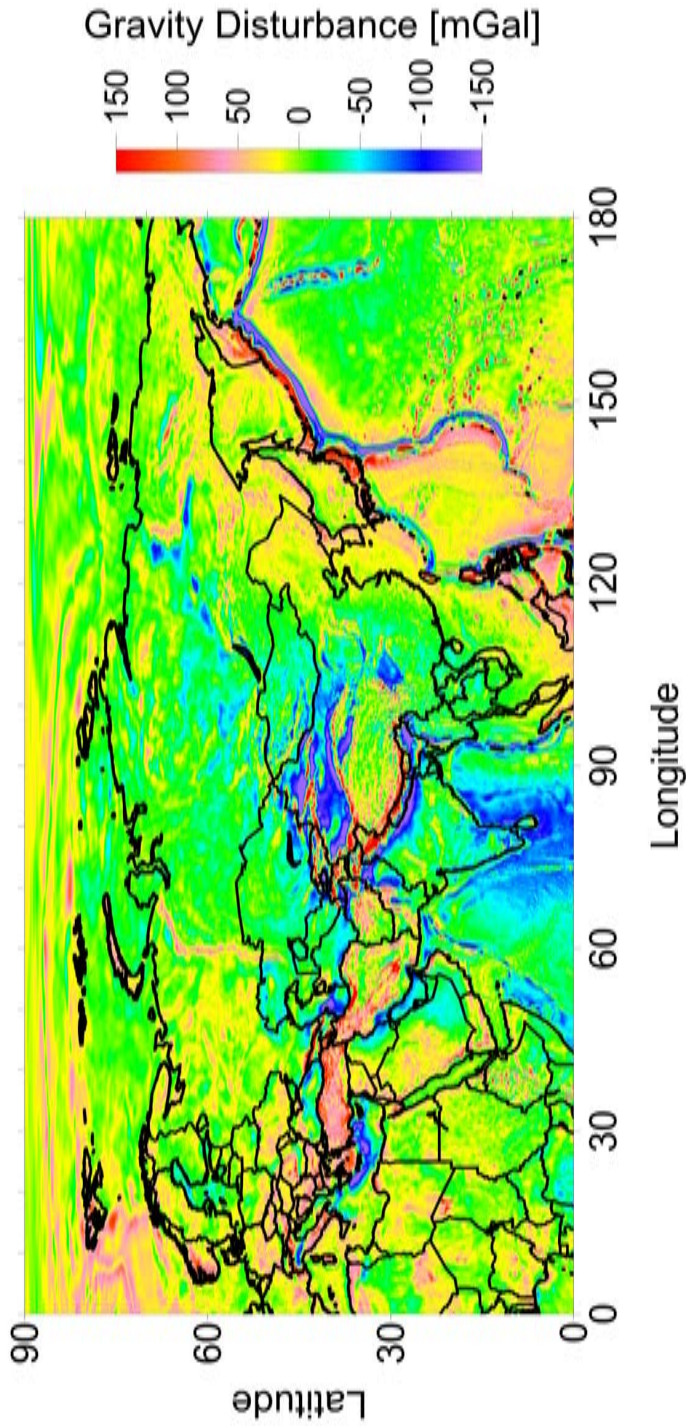


Figure 2.9: EIGEN-6C global gravity anomaly model from ICGEM [Förste et al., 2011]



Sediment velocity and density model

The topmost layer of the solid earth is the sedimentary cover. This layer is usually studied in much more detail than the crystalline crust. This is especially true for its thickness, see section 2.2. Numerous well-logs and geophysical prospecting data show a very complicated structure of sedimentary basins including additional interfaces within the sedimentary cover. However, it is in general not possible to join these interfaces into more regular boundaries. In constructing a crustal model for a region such as Asia, one is more interested in the large scale variations in properties of the sedimentary cover and less in local structures. A good approach to construct a sediment velocity and density model is to use a smooth velocity/density-depth relationship based on averaged borehole and seismic data and on sufficiently determined density-compaction relations (e.g. Jachens and Moring [1990], Langenheim and Jachens [1996], Artemjev and Kaban [1994], Kaban and Mooney [2001], Kaban et al. [2004]). This relationship should be specific for several general types of sedimentary regions depending on their structure and history. Subsequently, an average structure of any sedimentary region is reproduced with sufficient accuracy, while all small scale features are left for local studies.

3.1 Velocity-depth relation in sedimentary cover

In a basin filled with sediments, the density of the sediments generally increases with depth because of mechanical compaction. Furthermore the rate of compaction with depth decreases. Densities (ρ) can be derived from observed P-wave velocities (V_p) in sediments using e.g. the Nafe-Drake relation (N-D) [Ludwig et al., 1970] (equation 3.1) or Gardner's rule [Gardner et al., 1984] (equation 3.2). Both relations are used in e.g. Brocher [2005].

$$\rho_{N-D} = 1.6612V_p - 0.4721V_p^2 + 0.0671V_p^3 - 0.0043V_p^4 + 0.000106V_p^5 \quad (3.1)$$

$$\rho_{Gardner} = 1.74V_p^{0.25} \quad (3.2)$$

The increase of velocity, and thus density, with depth can then be approximated by relation 3.3.

$$V(z) = V_{surf} + (V_{max} - V_{surf}) \left(1 - e^{\frac{-3z}{z_{V_{max}}}}\right) \quad (3.3)$$

Parameter V_{surf} is the seismic velocity at the surface. Parameter $z_{V_{max}}$ describes how fast the wave velocity V_p approaches V_{max} with depth. V_{max} in the sedimentary layer was experimentally determined at 6km/s for V_p based on the data used in this study.

3.2 Division into regions and function fitting

The sediment thickness map (figure 2.2) is used to divide Asia into 24 main 'sedimentary' regions (figure 3.1a), with each region generally defined as having a thick sedimentary cover in the centre and a shallow cover at the border. In some cases neighbouring small regions with little data have been joined together, e.g. the East China region. The sedimentary cover is then analysed per region.

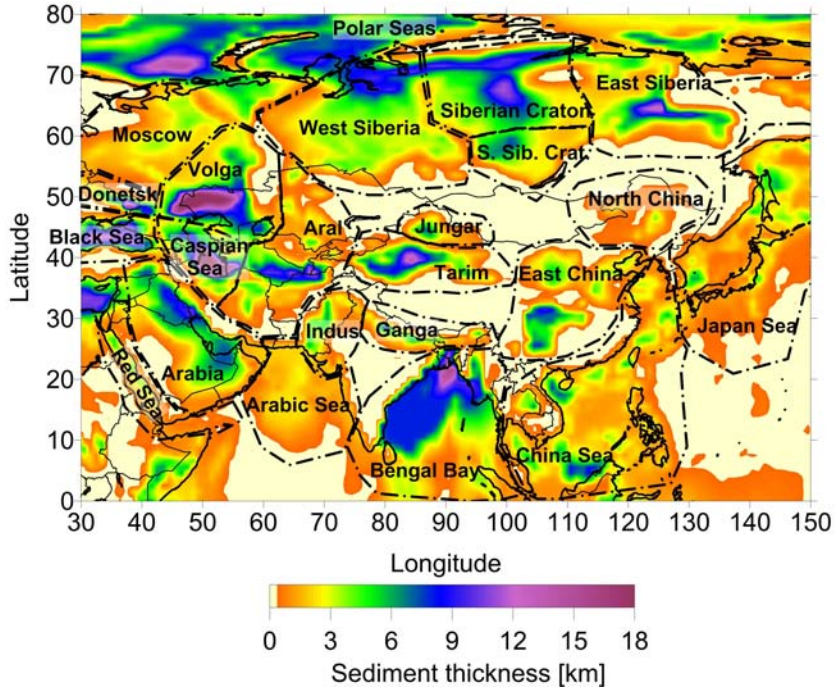
First all data inside a sedimentary region are selected, see figure 3.1b. Before fitting the function 3.3 the selected (V, z) -pairs are binned over 0.1km depth-intervals, a process in which all data inside a single bin are replaced with a representative value (in this case the arithmetic mean) at the centre of the bin. This is done to prevent a cluster of data points, covering a small depth range, from dominating the shape of the function. For a broader discussion of this process, see appendix A.

Next, for each region a Least Squares (LS) estimate is used to determine which V_{surf} and $z_{V_{max}}$ lead to the best fit with the averaged (binned) (V, z) -pairs located within the sedimentary cover. The results are given in figure 3.2. Estimated V_{surf} and $z_{V_{max}}$ for each basin are given in table 3.1, together with the number of averaged data points and R^2 , a measure for the quality of the fit, see also appendix B.

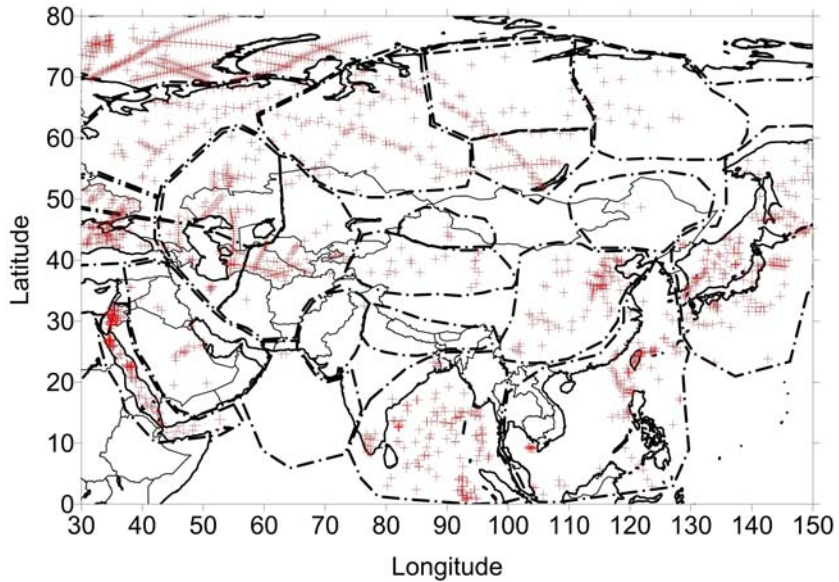
3.3 Analysis of results

For some regions the amount of available data is insufficient to reliably determine the parameters V_{max} and $z_{V_{max}}$ (e.g. Arabic Sea, Ganga, Indus, table 3.1), for some other regions the data does not regress well to the applied function (e.g. East Siberia), figure 3.2 and table 3.1. For these regions velocity and density functions have been adopted from regions with a comparable tectonic and basin evolution history (see table 3.2).

For comparison, all well resolved velocity-depth functions can be plotted in a single graph. Both the oceanic basins (figure 3.3) and the continental basins (figure 3.4) can be classified into three characteristic groups, see table 3.3. 'Slow' regions are characterized by low velocity (and thus density) near the surface, and rapidly increasing velocity/density with depth; examples are the Bengal Bay and Japan Sea for oceanic regions and the Aral Sea and East China basins for continental regions. The second group of 'intermediate' regions, has



(a) thickness of the sedimentary cover (same as figure 2.2)



(b) available data per sedimentary region

Figure 3.1: Division of the study area into 'sedimentary' regions

Table 3.1: Estimated V_{surf} and z_{Vmax} parameters for each region

Region	n_{obs}	V_{surf}	z_{Vmax}	R^2
Arabia	13	4.07	26.45	0.05
Arabic Sea	1	-0.50	6.65	n.a.
Aral	52	2.08	10.98	0.69
Bengal Bay	44	1.28	10.32	0.85
Black Sea	66	2.72	25.14	0.33
Caspian Sea	53	2.46	13.95	0.63
South and East China Sea	28	2.31	14.43	0.69
Donetsk	20	2.36	8.94	0.58
East China	34	2.96	8.43	0.51
East Siberia	14	4.34	86.80	0.004
Ganga	0	n.a.	n.a.	n.a.
Indus	1	3.04	3.04	n.a.
Japan Sea	37	1.52	9.16	0.77
Jungar	4	4.83	19384	0.000
Moscow	25	3.50	39.61	0.10
North China	2	4.90	11584	0.000
Polar Seas	89	2.62	11.30	0.88
Red Sea	34	3.03	9.17	0.58
Siberian Craton	37	4.65	9.79	0.17
South Siberian Craton	25	4.22	6.23	0.41
Tarim Basin	15	4.19	19.90	0.14
Volga	68	3.15	16.03	0.68
West Siberia Basin	50	3.39	26.27	0.21

Table 3.2: Unresolved regions with overall resemblance to well resolved regions

Unresolved region	Well resolved region
Arabia	West Siberia Basin
Arabic Sea	Bengal Bay
East Siberia	Siberian Craton
Ganga	Aral
Indus	Aral
Jungar	South Siberian Craton
Moscow	Volga
North China	East China
Tarim Basin	Volga

intermediate velocities and densities near the surface, and a small gradient with depth; examples are the oceanic Black Sea basin and the Volga and West Siberia basins in continental settings. The last group, the 'fast' regions, show a relative high velocity near the surface and a steep gradient towards V_{max} ($6km/s$) with depth; examples are the Red Sea and both basins on the Siberian craton.

The velocity-depth relations have been converted to density-depth relations,

Table 3.3: Division of regions in slow, intermediate and fast

Setting	Slow	Intermediate	Fast
Oceanic	Arabic Sea Bengal Bay Japan Sea	Black Sea	Caspian Sea South and East China Sea Polar Seas Red Sea
Continental	Aral Sea Donetsk East China Ganga Indus North China	Arabia Moscow Tarim Volga West Siberia	East Siberia Siberian Craton South Siberian Craton

taking the average between the Nafe-Drake relation (equation 3.1) and Gardner's Rule (equation 3.2). In combination with the sediment thickness map (figure 2.2), the average velocity (figure 3.5a) as well as the average density (figure 3.5b) can be computed at each location. This density model of the sedimentary cover of Asia is subsequently used in the construction of the depth-to-Moho model (chapter 4).

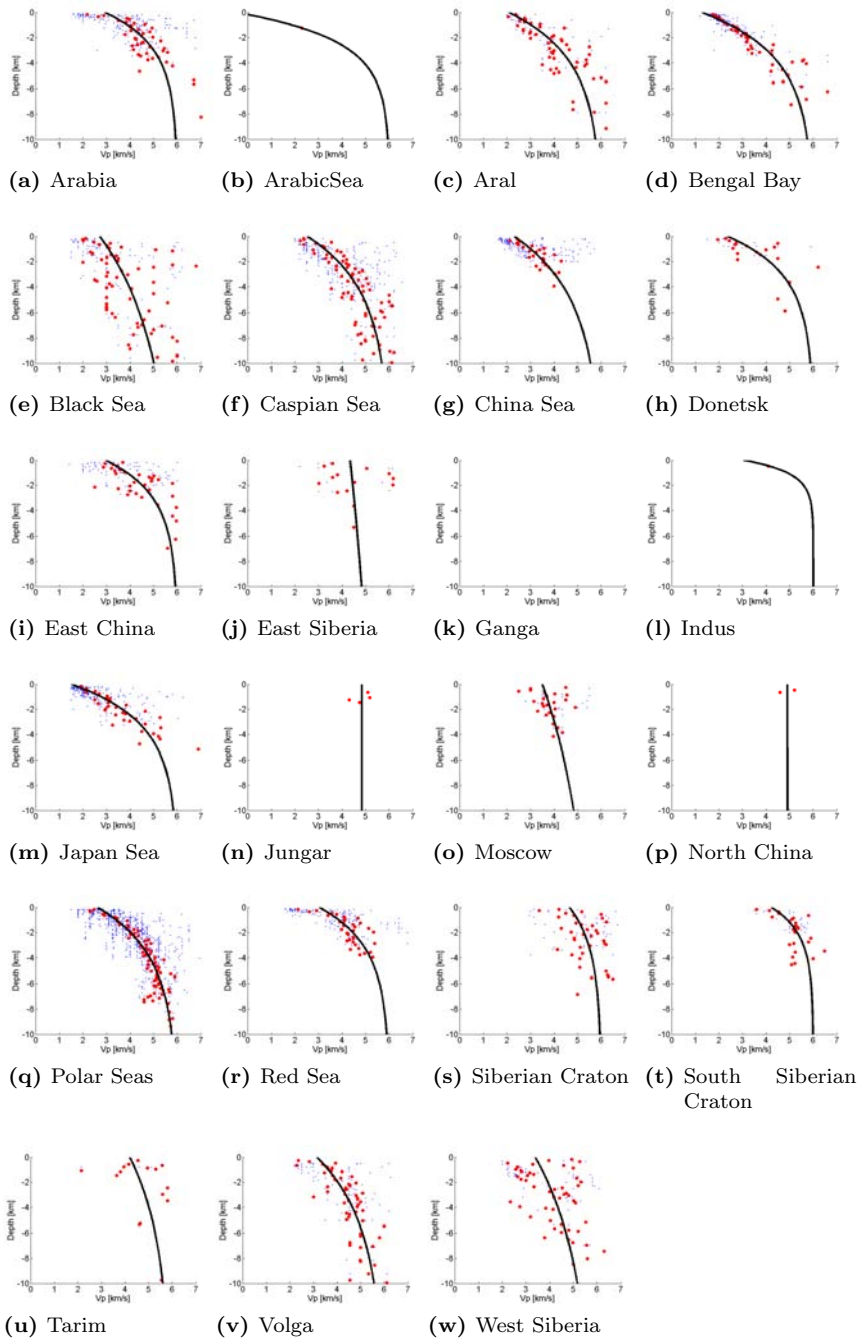


Figure 3.2: Estimated velocity-depth relations in the sedimentary cover for the different regions. Original observations (black dots) are averaged in 0.1km wide bins (red dots). The function is fitted through the averaged observations (black lines)

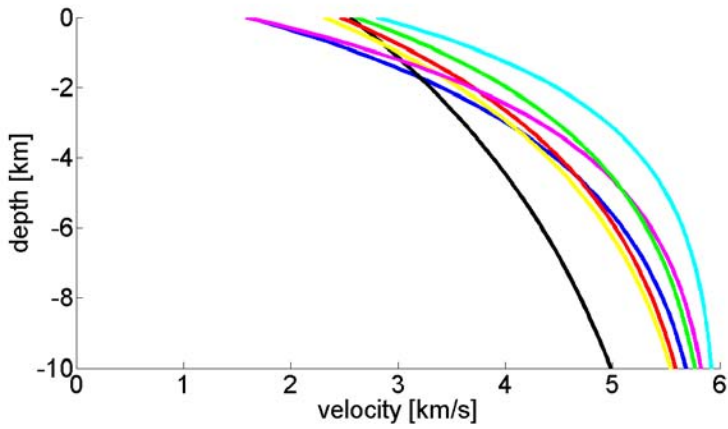


Figure 3.3: Velocity-depth functions for oceanic regions [blue = Bengal Bay; black = Black Sea; red = Caspian Sea; yellow = China Sea; magenta = Japan Sea; green = Polar Seas; cyan = Red Sea]

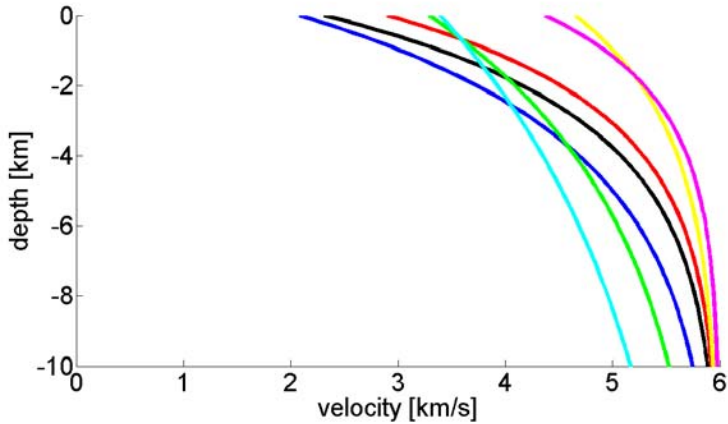
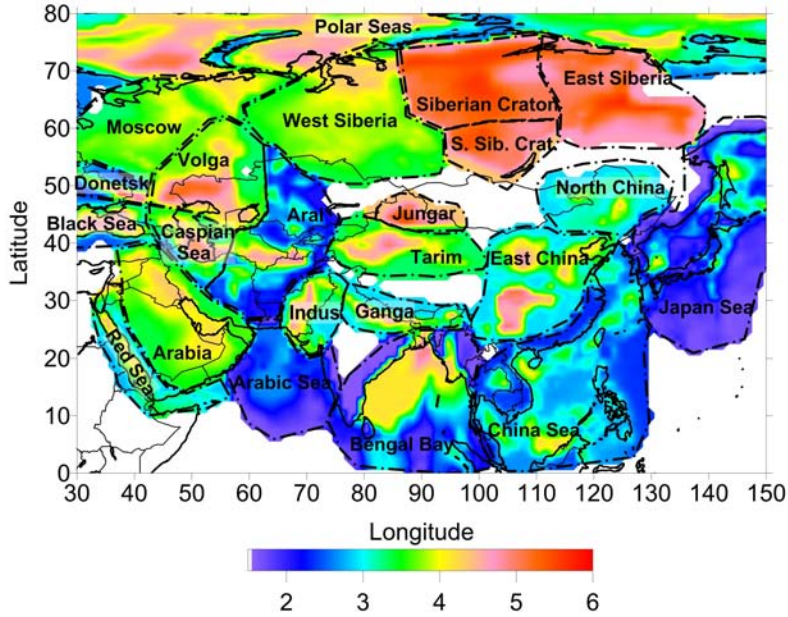
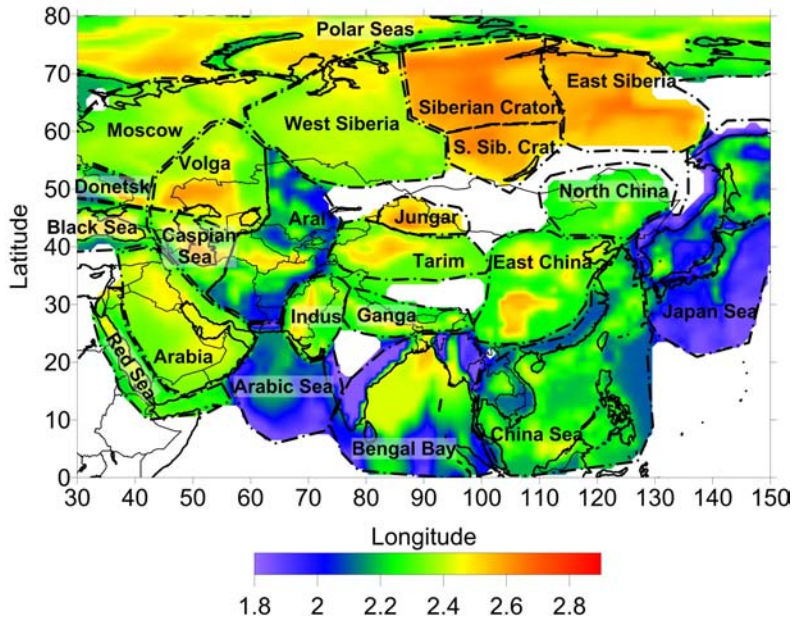


Figure 3.4: Velocity-depth functions for continental regions [blue = Aral; black = Donetsk; red = East China; yellow = Siberian Craton; magenta = South Siberia Craton; green = Volga; cyan = West Siberia]



(a) average V_p (km/s) of sedimentary cover



(b) average sediment densities (kg/m^3)

Figure 3.5: New model of average velocities and densities in the sedimentary cover of Asia [Please note that for some regions the velocity-depth relation was not well resolved (see tables 3.1 3.2), and this may lead to higher than average inaccuracies in the sediment model in these regions]



Depth to Moho

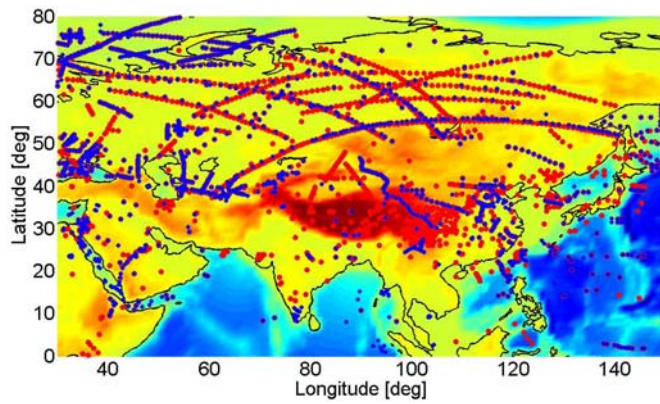
An accurate assessment of the depth to the Moho discontinuity is of primary importance to investigate the thermo-mechanical behaviour of the crystalline crust, and to assess the crustal contribution to the rheological strength of the lithosphere [Tesauro et al., 2007, 2008, 2009, Cloetingh et al., 2005, Burov, 2011, Tesauro et al., 2012]. Since the distribution of Moho depth observations in Asia is very inhomogeneous (see figures 4.1a and 4.1b), simply patching a Moho map from different regional studies would lead to unacceptable differences in quality of the model throughout the study area. Therefore a new method to interpolate the Moho observations in Asia is proposed. This method is analogous to the remove-compute-restore technique used in geoid modelling (e.g. Forsberg and Tscherning [1997]).

Figure 4.1c shows all Moho depth observations, projected on a W-E running vertical profile, as if looking through the crust from South to North. The variance in the observed Moho depths is clearly large. Many crustal thickness studies show that part of the variations in Moho depth can be related to (partial) isostatic balancing of the crust. The application of the remove-compute-restore technique presented in this chapter aims to remove, to the first order, this factor which dominates the observed variations in depth to Moho at short wavelengths. With this new method, therefore, it will be possible to construct a more robust and reliable Moho depth model.

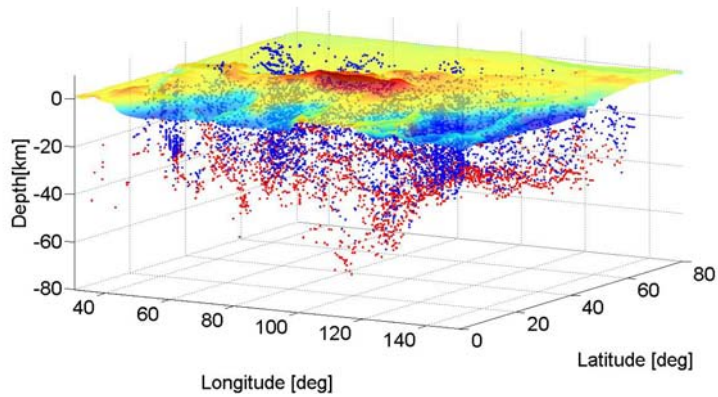
The proposed modified version of the remove-compute-restore technique consists of three steps, that are illustrated in figure 4.2 and will be described in more detail in the sections below. Starting from the original observations (figure 4.2a), first the isostatic topographic effect is removed, leading to residual observations (figure 4.2b, section 4.1). Secondly, the residual observations can be interpolated with less uncertainty, since the variance between observations is reduced (figure 4.2c, section 4.2). Finally, the removed isostatic topographic effect is restored to the interpolated Moho depth, leading to the full interpolated depth to Moho (figure 4.2d, section 4.3).

4.1 Remove isostatic topographic effect

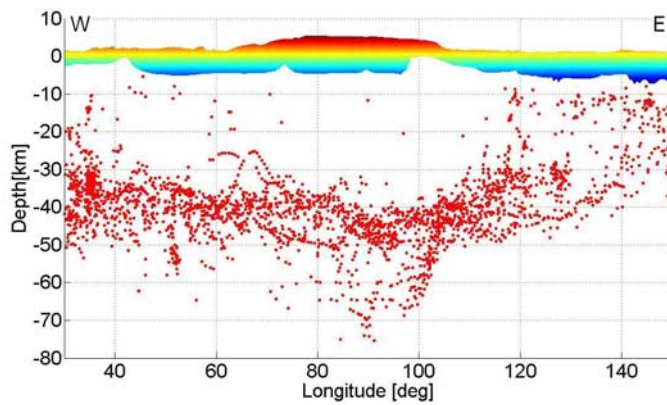
It is reasonable to assume that some part of the Moho variation is related to the surface load providing part of the isostatic compensation. Therefore, first



(a) Locations of depth to Moho data (red = M_{obs} , blue = V_p)



(b) oblique 3D view of data



(c) East-West profile with projected depths to Moho

Figure 4.1: Available Moho depth observations in the study area

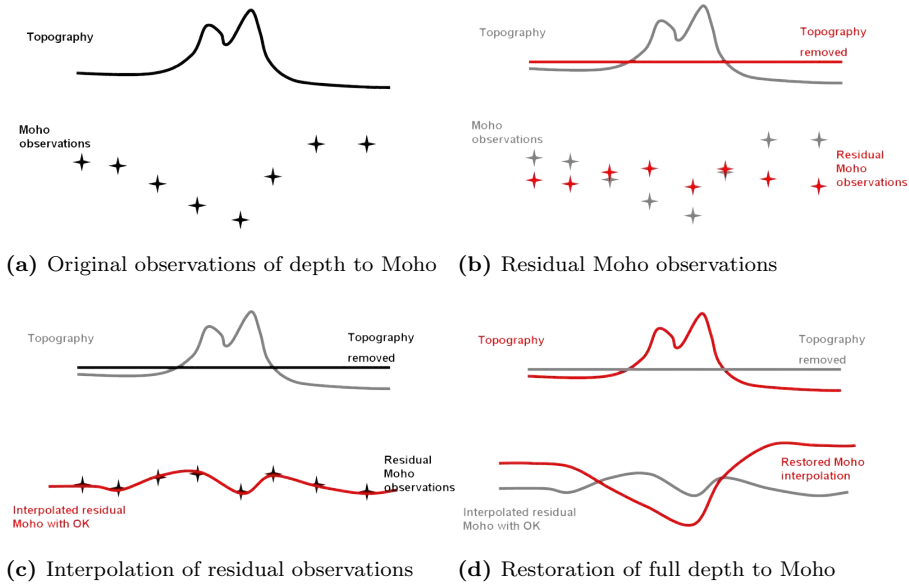


Figure 4.2: Principles of the remove-compute-restore technique

the deflection of the Moho due to the effect of the surface load, represented by topography/bathymetry and sediment heterogeneity, is removed from the Moho observations, resulting in residual Moho observations (M_{res}), figure 4.2b. These residual Moho observations are computed using equation 4.1, which is based on the original Moho observations (M_{obs}), corrected for local Airy isostasy due to the adjusted topography.

$$M_{res} = M_{obs} + \frac{\rho_{uppercrust}}{\rho_{lowercrust} - \rho_{mantle}} h_{adj} \quad (4.1)$$

The type of the isostatic compensation is not critical (as has been proven by several tests) since the applied correction is returned to the interpolated field later in the process. Reference values are used for the density of the upper crust ($\rho_{uppercrust}$), $2.67g/cm^3$, the average density of the lower crystalline crust ($\rho_{lowercrust}$), $2.85g/cm^3$, the density for the lithospheric mantle, (ρ_{mantle}), $3.32g/cm^3$ [Kaban et al., 2004].

Adjusted topography (h_{adj} in equation 4.1) represents the total surface load (e.g. Artemjev et al. [1994], Artemjev and Kaban [1994]). The adjusted topography is obtained by subtracting from the topography (h) the change in topography when sediments (ρ_{sed}) and water (ρ_{water}) are numerically densified to the normal upper crust density ($\rho_{uppercrust}$) $2.67g/cm^3$ (equation 4.2).

$$h_{adj} = h - \int_0^{t_{sed}} t \frac{\rho_{sed}}{\rho_{uppercrust}} dt - \int_0^{t_{water}} t \frac{\rho_{water}}{\rho_{uppercrust}} dt \quad (4.2)$$

In equation 4.2 t_{sed} and t_{water} are the thickness of the sediment and water

layers respectively.

4.2 Compute residual depth to Moho on regular grid

In the second step local Ordinary Kriging (OK) is used to interpolate the residual observations on a regular $1^\circ \times 1^\circ$ grid. Local OK is a standard method for interpolation and consists of three steps: data selection, obtaining covariance function, Ordinary Kriging. For each grid point at which the depth to residual Moho is interpolated these three steps are performed, then the interpolation moves to the next grid point.

First all data within a certain radius (R) around the grid point (in this study $R = 10^{circ}$) is selected. Next, the experimental covariance is determined between each pair of observations, $\text{cov}(M_{obs,i}, M_{obs,j})$. These observations are ordered according to the distance, $d(M_{obs,i}, M_{obs,j})$, between the two observations, leading to d -cov-pairs, $[d(M_{obs,i}, M_{obs,j}), \text{cov}(M_{obs,i}, M_{obs,j})]$. A positive definite spherical covariance model, where $\text{Cov}(d)$ is the modelled covariance as function of distance d (equation 4.3) is fitted through the d -cov-pairs.

$$\text{Cov}(d) = c_0 \left(1 - \frac{3d}{2c_{range}} + \frac{d^3}{c_{range}^3} \right) \quad (4.3)$$

The spherical covariance function, equation (4.3) is determined by two parameters. The first, c_0 , determines the covariance at the origin ($d=0$), the second, c_{range} , defines the distance at which the covariance becomes zero. This covariance function is the basis for the weight distribution between the observations (M_{res}) in the OK-scheme and leads to an estimation of the Moho depth (M) at the interpolation grid point. Furthermore, it allows for an estimation of the uncertainty of the estimated Moho depth. A more in depth discussion of both the use of covariance functions and OK itself can be found in appendix C.

The residual depth to Moho interpolation is given in figure 4.3. The standard deviation σ_{std} (the square root of the variance) of the estimation is given in figure 4.4a. It is in this variance estimation that the advantage of interpolating the residual Moho observations, rather than the original observations, is most pronounced. When comparing figure 4.4a to figure 4.4b, a reduction of the estimation variance of on average 30% can be observed, indicating that the model using the remove-compute-restore significantly improves the reliability of the interpolated Moho topography model.

4.3 Restore topographic adjustment

Finally, the isostatic correction, removed from the observations using equation 4.1, is restored to the interpolated residual Moho, using equation 4.4, which is the inverse of equation 4.1.

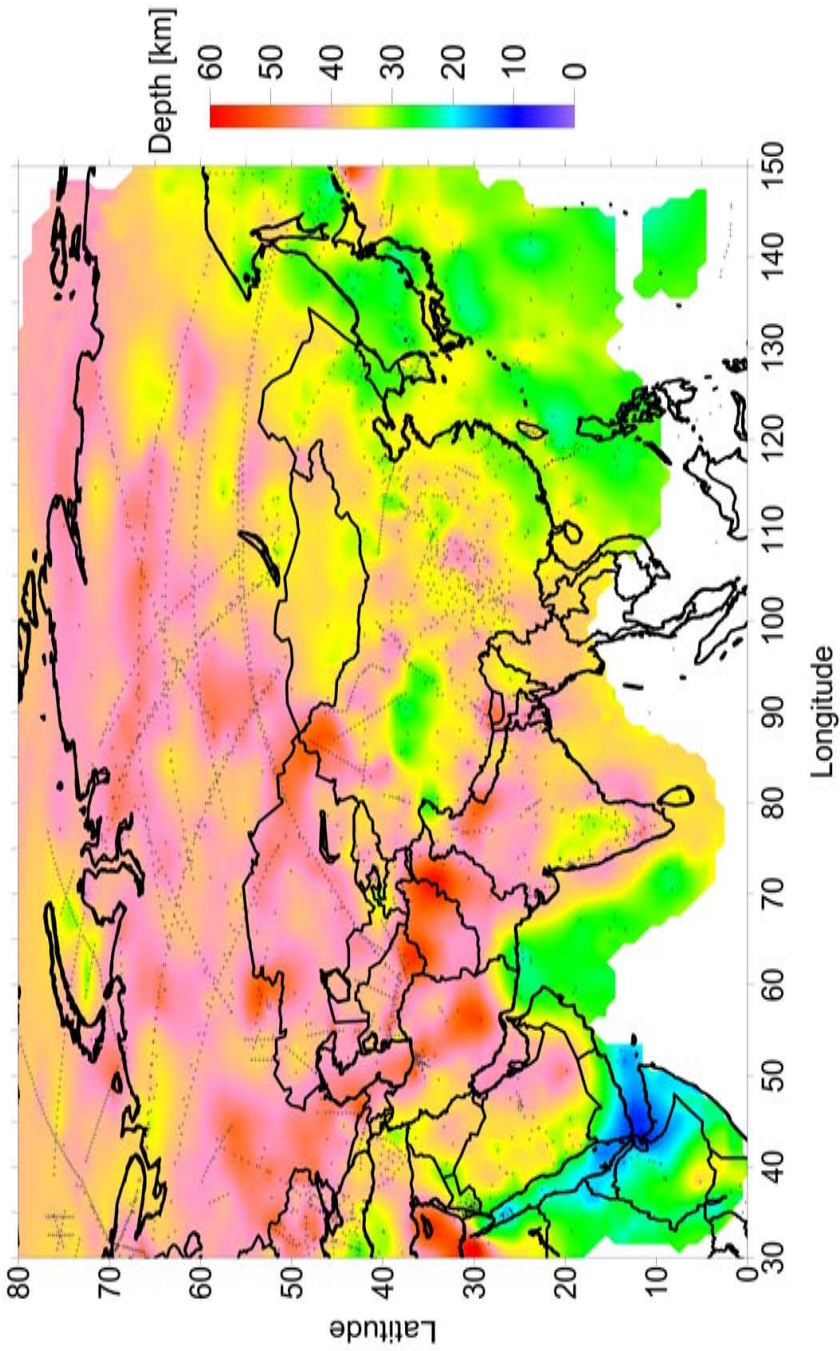
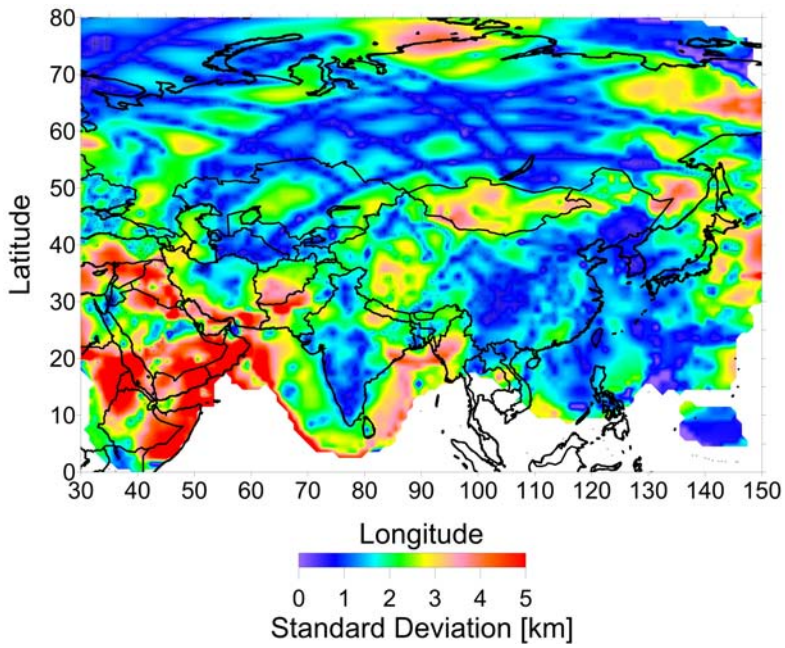
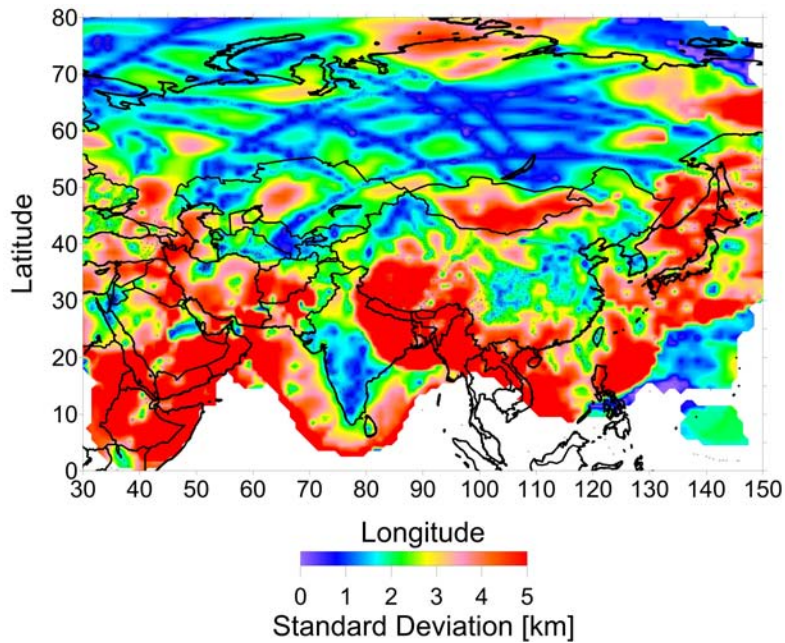


Figure 4.3: Interpolated residual depths to Moho, in *km*



(a) For interpolation based on residual Moho observations



(b) For interpolation based on actual Moho observations, for reference

Figure 4.4: Standard deviations (σ_{std}) for estimation of depth to Moho, in *km*

$$M = M_{res} - \frac{\rho_{uppercrust}}{\rho_{lowercrust} - \rho_{mantle}} h_{adj} \quad (4.4)$$

4.4 Quality control

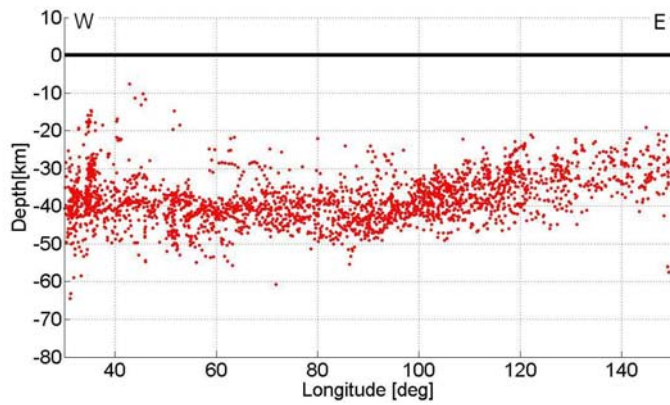
All observations are also checked for coherence with neighbouring observations, by estimating the Moho depth, using local OK at the observation location on the residual observations. In this estimation, all surrounding observations are used, except for the observation that is under review. Since the expected standard deviation can also be estimated, the difference between the estimation and the actual observation can be expressed relative to this standard deviation. If the absolute difference is more than twice the variance (95% confidence interval), and more than $5km$ (considered as a reasonable deviation in the estimation due to abrupt local changes in Moho topography), the observation is flagged as outlier and disregarded.

An undesired side-effect of this approach is that inaccurate observations can lead to the flagging of neighbouring observations that however are of acceptable quality. To prevent this effect all flagged observations are re-evaluated using the same method, but now disregarding all previously flagged observations. Observations that are still flagged are removed from the dataset; observations that are not flagged in this second iteration are restored and used in the Moho estimation.

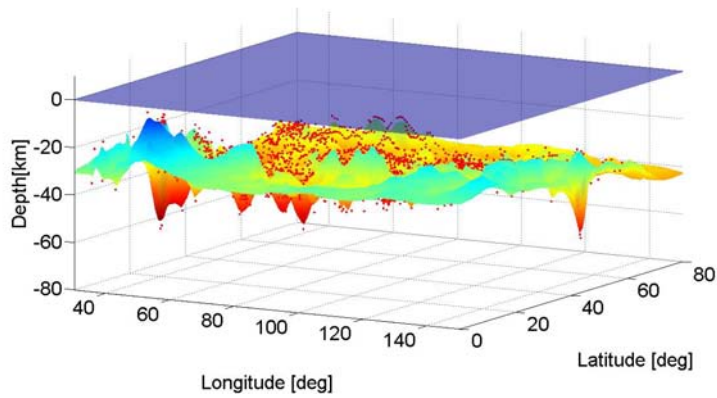
4.5 Discussion of Results

The three steps of the remove-compute-restore technique have been applied to the available Moho depth observations (section 2.3) for the study area. First the effects of the surface topography, sediment and water loading are removed from the observations (figure 4.5a). Secondly, the residual observations are interpolated (figure 4.5b). Finally the effects of surface topography, sediment and water loading are restored (figure 4.5c).

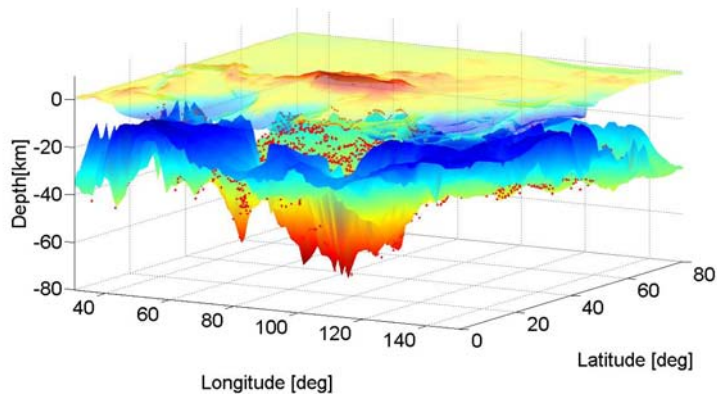
The new crustal Moho depth model for Asia is also presented in figure 4.6. In agreement with previous crustal models [Bassin et al., 2000, Kaban et al., 2009], we find anomalous deep Moho ($> 50km$) running from the Anatolian Plateau in the west to the Tibetan Plateau ($> 60km$) in the east, coinciding with the Alpine-Himalayan convergence zone. The increasing depth to Moho in the Zagros mountain belt (Iran) is in agreement with Paul et al. [2010]. Another common anomalous feature is the deep Moho ($> 55km$) under the Tibetan Plateau, in line with recent observational studies [Zhang and Klemperer, 2010]. The largest reconstructed Moho depths are found in the convergence zone just west of the Tarim Basin and at the southern edge of the Tibetan Plateau (both $75km$), in accordance with Li et al. [2006] and recent studies of e.g. Ruigrok and Wapenaar [2012]. However, we also find strong heterogeneities in Moho depth in the intra-continental domains north and south of the Alpine-Himalayan convergence zone.



(a) Residual Moho observations



(b) Residual interpolated depth to Moho



(c) Restored interpolated depth to Moho

Figure 4.5: Application of the remove-compute-restore method to the actual data

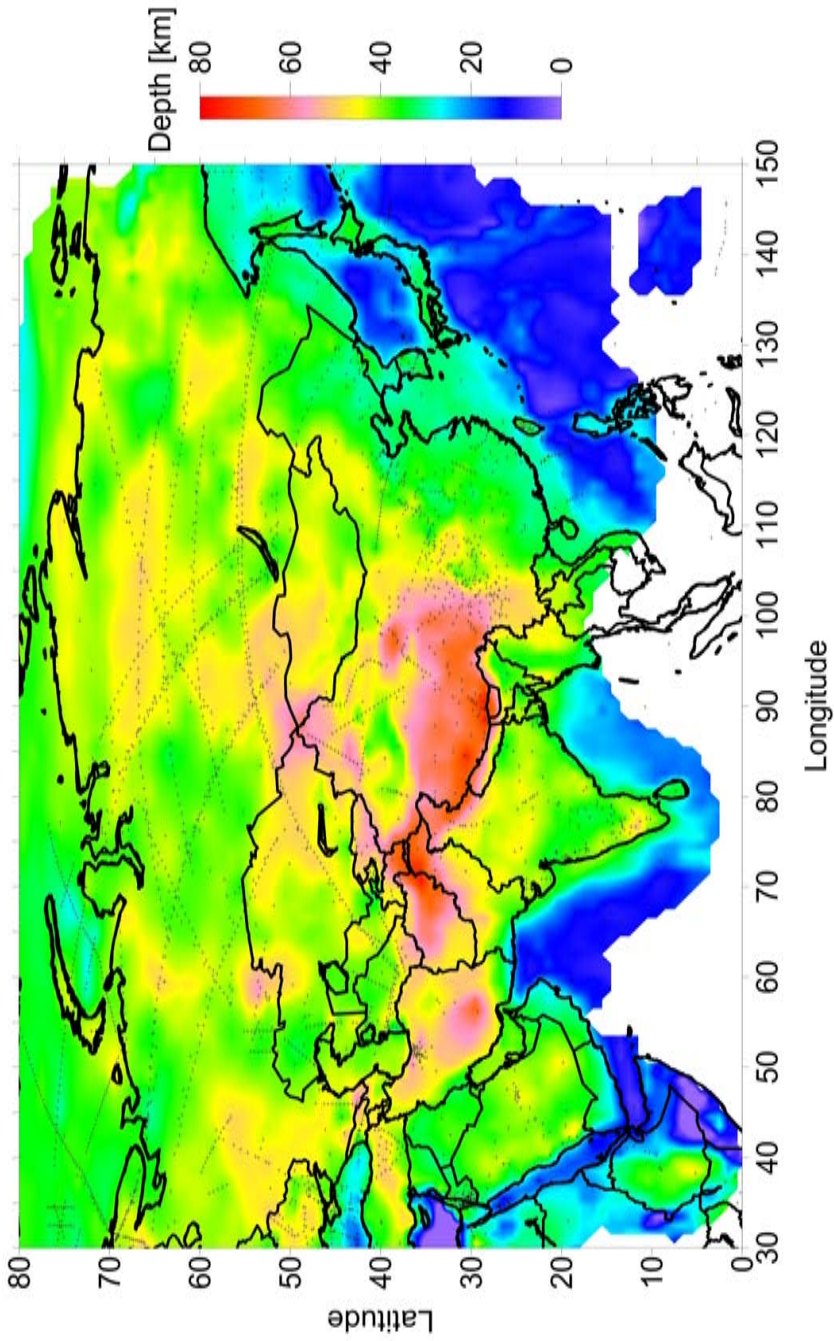


Figure 4.6: Interpolated and restored depth to Moho, in *km*

A major intraplate feature is a zone in Central Asia with a deep Moho extending from just west of the Tarim Basin to just west of Lake Baikal (55 – 60km), and clearly separated from the Tibetan Plateau by a shallow Moho in the Tarim Basin (35 – 40km), slightly shallower than in Li et al. [2006]. The anomalous deep Moho in Central Asia coincides with a region of major Cenozoic intraplate tectonic deformation that occurs in response to the collision between the India subcontinent and the Eurasian plate [Delvaux et al., 2013, Smit et al., 2013]. Intraplate deformation in Central Asia is characterized by large-scale lithosphere folding [Nikishin et al., 1993, Burov et al., 1993] and the associated development of major compressional basins [Cloetingh et al., 1999, 2002, Cloetingh and Burov, 2011, Delvaux et al., 2013]. The presence of long-wavelength lithosphere folds, amplified by infill of sediments, could provide an explanation for the deeper Moho in this intra-continental area.

Further to the north-west, the Ural Mountains, well constrained by data [Sollogub et al., 1980, Zverev and Kosminskaya, 1980, Khalevin et al., 1987, Belousov et al., 1991, Egorkin, 1991, GEON, 1992, Stadlander et al., 1999, Ayala et al., 2000] and therefore better resolved than in previous studies [Bassin et al., 2000, Kaban et al., 2009], also appears as an anomalous crustal structure. Here, Moho depth is varying heterogeneously, with a depth up to 50km for both the northern and southern Urals, in accordance with the URSEIS measurements [Brown et al., 2002, 2006, Brown, 2009], but with a substantially shallower Moho (up to 40km) for the central Urals. Other areas with anomalous deep Moho are found in the Siberian Craton and Platform (40 – 50km) and the East European Platform (43 – 48km). In contrast, areas with an anomalous shallow Moho are observed, for instance, in western Kazakhstan (34 – 40km) and under the West Siberian Basin (37 – 43km).

The high accuracy of the new Moho depth model is illustrated in figure 4.4a, which is a map of the standard deviation (σ_{std}) of the computed Moho depths. It shows that in large parts of the model the reconstructed Moho depth has an estimated 1σ -accuracy of less than 2km (95% confidence interval is $2\sigma = 4km$). Regions with lower accuracy are characterised by lack of data (Arabian Peninsula, Afghanistan and Pakistan, Mongolia and far east Russia), or by abrupt, large lateral variations in Moho depth (western China) which limits the correlation length of the data and increases the uncertainty of the estimation. Accuracy in these regions can be improved by increasing the amount of observational data.

Discrepancies between the model and observations can be determined by computing, when available, the average of the data for each grid point and comparing this average with the model value at the same grid point. Absolute difference between model and data is on average 3.9km for CRUST2.0 [Bassin et al., 2000], 3.2km for Kaban et al. [2009] Kaban et al. (2009) and 1.4km for the new model presented here. The distribution of the discrepancies is given in figure 4.7.

A quantitative analysis of different crustal types (shield, platform, orogen, basin large igneous province (LIP) and extended crust) shows us that, on average, the Moho is deepest underneath orogenic areas (47.3km, table 4.1) and also the largest spread ($\sigma_{std} = 8.8km$) occurs in these areas. Not surprisingly, also the thickness of the crust, measured from the sedimentary basement to Moho is

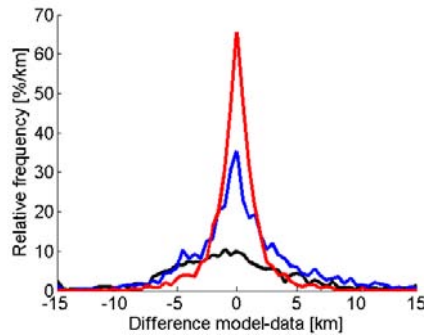


Figure 4.7: Distribution of relative frequency [%/km] of the discrepancy between Moho data and model (black = CRUST2.0 [Bassin et al., 2000]; blue = Kaban et al. [2009]; red = this model)

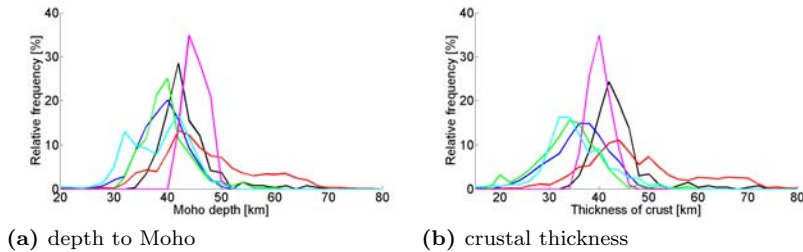


Figure 4.8: Histograms of the distribution of depth to Moho and thickness of the crystalline crust (black = shield, dark blue = platform, red = orogen, green = basin, purple = large igneous province, light blue = extended crust)

largest in orogenic areas (47.6km). In shield areas, both the thickness and depth to Moho is slightly less than in orogenic areas (43.3km and 43.7km respectively). The thinnest crust is found under basins (33.8km on average), whereas the shallowest Moho is to be found in extensional settings (38.1km). Depth to Moho in extensional settings shows two peaks in the distribution plot, figure 4.8a. The peak around 30km corresponds to the lowland areas in eastern China and the peak between 40km and 45km corresponds to, amongst others, the anomalous intra continental Lake Baikal area (e.g. Nielsen and Thybo [2009], Thybo and Nielsen [2009]).

Table 4.1: Comparison of parameter averages between geological provinces (values between brackets are standard deviations)

Type	#obs	Moho [km]	t_{crust}
Shield	263	43.3 (5.0)	43.7 (5.6)
Platform	1889	39.2 (4.3)	36.0 (5.7)
Orogen	1318	47.3 (8.8)	47.6 (10.8)
Basin	403	40.0 (4.5)	33.8 (6.6)
LIP	109	45.2 (2.0)	40.0 (2.1)
Extended	488	38.1 (6.1)	34.9 (7.3)



Crustal P-wave velocities

The crust is usually divided in several layers in which the P-wave velocity is (quasi-)constant. Common for larger crustal models is a division into three separate velocity layers (upper, middle and lower crust) [Egorkin, 1991, 1998, Mooney et al., 1998]. In each layer the velocity can vary laterally, but is assumed to be constant in the vertical direction. The velocity (V) depth (z) relation at a single location (longitude, latitude) can then be expressed as

$$V(z) = \begin{cases} V_{upper} & \text{if } z < z_{um} \\ V_{upper} + \Delta V_{um} & \text{if } z_{um} \leq z < z_{ml} \\ V_{upper} + \Delta V_{um} + \Delta V_{ml} & \text{if } z \geq z_{ml} \end{cases} \quad (5.1)$$

At each grid point the parameters V_{upper} , which is the velocity in the upper crust, the velocity increase between the upper and middle crust (ΔV_{um}), the increase between middle and lower crust (ΔV_{ml}) as well as the depth of the boundaries between upper and middle crust (z_{um}) and between middle and lower crust (z_{ml}) need to be determined. This is done in four steps. After some initial pre-processing, in which the depths are normalized (section 5.1), the second phase consists of determining z_{um} and z_{ml} (section 5.2). These boundaries are subsequently smoothed and in the third phase, V_{upper} , ΔV_{um} and ΔV_{ml} are determined (section 5.3). In the final post-processing phase, the velocities are corrected to reflect the independently determined average P-wave velocities in the crust, which can be assessed more accurately than the velocities in each single layer (section 5.4).

5.1 Phase 1: Normalizing depths

Because the crust usually is deformed, the normalized depths (\bar{z}) are more pronounced over larger regions than the absolute depths to the boundaries between upper and middle and between middle and lower crust. Therefore, normalized depths are more reliable to interpolate and thus will lead to a more robust crustal model. For this reason, all V - z observations are normalized relative to the local Moho depth and basement (sediment-crystalline crust interface) topography (0 depth is basement and 1 is Moho).

5.2 Phase 2: Determination of boundary depths

The second and third phases are methodologically equal. The goal in the second phase is to obtain a reliable estimate for the depth to the internal boundaries (z_{um} and z_{ml}). This is done by estimating all five free parameters in function 5.1, for each grid point. From these z_{um} and z_{ml} are extracted and post-processed. This process consists of five steps:

1. data selection
2. quality control
3. determination of weights
4. iterative LS analysis
5. post-processing

Firstly observations within a certain radius (R_{max}) of the grid point are selected. A maximum radius of 10° was found to be effective. The minimum number of observations required to make a reliable estimation is ten. When there are more than 200 observations present within R_{max} , the search radius is reduced, such that at the number of used observations lies between 50 and 200.

Secondly, the data are checked for consistency. An outlier check is performed at each grid point. Based on the scatter diagram of (V, z) -pairs (figure 5.1), a moving average (black line) with window size 20% is computed from 0% to 100% depth. The standard deviation (σ_{std}) of this moving average is computed as well. The assumption that over the short depth range of the window the observed velocity values are normally distributed implies that 95% of the data is expected to fall within $2\sigma_{std}$ from the moving average. The $2\sigma_{std}$ range is denoted by the pink lines in figure 5.1. Data points that fall outside the $2\sigma_{std}$ range are considered outliers and excluded from the estimation at the current location, though they could be included in estimations at other locations. Excluded observations are denoted with a small black dot in figure 5.1.

Thirdly each observation is assigned a weight (W) that is inversely proportional to the distance between observation location and grid point (d), according to equation 5.2. Thus observations located at the grid point would receive weight $W(0) = 1$ and observations on the edge of the selection circle receive weight $W(R) = 0$.

$$W(r) = 1 - \frac{d}{R} \quad (5.2)$$

In the fourth step, parameters V_{upper} , ΔV_{um} , ΔV_{ml} , z_{um} and z_{ml} are estimated such that the best fit of function 5.1 with the selected data is obtained, taking into account the weights $W(d)$. Since function 5.1 is highly non-linear, an iterative approach is used. In each iteration, the upper and lower boundaries (z_{um} and z_{ml}) are fixed and the other parameters are determined in a Least Squares (LS) sense. The residual misfit (σ_{fit}) between the function and the data

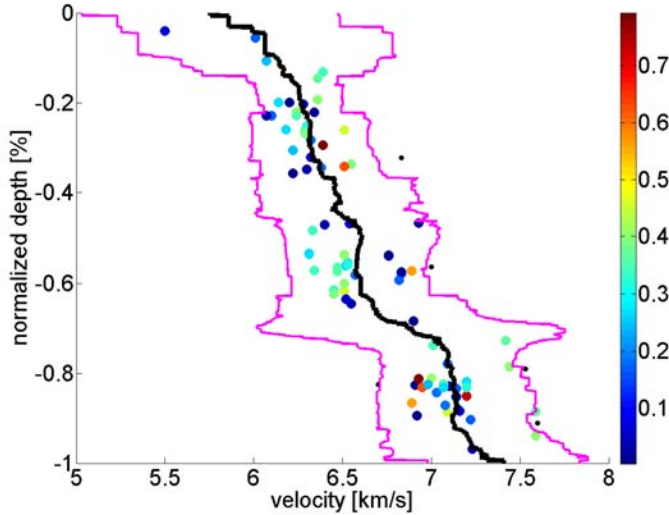


Figure 5.1: Quality check on (V, z) -pairs, dots are (V, z) -pairs (colours indicate weights), black line is moving average and pink lines are $2\sigma_{std}$ boundaries, small black dots denote rejected observations (see main text for explanation)

is measured and stored. In the next iteration the following pair of z_{um} and z_{ml} are evaluated.

In order to obtain a model that is robust with respect to slight variations and uncertainties in the data, the thickness of each velocity layer is constrained to be between 20% and 43% of the total crustal thickness at that grid point. Previous models have shown that over 98% of the crust is covered by this range [Bassin et al., 2000]. Thus the upper boundary (z_{um}) is varied between 20% and 43% of the total crustal thickness, with a step size of 1%. The lower boundary (z_{ml}) is varied from 57% to 80%, with the same step size. The same constraints - no velocity layer may be thinner than 20% or thicker than 43% - are also applied to the middle layer. Obviously the real crustal structure may be more complicated, the crystalline crust may consist of less (e.g. oceanic crust) or more than three layers (e.g. cratonic areas, where an additional high velocity layer at the bottom of the crust is usually implied). However our primary goal is to mathematically construct a model of the crust, which can be used in various geophysical applications. Therefore, like in most previous studies, we follow the general three layers division.

Finally the solution with the least residual misfit (σ_{fit}) is selected as the best solution. The upper and lower boundaries (z_{um} and z_{ml}) are retrieved and post-processed. Post-processing consists of smoothing the solution using a Gaussian filter and removal of some interpolation artefacts arising due to the inhomogeneous spread of the observations. The resulting boundaries are used in phase 3.

5.3 Phase 3: Determination of velocity profiles

The third phase resembles the second phase. Again function 5.1 is fitted to the original data. However, now only V_{upper} , ΔV_{um} and ΔV_{ml} are considered free parameters. Parameters z_{um} and z_{ml} are taken from the phase two and not solved for. Thus, the steps are still the same (data selection, quality assurance, determination of weights, LS analysis, post processing), but since the relation 5.1 is now a linear function of its free parameters, the LS analysis is straightforward and not iterative. The result is a velocity-depth profile for each grid point. In post-processing the solution can again be locally smoothed to remove interpolation artefacts, arising from the inhomogeneous spread of the observations.

5.4 Phase 4: Correction for average velocity

The average P-wave velocity can be more accurately estimated for an entire column of crust than for a separate crustal velocity layer, partially because the average crustal velocity can be more accurately measured and partially because more data is available. For this reason, the average velocity in the crust is determined, and the velocity profiles obtained previously are corrected to reflect the average velocity.

A map of average crustal velocities (figure 5.2) is obtained by applying the same local OK interpolation applied to Moho interpolation, see appendix C. Input data are obtained from both averaging velocities in a column of crust - when the velocity distribution is known for the entire column - and from independent data on average velocities, mainly along the deep seismic lines in Russia [Kaban, 2001].

The difference between the interpolated average crustal velocity and the average velocity of the velocity-depth profiles is computed. This difference is added to the velocity-depth profiles. Thus the average velocity of the velocity-depth profiles becomes the same as the interpolated average crustal velocity.

5.5 A new crustal velocity model for Asia

Figure 5.2 shows pronounced velocity heterogeneities throughout Asia. Three major regions with a characteristic velocity range can be identified: northern and western Asia, south-east Asia, and the Tibetan region. North-western Asia crust has average P-wave velocities ranging from $6.6 - 6.8 km/s$, while south-east Asia has velocities around $6.3 - 6.4 km/s$. In the Tibetan region, the average velocities are even smaller, around $6.2 km/s$.

Considerable heterogeneity is also observed in the thickness of the three crustal velocity layers, figures 5.3d, 5.3e and 5.3f as well as in the P-wave velocities in each layer, figures 5.3a, 5.3b and 5.3c. The velocity variation reflects the division into north-west Asia, south-east Asia and Tibet, observed in the

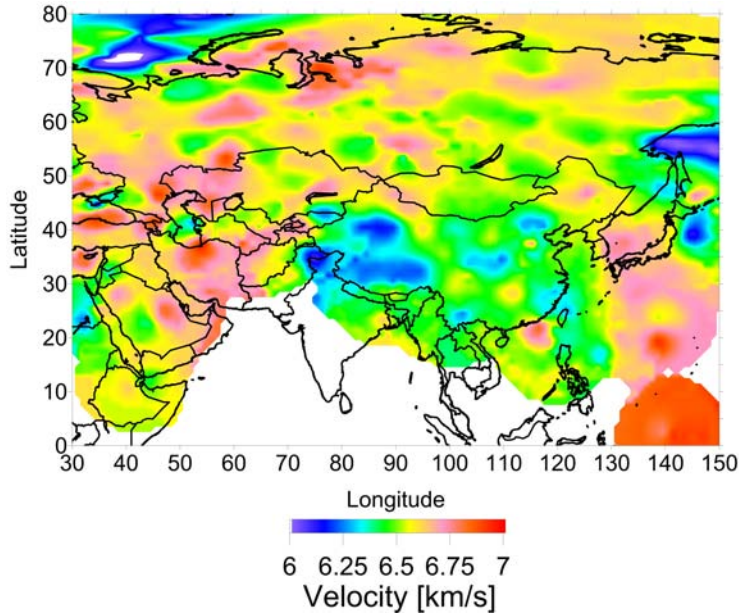


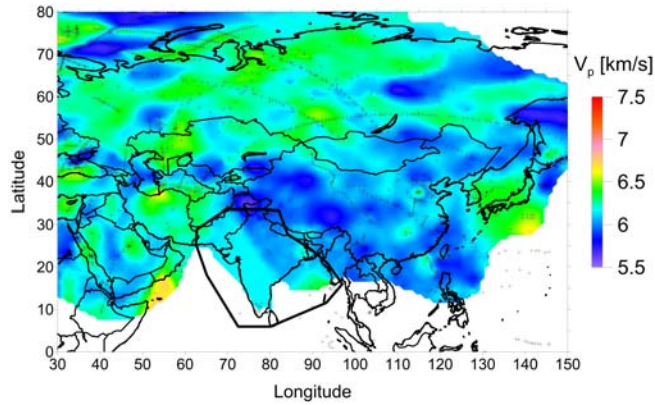
Figure 5.2: Average P-wave velocity in the crust

average velocities, figure 5.2. This is however less pronounced in the lower crust, figure 5.3c.

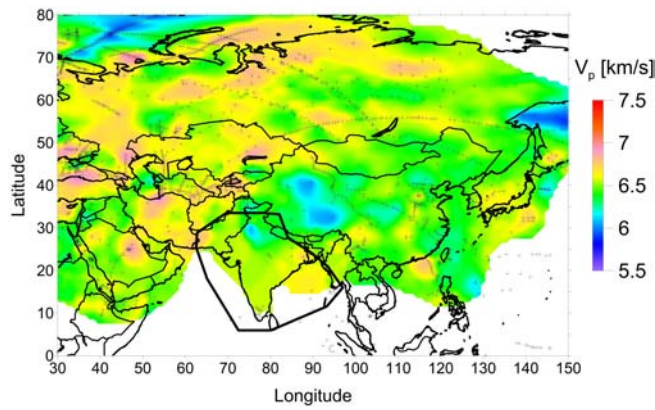
For the Indian subcontinent insufficient observations of crustal velocity are available to obtain a reliable crustal P-wave velocity model. A modified approach has been adopted in which both India and the rest of the modelled area are subdivided into different tectonic provinces, with each province characterised by a different crustal type (shield, platform, orogen, basin, LIP). For each tectonic province in India, the range of Moho depths (table 5.1) is established, using the new model. Average values for thickness and velocity of upper, middle and lower crustal velocity layers are obtained from regions outside India which have the same tectonic setting and with similar depth to Moho (table 5.2). These average values are used as velocity and thickness of upper, middle and lower crustal velocity layer in the Indian subcontinent. Post-processing consists of smoothing across the transition boundary (black line in figure 5.3) between India and the surrounding model.

Table 5.1: Depth to Moho for different crust types in India

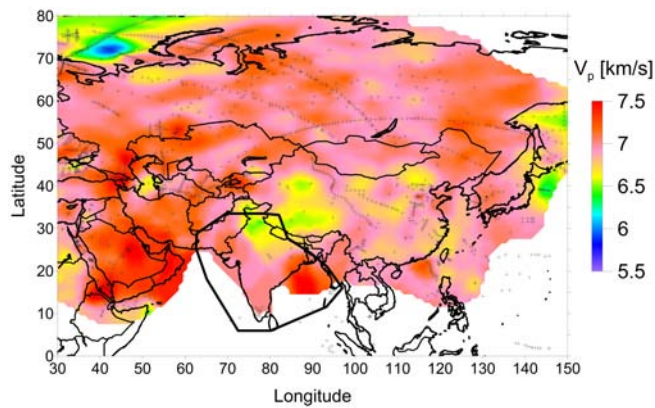
Type	z [km]	σ_{std} [km]	range [km]
Shield	36.6	4.5	30-45
Platform	40.0	2.3	37-43
Orogen	52.1	14.3	40-80
Basin	41.5	4.9	35-45
LIP	40.1	2.5	35-45



(a) upper

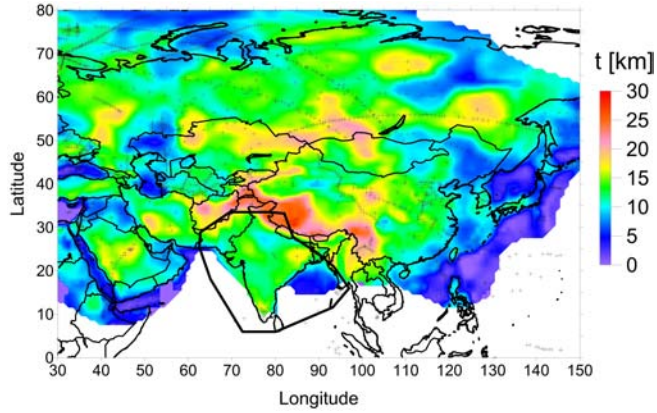


(b) middle

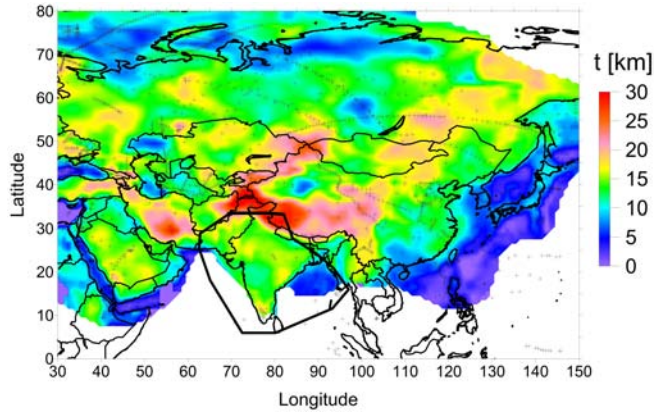


(c) lower

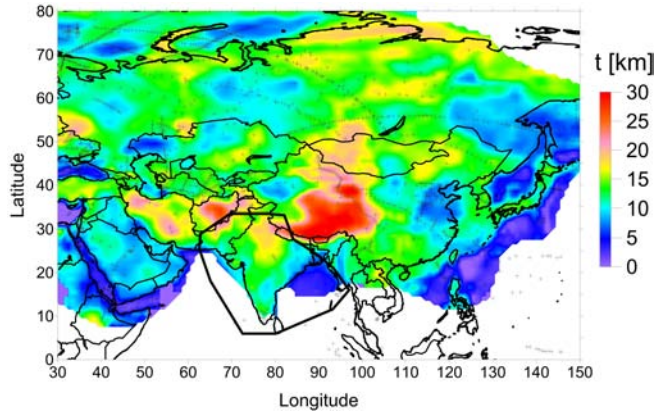
Figure 5.3: Pressure wave velocities in upper middle and lower crustal velocity layer (black line denotes boundary of the area on the Indian subcontinent where the modified approach was applied, see main text)



(d) upper



(e) middle



(f) lower

Figure 5.3: Thickness of upper, middle and lower crustal velocity layer (black line denotes boundary of the area on the Indian subcontinent where the modified approach was applied, see main text)

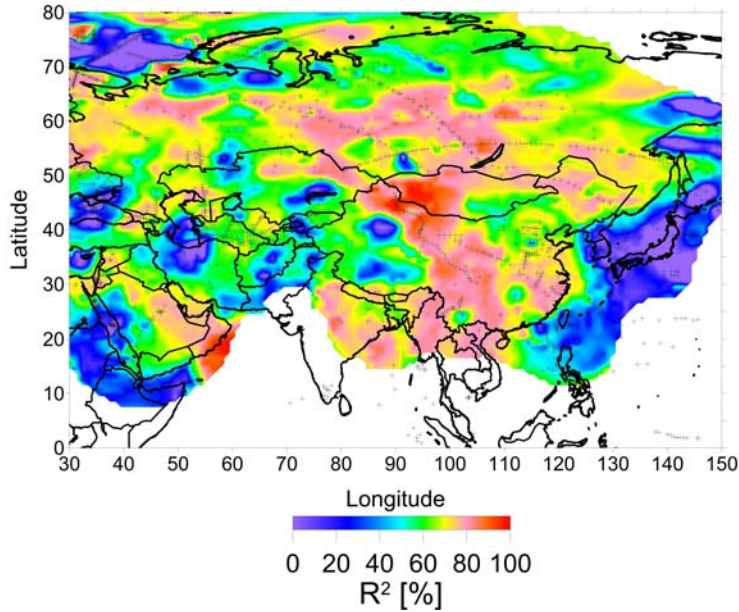


Figure 5.4: Coefficient of determination as measure of quality of the crustal model

Table 5.2: Values used for India (t = relative thickness; V = average velocity)

Type	t_{upper}^{rel}	t_{middle}^{rel}	t_{lower}^{rel}	V_{upper}	V_{middle}	V_{lower}
Shield	0.34	0.37	0.29	6.16	6.56	7.01
Platform	0.33	0.34	0.33	6.19	6.57	6.97
Orogen	0.31	0.36	0.33	6.11	6.51	6.96
Basin	0.30	0.38	.32	6.15	6.55	7.11
LIP	0.32	0.32	0.36	6.17	6.53	6.94

The average of the coefficient of determination (R^2) is 66.5%, but it varies substantially throughout the research area, see figure 5.4. Central China as well as the southern part of Russia are well resolved ($R^2 > 75\%$), whereas the areas around Japan and the Barentsz Sea remain poorly resolved ($R^2 < 20\%$). Closer analysis of the data in the Barentsz Sea area [Ritzmann and Faleide, 2007, Gac et al., 2012] reveals that there the crustal velocity distribution can not be easily approximated by the three layered function used in this model.

5.6 Statistical analysis

The new crustal model for Asia is analysed by classifying the region into six different geological province types, following Mooney [2007]: shields, platforms, orogens, basins, LIPs and regions of extended crust, similar to the analysis of the Moho in section 4.5. Areas with little or no primary data are excluded from

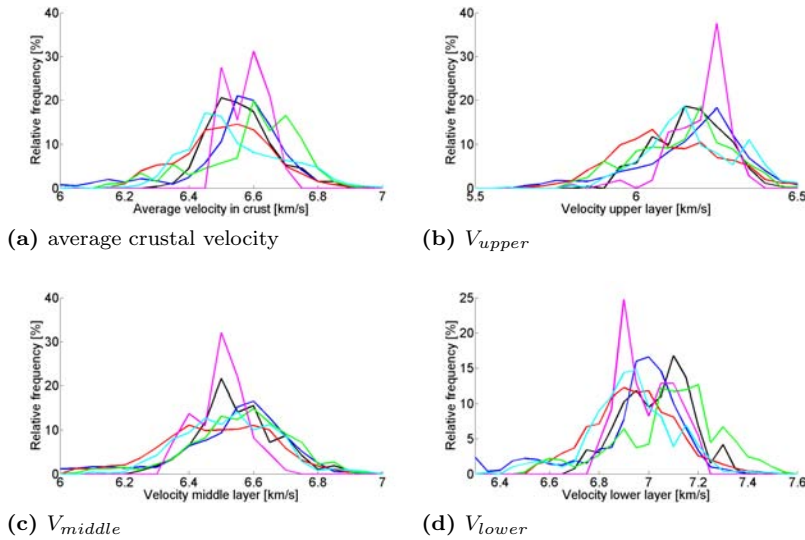


Figure 5.5: Histograms of the distribution of of different crustal parameters (black = shield, dark blue = platform, red = orogen, green = basin, purple = large igneous province, light blue = extended crust)

this analysis.

The peak in the average P-wave velocities (mode) occurs at the lowest velocity for extended crust (6.45km/s) (figure 5.5a). These low velocities are found in East China and coincide with a thin lower crust in this area (figure 5.3f). Higher average P-wave velocities in extensional settings are found around Lake Baikal and in northern Russia. The mean of the average P-wave velocities in orogens is lower than any other crust type. This is due to the low velocities in the Tibetan region (figure 5.2) particularly in the upper crust (figure 5.3a) (for more detailed studies of this area see e.g. Li et al. [2006], Liu et al. [2006], Zhang and Klemperer [2010], Zhang et al. [2011]). The second peak in the average velocities for basins is caused by high ($> 6.7\text{km/s}$) average velocities in the Pre-Caspian Basin in western Kazakhstan [Brunet et al., 1999, 2003, Guest et al., 2007, Egan et al., 2009].

When analysing velocities per intracrustal layer, a double peak turns up in the velocities in the upper crust for extensional settings, figure 5.5b. The second peak is due to high velocities in northern Russia and west Kazakhstan (between the Caspian Sea and Aral Sea). The wide spread (absence of a clear peak) in P-wave velocities in orogenic regions is noticeable in figures 5.5b and 5.5c. Figure 5.5d shows high velocities in the lower crust for the Northern Caucasus foreland basin —(in accordance with Ershov et al. [2003]) and the Mesopotamian foredeep basin (e.g papers in Al Hosani et al. [2013], see also figure 5.3c).

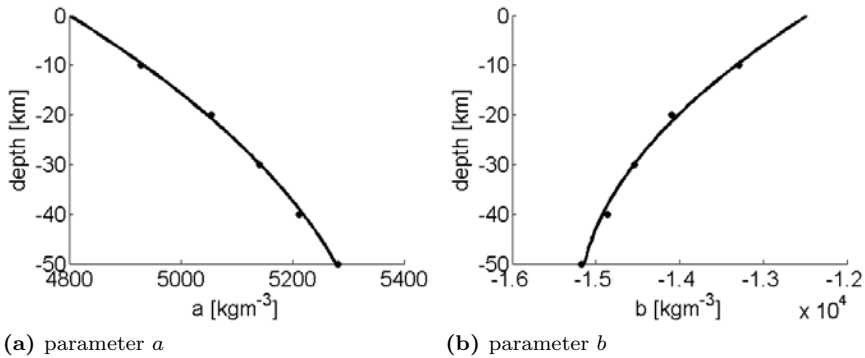


Figure 5.6: Estimating parameters a and b as a function of depth, based on Christensen and Mooney [1995] (black dots correspond to values in table 5.3)

5.7 Conversion to density

Analogous to the conversion of p-wave velocities to densities in sediments (section 3.1), the p-wave velocities in the crust can also be converted to densities. According to Christensen and Mooney [1995] density (ρ) can be obtained from the pressure wave velocity (V_p) using equation 5.3.

$$\rho = \frac{(a + \frac{b}{V})}{1000} \quad (5.3)$$

Parameters a and b are depth dependent and are given by Christensen and Mooney [1995] for some depth intervals (table 5.3). Second degree polynomials have been fitted through the depth- a and depth- b pairs (figure 5.6), leading to best fit equations 5.4a and 5.4b for a and b , respectively.

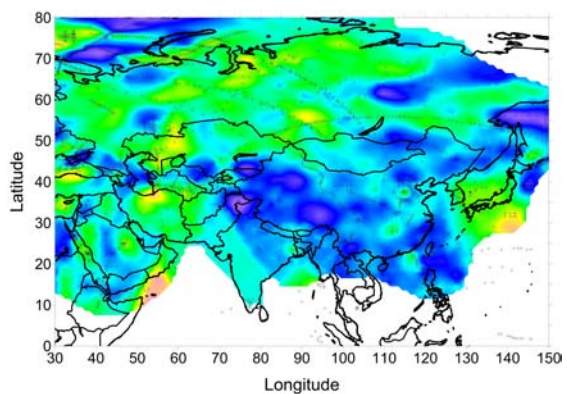
Table 5.3: Non-linear Velocity-Density Regression Line Parameters (from Christensen and Mooney [1995])

Depth	a [kgm^{-3}]	b [kgm^{-3}/kms^{-s}]
10	4929	-13294
20	5055	-14094
30	5141	-14539
40	5212	-14863
50	5281	-15174

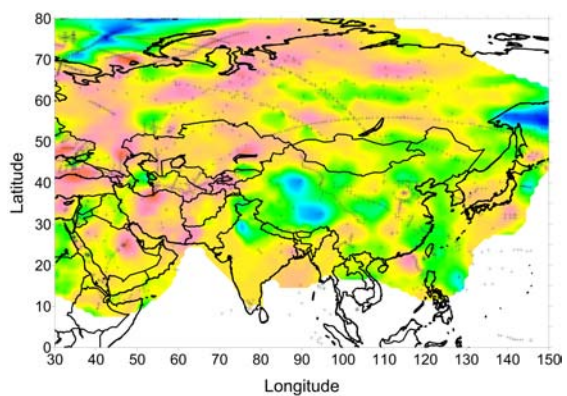
$$a = 4800.8 + 14.13857143z - 0.09214285714z^2 \quad (5.4a)$$

$$b = -12484.6 - 92.39z + 0.785z^2 \quad (5.4b)$$

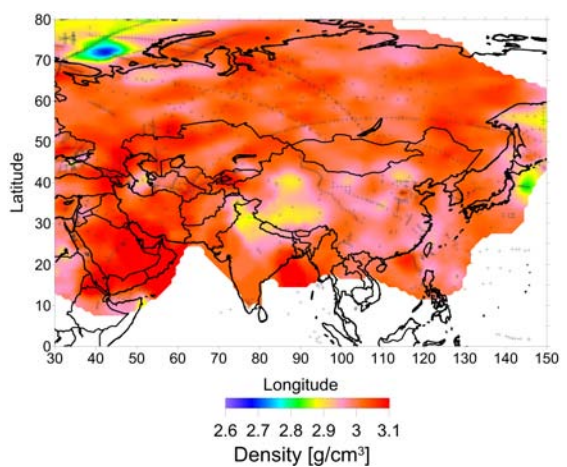
Converting the P-wave velocities (figure 5.3) in the upper, middle and lower crust results in the average density distributions shown in figure 5.7.



(a) density upper crust



(b) density middle crust



(c) density lower crust

Figure 5.7: Average crustal density in the three crustal velocity layers)



本島 聯合

野野中國鮮谷新

Thermal, density and compositional model of the lithospheric mantle

Separating the effects thermal and compositional heterogeneities in the lithospheric mantle have on observable data is complex and this problem is not well resolved. While seismic studies indicate that heterogeneities exist in the mantle lithosphere, seismic data alone are insufficient to attribute the observed wave velocity anomalies to thermal differences, since variations in composition may also have a significant effect. Analysing solely gravity anomalies one cannot distinguish between e.g. stacked density anomalies or lateral density anomalies. Combining both datasets can better resolve the anomalous structure and provide more insight into the mantle lithosphere, though the solution to the problem at hand remains non-unique.

This chapter will treat a combined seismics-gravity approach to the thermal-composition problem of the mantle lithosphere (figure 6.1). The method is iterative. After the assumption of an initial composition, the thermal state of the mantle is modelled based on tomographic data (section 6.1). The resulting thermal and density models are forward modelled into a gravity signal (section 6.2). This gravity signal is compared with the mantle gravity field obtained after removing of the crustal effect from the observed signal. Based on the differences between the modelled and observed gravity signal (section 6.3), together with information from literature on e.g. xenoliths, the composition is adjusted (section 6.4). After a few iterations, the system stabilizes and the final solution is reached (section 6.5).

6.1 Temperature and density modelling

Seismic body wave propagation velocities are a function of three material properties, bulk modulus (κ), shear modulus (μ) and density (ρ), see equation 6.1. These so called anharmonic velocities (V_{anh}) apply only to perfectly elastic isotropic media. However, the minerals in the lithospheric mantle are not perfectly elastic and therefore an anelasticity correction c_{anel} has to be applied to

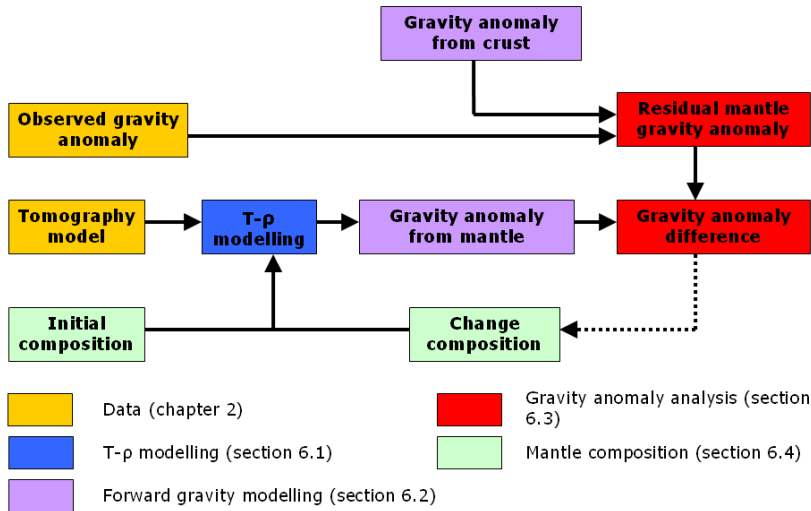


Figure 6.1: Workflow for the combined seismics-gravity approach to the thermal-composition problem

the anharmonic velocities to obtain synthetic velocities V_{syn} that can be compared to observed velocities V_{obs} [Jackson et al., 1992, Karato, 1993], see equation 6.2 and section 6.1.3.

$$V_{anh,p} = \sqrt{\frac{\kappa + \frac{4}{3}\mu}{\rho}} \quad (6.1a)$$

$$V_{anh,s} = \sqrt{\frac{\mu}{\rho}} \quad (6.1b)$$

$$V_{syn} = c_{anel} V_{anh} \quad (6.2)$$

This leads to three unknowns with at most two knowns. In some regions only the shear (V_s) or the pressure wave velocity (V_p) is well determined and not both. In any case, the system is not directly solvable in terms of κ , μ and ρ . However, the three unknowns can be related to three parameters, namely the pressure P , the temperature, T , and the composition, X , using geochemical relationships (see e.g. Duffy and Anderson [1989] or Vacher et al. [1998] for an overview). Pressure is fairly well constrained by depth [Dziewonski and Anderson, 1981], but assigning velocity heterogeneity to thermal and/or compositional effects remains challenging (e.g. Artemieva [2009], Afonso et al. [2008]). Two approaches can be discerned, compositional modelling and thermal modelling. In compositional modelling, a temperature distribution, constrained by independent data such as surface heat flow, is assumed and relations are solved for composition (e.g. Artemieva [2009]). In the thermal approach, a composition is assumed, based

on for instance xenolith studies, and temperature is solved for (e.g. Goes et al. [2000], Cammarano et al. [2003], Tesauro [2009]).

The main disadvantage of the thermal method is the assumption of a composition that may be poorly constrained, especially in continental settings. Chemical heterogeneity plays a major role in the continental lithosphere [Artemieva, 2009, Afonso et al., 2008]. In contrast, its effect on seismic velocities and densities is remarkably different, which makes it possible to discriminate between these effects using a combined interpretation of the gravity and seismic data, e.g. Kaban et al. [2003]. A major concern in this approach is the effect of volatiles, which might significantly affect seismic velocities.

Another method to recover temperature distribution in the lithosphere, based on independent data such as heat flow measurements, e.g. Artemieva and Mooney [2001]. However, this method also requires assumptions with regard to heat production in crustal rocks and variations in thermal conductivity with depth [Chapman, 1986]. Furthermore, shallow and local processes may heavily influence the measured surface heat flow [Goes et al., 2000]. This study follows the thermal approach and uses gravity field analysis as well as xenolith studies to further constrain the composition of the lithospheric mantle, e.g. Kaban et al. [2003, 2010].

A work flow for the thermal modelling can be seen in figure 6.2. The thermal approach starts with converting mineral properties at surface conditions κ_0 , μ_0 and ρ_0 to mineral properties at increased depth and elevated temperature conditions, κ , μ and ρ , using their dependencies on pressure and temperature (section 6.1.1). Secondly, κ , μ and ρ for the mantle composition are obtained by averaging the properties of the separate minerals in the composition, using Voigt-Reuss-Hill (VRH) averaging (section 6.1.2). These composition properties can be converted to anharmonic velocities, using relations 6.1. The anelastic correction factor, which is also dependent on T and P (section 6.1.3) is used to arrive at the synthetic velocities (V_{syn}).

The method can be used iteratively [Goes et al., 2000]. In this case, an initial temperature is chosen, the corresponding V_{syn} is computed. Based on the difference between the V_{syn} and the V_{obs} , and the temperature dependence of V_{syn} ($\frac{\partial V_{syn}}{\partial T}$), the temperature is updated and the loop repeated. Iteration is terminated after convergence, usually only a few iterations are required.

In an alternative approach a range of temperatures can be selected, and corresponding velocities computed, resulting in a velocity temperature curve. Velocities can then be converted to temperatures based on this curve. Main advantages of this approach are that the derivatives with respect to temperature need not be calculated. Furthermore, when the composition stays the same, the same curve can be used for multiple velocity observations. In general, computation time is drastically reduced using the curve-approach rather than the iterative-approach, though the advantage reduces when composition changes from one location to the next.

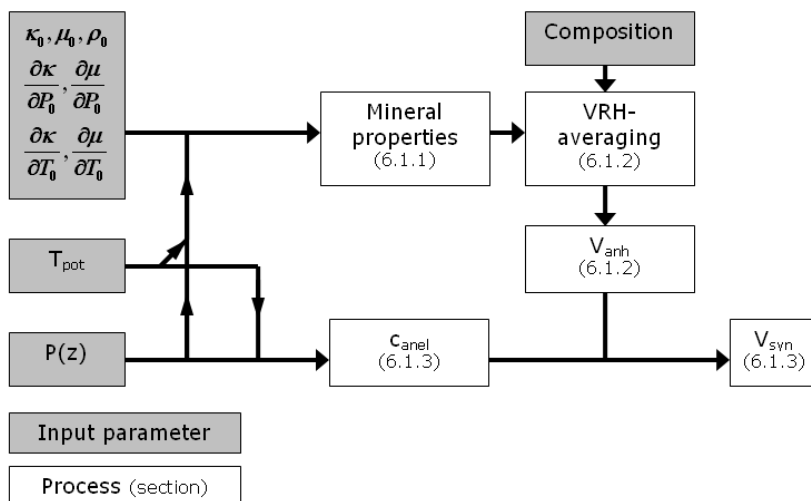


Figure 6.2: Workflow in the thermal method

6.1.1 Mineral properties

In the thermal approach, mineral properties at surface conditions (T_0 , P_0) are assumed to be known. Values used in this study for ρ_0 , κ_0 and μ_0 as well as their derivatives with respect to both pressure and temperature are given in table 6.1. These properties are extrapolated to elevated temperatures and then, along the adiabat, to increased pressures [Cammarano et al., 2003].

Furthermore, the thermal expansion coefficient α is assumed to be a known function of T and integrable to the adiabat (i.e. from T_0 to the potential temperature T_{pot}). An empirical relation of α as a function of T is given in equation 6.3 [Fei, 1995]. The three parameters a_0 , a_1 and a_2 are given for different minerals in table 6.2.

$$\alpha(T) = a_0 + a_1T + a_2T^{-2} \quad (6.3)$$

The density (ρ) and elastic moduli (κ and μ) are extrapolated to the potential temperature (T_{pot}) of the adiabat (equations 6.4 and 6.5). Also the pressure derivatives of the elastic moduli are extrapolated (equation 6.6).

$$\rho(T_{pot}, P_0) = \rho_0 \exp \left[- \int_{T_0}^{T_{pot}} \alpha(T) dT \right] \quad (6.4)$$

$$\kappa(T_{pot}, P_0) = \kappa_0 + \left(\frac{\partial \kappa}{\partial T} \right)_P (T_{pot} - T_0) \quad (6.5a)$$

$$\mu(T_{pot}, P_0) = \mu_0 + \left(\frac{\partial \mu}{\partial T} \right)_P (T_{pot} - T_0) \quad (6.5b)$$

Table 6.1: Density and elastic properties of minerals at surface conditions (T_0, P_0) [Cammarano et al., 2003]

Mineral	ρ_0 (gcm^{-3})	κ_0 (GPa)	μ_0 (GPa)	$\frac{\partial \kappa}{\partial P_0}$ (-)	$\frac{\partial \mu}{\partial P_0}$ (-)	$\frac{\partial \kappa}{\partial T_0}$ (GPa/K)	$\frac{\partial \mu}{\partial T_0}$ (GPa/K)
Olivine (Ol)	3.222 + 1.182 X_{Fe}	129 ($\pm 1\%$)	81-31 X_{Fe} ($\pm 1\%$)	4.2 ($\pm 3\%$)	1.4 ($\pm 7\%$)	-0.017 ($\pm 17\%$)	-0.014 ($\pm 17\%$)
Orthopyroxene (OPX)	3.215 + 0.799 X_{Fe}	109 + 20 X_{Fe} ($\pm 2\%$)	75+10 X_{Fe} ($\pm 2\%$)	7.0 ($\pm 10\%$)	1.6 ($\pm 15\%$)	-0.027 ($\pm 25\%$)	-0.012 ($\pm 25\%$)
Clinopyroxene (CPX)	3.277 + 0.38 X_{Fe}	105 + 12 X_{Fe} ($\pm 1\%$)	67-6 X_{Fe} ($\pm 2\%$)	6.2-1.9 X_{Fe} ($\pm 10\%$)	1.7 ($\pm 15\%$)	-0.013 ($\pm 25\%$)	-0.010 ($\pm 25\%$)
Garnet (Gt)	3.597	168 ($\pm 1\%$)	107 ($\pm 2\%$)	5.2 ($\pm 10\%$)	1.6 ($\pm 15\%$)	-0.016 ($\pm 20\%$)	-0.012 ($\pm 25\%$)

CHAPTER 6. THERMAL, DENSITY AND COMPOSITIONAL MODEL
OF THE LITHOSPHERIC MANTLE

Table 6.2: Thermal expansion parameters a_0 , a_1 and a_2 for different minerals [Fei, 1995]

Mineral	T range [K]	a_0 (10^{-4})	a_1 (10^{-8})	a_2
Olivine				
Fayalite (Fe_2SiO_4)	298-1123	0.2386	1.153	-0.0518
Forsterite (Mg_2SiO_4)	300-1300	0.2854	1.0080	-0.3842
OPX				
Enstatite ($MgSiO_3$)	293-1073	0.2947	0.2694	-0.5588
Orthoferrosilite ($FeSiO_3$)	297-1253	0.3930	0.0000	0.0000
CPX				
Diopside ($CaMgSi_2SO_6$)	297-1273	0.3330	0.0000	0.0000
Hedenbergite ($CaFeSi_2O_6$)	297-1273	0.2980	0.0000	0.000
Garnet				
Almandite ($Fe_3Al_2Si_3O_{12}$)	294-1044	0.1776	1.2140	-0.5071
Grossularite ($Ca_3Al_2Si_3O_{12}$)	292-980	0.1951	0.8089	-0.4972
Pyrope ($Mg_3Al_3Si_3O_{12}$)	283-1031	0.2311	0.5956	-0.4538

$$\frac{\partial \kappa}{\partial P}(T) = \frac{\partial \kappa}{\partial P_0} \exp \left[\int_{T_0}^{T_{pot}} \alpha(T) dT \right] \quad (6.6a)$$

$$\frac{\partial \mu}{\partial P}(T) = \frac{\partial \mu}{\partial P_0} \exp \left[\int_{T_0}^{T_{pot}} \alpha(T) dT \right] \quad (6.6b)$$

Thus the density (ρ), wave moduli M_w and derivatives are known at specific temperatures, but at surface pressure (P_0) only. The density can be extrapolated along the adiabat using 6.7.

$$\rho(P, T) = \rho(T_{pot}, P_0) (1 - 2\epsilon)^{3/2} \quad (6.7)$$

The strain (ϵ) in equation 6.7 can be obtained by adopting the finite strain formulation [Duffy and Anderson, 1989, Davies and Dziewonsky, 1975], equation 6.8.

$$P = -(1 - 2\epsilon)^{5/2} \left(C_1\epsilon + \frac{1}{2}C_2\epsilon^2 + \frac{1}{6}C_3\epsilon^3 + \dots \right) \quad (6.8)$$

Parameters C_1 , C_2 in equation 6.8 depend on the bulk modulus and its derivative with respect to pressure (equations 6.9a and 6.9b). For $\epsilon \ll 1$ the pressure-strain equation (6.8) can be truncated after the second order, by setting

$C_3 = 0$ (equation 6.9c).

$$C_1 = 3\kappa(T_{pot}, P_0) \quad (6.9a)$$

$$C_2 = 9\kappa(T_{pot}, P_0) \left(4 - \frac{\partial\kappa}{\partial P_0}(T) \right) \quad (6.9b)$$

$$C_3 = 27\kappa(T_{pot}, P_0) \left[\kappa(T_{pot}, P_0) \frac{\partial^2\kappa}{\partial P_0^2}(T) - \frac{\partial\kappa}{\partial P_0}(T) \left(7 - \frac{\partial\kappa}{\partial P_0}(T) \right) + \frac{143}{9} \right] \quad (6.9c)$$

However equation 6.8 is not directly invertible, thus an iterative scheme needs to be adopted. Since the equation is differentiable with respect to ϵ , Newton's method (also known as the Newton-Raphson method) [Wallis, 1685, Raphson, 1690] can be applied.

Using the same finite strain approach, also the wave moduli (M_w) can be extrapolated for pressure (equation 6.10)¹.

$$M_w(P, T) = (1 - 2\epsilon)^{5/2} \left(A_1 + A_2\epsilon + \frac{1}{2}A_3\epsilon^2 \right) \quad (6.10)$$

The parameters A_1 , A_2 and A_3 from equation 6.10 are given in equations 6.11

$$A_1 = M_{w0} \quad (6.11a)$$

$$A_2 = 5A_1 - 3\kappa(T_{pot}, P_0) \frac{\partial M_w}{\partial P_0}(T) \quad (6.11b)$$

$$A_3 = 9\kappa^2(T_{pot}, P_0) \frac{\partial^2 M_w}{\partial P_0^2}(T) - 3A_2 \left(\frac{\partial\kappa}{\partial P_0}(T) - 4 \right) + 5A_1 \left(3 \frac{\partial\kappa}{\partial P_0}(T) - 5 \right) \quad (6.11c)$$

in which $M_{w0} = \mu_0$, $\frac{\partial M_w}{\partial P_0}(T) = \frac{\partial\mu}{\partial P_0}(T)$ and $\frac{\partial^2 M_w}{\partial P_0^2}(T) = \frac{\partial^2\mu}{\partial P_0^2}(T)$ for shear waves and $M_{w0} = \kappa_0 + \frac{4}{3}\mu_0$, $\frac{\partial M_w}{\partial P_0}(T) = \frac{\partial\kappa}{\partial P_0}(T) + 4/3 \frac{\partial\mu}{\partial P_0}(T)$ and $\frac{\partial^2 M_w}{\partial P_0^2}(T) = \frac{\partial^2\kappa}{\partial P_0^2}(T) + 4/3 \frac{\partial^2\mu}{\partial P_0^2}(T)$ for pressure waves. A value for $\frac{\partial^2\kappa}{\partial P_0^2}(T)$ is obtained by equating $C_3 = 0^2$ and $\frac{\partial^2\mu}{\partial P_0^2}(T) = 0.631 \frac{\partial^2\kappa}{\partial P_0^2}(T)$ [Cammarano et al., 2003, Stacey, 1992].

¹Cammarano et al. [2003] split equation 6.10 into separate equations for pressure and shear waves. Please note that in Cammarano et al. [2003] the factor $\frac{1}{2}$ is missing in front of parameters A_3 in the case of shear waves (M_3 in Cammarano et al. [2003])

²In Cammarano et al. [2003] the reasoning behind equating $C_3 = 0$ is that relation 6.8 is truncated after degree 2. This truncation is valid because ϵ^3 becomes very small in comparison to the previous terms, and not because C_3 is very small. Since C_1 and C_2 are of the same order, it is more likely that C_3 is also, rather than that $C_3 = 0$. Therefore the use of $C_3 = 0$ is questionable. However the terms A_1 , A_2 and A_3 are of the same order (10^{12}). In equation 6.10 A_1 is multiplied with 1, A_2 with ϵ , which is of the order 10^{-2} and A_3 is multiplied with ϵ^2 , which is of the order 10^{-4} . Thus any adverse effects of setting $C_3 = 0$ become negligible. This study, therefore, still follows the assumption of $C_3 = 0$ made in Cammarano et al. [2003].

6.1.2 Voigt-Reuss-Hill averaging

Hill [1952] proved that stress and strain of composite polycrystals lie between two extremes, namely the Reuss [Reuss, 1929] and Voigt [Voigt, 1928] values. Furthermore, Hill [1952] suggested, based on empirical data that $\frac{1}{2} (G^{reuss} + G^{voigt})$ or $\sqrt{G^{reuss}G^{voigt}}$ are good candidates for averaging e.g. shear and bulk moduli of polycrystal minerals. This was further confirmed by Chung [1963], who introduced $\frac{1}{2} (G^{reuss} + G^{voigt})$ as the standard average and also coined the expression VRH averaging. The concept of VRH averaging is used to compute strength parameters (e.g. κ or μ) of a composite mineral, based on the strength parameters of its constituents.

The Voigt average [Voigt, 1928] of a strength parameter (G^{voigt}) is a weighted average, with the weights determined by the volume fractions (λ_{vol}) of the n constituent minerals (equation 6.12a). The Reuss average [Reuss, 1929] of a strength parameter (G^{reuss}) is given in equation 6.12b. The strength parameters of the composition are then computed as in equation 6.13.

$$G^{voigt} = \sum_{i=1}^n \lambda_{vol,i} G_i \quad (6.12a)$$

$$G^{Reuss} = \left(\sum_{i=1}^n \frac{\lambda_{vol,i}}{G_i} \right)^{-1} \quad (6.12b)$$

$$G^{vrh} = \frac{1}{2} G^{voigt} + \frac{1}{2} G^{reuss} \quad (6.13)$$

The average density (equation 6.14) of the composition is calculated using only the Voigt average, since the average density is a dependent on the volume fractions of the constituents only.

$$\bar{\rho} = \sum_{i=1}^n \lambda_{vol,i} \rho_i \quad (6.14)$$

The average strength parameters and density can be used to compute the anharmonic velocities, as shown in equation 6.1.

6.1.3 Anelasticity correction

Because of energy dissipation due to viscous deformation, an anelastic correction needs to be taken into account when computing the wave velocities. The computation of the anelastic correction factor is less elaborate than the computation of the anharmonic velocity. Central to the computation of the anelastic correction (c_{anel}) (equation 6.15) is the wave attenuation factor Q .

$$c_{anel} = \left[1 - \frac{Q^{-1}(\omega, T)}{2 \tan(\pi a/2)} \right] \quad (6.15)$$

The wave attenuation factor (Q) is different for shear and pressure waves. In case of a shear wave the wave attenuation factor (Q) equals the rigidity attenuation factor (Q_μ).

Table 6.3: Anelasticity parameters [Cammarano et al., 2003]

Homologous temperature model	Norm. factor, A	Homologous temp. scaling, g_{temp}	Freq. dep. atten. a	Seismic freq. ω (Hz)	Bulk attenuation Q_κ
Q1	0.5	20	0.2	1	1000
Q2	0.8	20	0.2	1	1000
Q3	1.1	20	0.2	1	1000
Q4	0.035	30	0.2	1	1000
Q5	0.056	30	0.2	1	1000
Q6	0.077	30	0.2	1	1000

$$Q_\mu = A\omega^a \exp\left(\frac{ag_{temp}T_m}{T}\right) \quad (6.16)$$

Different models exist [Cammarano et al., 2003], using different values for the normalization factor A , seismic frequency ω , the frequency dependent attenuation a and the homologous temperature scaling g_{temp} , see table 6.3.

In order to compute the shear wave attenuation factor Q_μ , first the melting temperature T_{melt} must be computed (equation 6.17), with $a_{melt} = -5.104 \cdot 10^{-18} K/Pa^2$, $b_{melt} = 132.899 \cdot 10^{-9} K/Pa$ and $c_{melt} = 1120.661 K$ [Hirschmann, 2000].

$$T_m = a_{melt}P^2 + b_{melt}P + c_{melt} \quad (6.17)$$

Using T_{melt} , the rigidity attenuation factor Q_μ can be determined (equation 6.16).

In case of a pressure wave Q is defined as equation 6.18.

$$Q^{-1} = \begin{cases} Q_\mu^{-1} & \text{for shear waves} \\ (L-1)Q_\kappa^{-1} + LQ_\mu^{-1} & \text{for pressure wave} \end{cases} \quad (6.18)$$

The bulk attenuation factor Q_κ can be found in table 6.3. The parameter L is given by equation 6.19 where the $\bar{\kappa}$ and $\bar{\mu}$ denote the average κ and μ of the composite mineral rather than the κ and μ of any of its constituents.

$$L = \frac{4}{3} \left(\frac{V_s}{V_p} \right)^2 = \frac{4}{3} \frac{\bar{\mu}}{\bar{\kappa} + \frac{4}{3}\bar{\mu}} \quad (6.19)$$

The final anelastic correction factor can then be computed as in equation 6.15. Subsequently the synthetic wave velocity corrected for viscous effects is computed using equation 6.20.

$$V_{syn} = c_{anel}V_{anh} \quad (6.20)$$

These synthetic velocities can be compared to the observed velocities (V_{obs}) and finally a corresponding temperature (T) and density (ρ) can be derived.

6.2 Forward gravity field modelling

This section deals with forward gravity field modelling. In order to understand this, firstly some general principles of gravity potential are discussed (section 6.2.1). An elaborate discussion of theories and applications of gravity potential can be found in e.g. Blakely [1995]. Secondly, the specifics of the forward gravity modelling performed in this study are discussed (section 6.2.2). Forward gravity has been done by making use of programs by Mikhail Kaban (e.g. Kaban [2001], Kaban and Mooney [2001], Kaban et al. [2010]).

6.2.1 Theory of gravity field modelling

Gravitational potential obeys the principle of superposition. The gravitational potential of a collection of masses is the sum of the gravitational attractions of the individual masses.

$$U(P) = G \int_V \frac{dm}{r} \quad (6.21)$$

where G is the gravitational constant, v is a volume containing all the mass and r the distance between the observation point and the infinitely small mass dm . Since $dm = \rho dv$, in which ρ is the density at the location of dm , equation 6.21 can be written as 6.22.

$$U(P) = G \int_V \frac{\rho}{r} dv \quad (6.22)$$

The gravitational acceleration (g) of the potential U is obtained through equation 6.23.

$$\begin{aligned} \mathbf{g}(P) &= \nabla U \\ &= -G \int_V \rho \frac{\mathbf{r}}{r^3} dv \end{aligned} \quad (6.23)$$

Considering only the z -direction reduces equation 6.23 to 6.24, where r is the linear distance from the observation point (P) to the mass, given by equation 6.25.

$$\begin{aligned} g(x, y, z) &= \frac{\partial U}{\partial z} \\ &= -G \int_{z'} \int_{y'} \int_{x'} \rho(x', y', z') \frac{z-z'}{r^3} dx' dy' dz' \end{aligned} \quad (6.24)$$

$$r = \sqrt{(x-x')^2 + (y-y')^2 + (z-z')^2} \quad (6.25)$$

Equation 6.24 can be generalized and split in two parts, with the first part only depending on density (ρ) and the second part solely on position and shape of the mass (ψ), equation 6.26.

$$g(x, y, z) = G \int_{z'} \int_{y'} \int_{x'} \rho(x', y', z') \psi(x-x', y-y', z-z') dx' dy' dz' \quad (6.26)$$

The general form of the function ψ is given in equation 6.27 and can be considered a Green's function for a gravitational attraction at (x, y, z) of a point mass located at (x', y', z') [Blakely, 1995].

$$\psi(x, y, z) = -\frac{z}{(x^2 + y^2 + z^2)^{\frac{3}{2}}} \quad (6.27)$$

Considering a small volume (V_n) and assuming the density to be constant within this small volume, the dependency on ρ_n can be taken out of the volume integral. The gravitational attraction of V_n on point m (g_{mn}) can then be computed by equation 6.28.

$$g_{mn} = \rho_n \int_{z'} \int_{y'} \int_{x'} \psi(x_m - x', y_m - y', z_m - z') dx' dy' dz' = \rho_n \int_{V_n} \psi_{mn} dv \quad (6.28)$$

Many small volumes of constant density can be added together, using the superposition principle, to obtain the total gravitational attraction in z -direction at point m (g_m), equation 6.29.

$$g_m = \sum_{n=1}^N \rho_n \int_{V_n} \psi_{mn} dv \quad (6.29)$$

However, the Green's function (ψ) still needs to be integrated over V_n .

6.2.2 Evaluation of the Green's function for earth

In evaluating the Green's function for a realistic earth, certain simplifications need to be made, and side effects need to be taken into account. These simplifications (e.g. spherical earth, planar and cylindrical approaches) and some side effects (e.g. 'lateral effect' of the gravity signal) are discussed below.

Mass anomalies do not only influence the gravity field directly above, but also the gravity field in the surrounding area. The size of the influenced area depends, among other things, on the size, depth and the extent of the anomaly. However, the relation between an anomaly and its effect on the gravity field are not straight forward. Previously, geophysicists included a border area of 5° around the modelled area to account for this 'lateral effect' of the gravity signal [Kaban, 2008]. Nowadays, however, with the readily available global models for the main fields (e.g. global crustal and tomography and gravity models [Ritsema et al., 2011, Bassin et al., 2000, Förste et al., 2011]) and increased computing power, it is more convenient just to evaluate for the whole globe. Even though the resolution outside the study area may be lower, this poses no significant problems for the effect of distant zones [Kaban, 2008].

The gravity effect at each location on the surface of the earth can be computed as a sum of the effects of spherical prisms (tesseroids, figure 6.3), volume elements limited by the used grids and depth division. Evaluation of the gravity effect of tesseroids is complicated and needs enormous computing time (e.g.

Strakhov et al. [1989]). It is however possible to replace the tesseroïd by a different element that reproduces the gravity effect of the tesseroïd with sufficient accuracy (e.g. Artemjev and Kaban [1994]). Alternatively, each volume element can be subdivided into smaller parts to obtain the required level of accuracy. Regardless which of the two methods is chosen, the total mass of each volume element needs to be preserved, as well as the position of the centre of mass of the element.

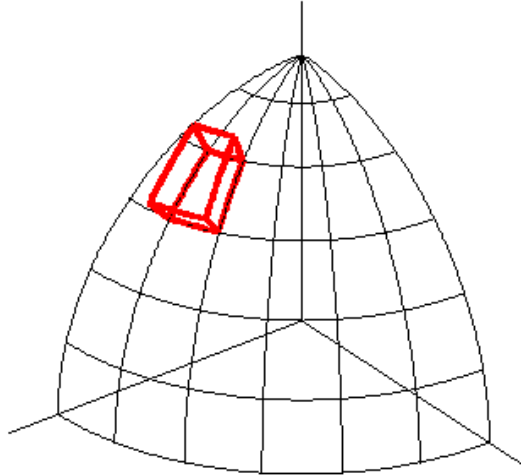


Figure 6.3: A tesseroïd

In the vicinity of the evaluation point (within 3°) a parallelepiped can replace the tesseroïd with sufficient accuracy as a basic shape for integration, figure 6.4a. Outside this zone the actual shape of the element is already less relevant, as long as the mass and centre of mass is preserved. Therefore, at distances larger than 3° the Green's function is evaluated for sectors of cylinders, which can be computed quickly and still are more accurate than using a simple point mass (spherical volume). The induced error due to the simplifications in this scheme remains within $1mGal$ [Artemjev et al., 1994].

Parallelepiped For a parallelepiped, coordinates need to be transformed such that observation point m coincides with the origin of the coordinate system. The parallelepiped is then defined by its two diagonally opposite corners at (x_1, y_1, z_1) and (x_2, y_2, z_2) . The integral of equation 6.29 can then be replaced by the summation given in equation 6.30 [Plouff, 1976]. In this equation, R_{ijk} is the distance from the origin to the corner point (x_i, y_j, z_k) of the parallelepiped (equation 6.31a) and ξ is defined in equation 6.31b.

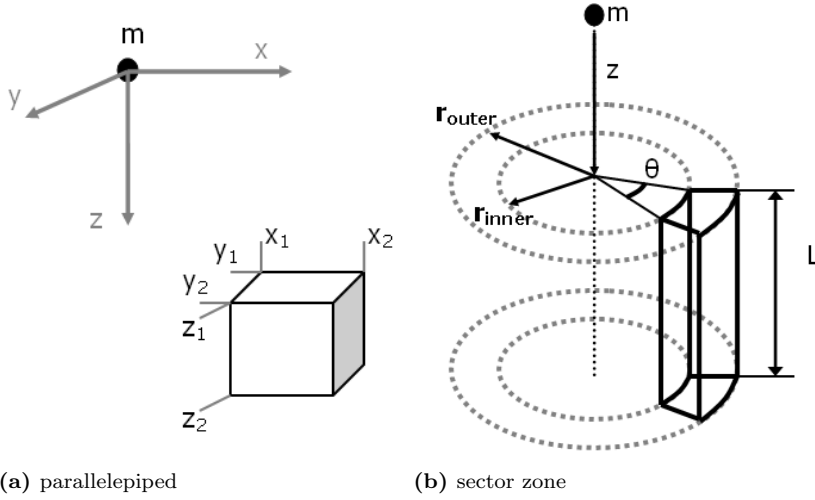


Figure 6.4: Two shapes for which the Green's function can be evaluated exactly.

$$\int_{V_n} \psi_{mn} dv = \sum_{i=1}^2 \sum_{j=1}^2 \sum_{k=1}^2 \xi_{ijk} \left(z_k \arctan \frac{x_i y_j}{z_k R_{ijk}} - x_i \log(R_{ijk} + y_j) - y_j \log(R_{ijk} + x_i) \right) \quad (6.30)$$

$$R_{ijk} = \sqrt{x_i^2 + y_j^2 + z_k^2} \quad (6.31a)$$

$$\xi_{ijk} = (-1)^{i+j+k} \quad (6.31b)$$

Sector zone Similarly, there exists an expression for the integral in equation 6.29 when the volume V_n is a cylinder of radius R and height L . If observation point m is assumed to be on the vertical axis of the cylinder at a distance z above the top of this cylinder, the integral is given by equation 6.32, [Telford et al., 1981].

$$\int_{V_n} \psi_{mn} dv = 2\pi \left(L + \sqrt{z^2 + R^2} - \sqrt{(z+L)^2 + R^2} \right) \quad (6.32)$$

The vertical gravitational acceleration of a sector of the cylinder is given by equation 6.33. The sector is defined by its angular size θ , its inner and outer radii (r_{inner} and r_{outer}) and its height L .

$$\int_{V_n} \psi_{mn} dv = \theta \left(\sqrt{r_{inner}^2 + (z + L)^2} - \sqrt{r_{outer}^2 + (z + L)^2} \right. \\ \left. + \sqrt{r_{outer}^2 + z^2} - \sqrt{r_{inner}^2 + z^2} \right) \quad (6.33)$$

In this study, only disturbances of a spherically symmetric gravity field are concerned. Thus, only density anomalies are taken into account, not the average density itself. Mathematically, this means that equation 6.29 is not summed over densities ρ_n , but rather density anomalies $\Delta\rho_n$, which are given by subtracting from the density ρ_n the average density $\bar{\rho}$ at the same depth as ρ_n ($\Delta\rho_n = \rho_n - \bar{\rho}$).

6.3 Mantle gravity anomalies

The gravity effect of the crustal density model (constructed in sections 3.3 and 5.7) is evaluated relative to a horizontally homogeneous reference model [Kaban et al., 2012], using the techniques described in section 6.2.2. The purpose of this evaluation is to remove the effects of the crust from the observed the gravity signal and thus obtain the residual, or mantle gravity anomalies, reflecting density variations in the upper part of the mantle. This removal process can be compared to applying a Bouguer type correction extending from the surface to the Moho [Mooney and Kaban, 2010]. The evaluation is split into two parts. First the gravity effect of a laterally homogeneous crust, with varying thickness (as computed in chapter 4) is evaluated; this is the reference crustal model. For example, a deep Moho produces a negative gravity anomaly since crustal material is less dense than mantle material and the residual mantle anomaly will increase. Secondly, lateral variations in crustal density are introduced, as computed in sections 3.3 and 5.7. For example, low density sediments will produce a negative effect relative to standard crystalline crust, and by removing this effect, the residual mantle anomaly is increased.

In this study, the reference density model for the lithosphere of Kaban et al. [2003] and Mooney and Kaban [2010] was used. This reference model is balanced to the old (180 Ma) oceanic lithosphere according to the cooling plate model. It is shown in Kaban et al. [2003] that the density of the stable old oceanic lithosphere compares on average to the density of the lithosphere mantle under North America. In this study it is assumed that this comparison also holds for Asia. This model is equivalent to a continental model with no topography, a 15km thick upper crust with density 2.7g/cm³, a 25km thick lower crust with density 2.94g/cm³. Average density of the uppermost mantle is set equal to 3.35g/cm³. The calculated mantle residual anomalies are shown in figure 6.5. They are compared with the mantle effects estimated by forward gravity modelling (section 6.2) from temperature and compositional variations as described in section 6.4.

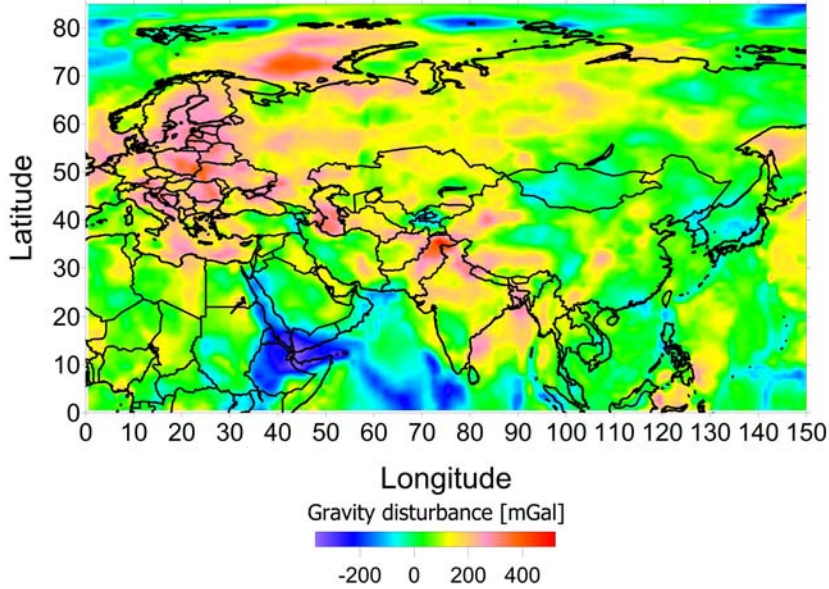


Figure 6.5: Residual gravity anomaly in the mantle after removal of crustal effects

6.4 Compositional changes

Assuming a general mantle composition of Primitive Mantle (see table 6.4 for its constituents), temperature and density can be computed throughout the study area, using the thermal modelling described in section 6.1. Note that since in the first iteration the same composition is used throughout the uppermost (up to 300km depth) mantle all velocity anomalies are interpreted as thermal anomalies and thus all density variations are purely thermal. The density distribution thus obtained can be forwarded into a gravity disturbance signal as described in section 6.2. This modelled gravity disturbance signal finally can be compared with the observed gravity disturbance. The modelled and observed gravity disturbance often will not coincide (figure 6.6), due to compositional variations in the lithosphere, which need to be accounted for in an integrative approach.

The difference between observed and modelled gravity disturbance is expressed as the effect of a density difference ($\Delta\rho$) spread over a 100km thick column (figure 6.6). A negative $\Delta\rho$ implies that the observed gravitational disturbance is lower than the gravitational disturbance derived from the model of the lithosphere (equation 6.34). In other words, areas with a negative $\Delta\rho$ in figure 6.6 require a less dense upper mantle and areas with a positive $\Delta\rho$ require a denser upper mantle.

$$\Delta m_0 = \frac{g_{obs} - g_{model}}{x} \quad (6.34)$$

The remainder of this chapter will focus on those areas with a negative

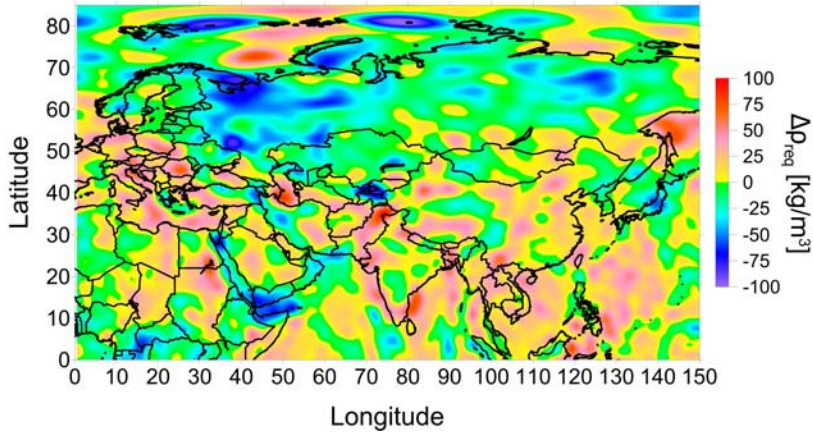


Figure 6.6: Difference between observed and modelled gravity anomaly, expressed as a density change ($\Delta\rho$) in a 100km thick column

$\Delta\rho$, which coincide with cratonic areas. In order to assess what compositional changes are required, the influence of a change in composition on density and temperature are required. This analysis is given in section 6.4.1. Next, the implementation of consecutive composition changes in the model is discussed in section 6.4.2.

6.4.1 Composition, density and temperature

Primitive Mantle is considered a common composition for mantle material. However, the lithospheric mantle underneath cratonic areas is often depleted, meaning relative high olivine contents and low garnet and clino-pyroxene (CPX) as well as low iron (Fe) content. Two such compositions are Garnet Lherzolite and Archon, where Garnet Lherzolite is slightly less depleted than Archon, table 6.4. Iron content can vary within each composition, effecting its elastic properties and the density of constituent minerals according to table 6.1.

Table 6.4: Different possible compositions of the upper mantle in order of increasing depletion. Constituents of olivine, clino-pyroxene (CPX), ortho-pyroxene (OPX) and garnet are given in volume percentages. (Primitive Mantle from McDonough [1990]; Garnet Lherzolite from Jordan [1979]; Archon from Griffin et al. [2003])

Composition	Olivine	CPX	OPX	Garnet
Primitive Mantle	58.5%	11.5%	15.0%	15.0%
Garnet Lherzolite	67.0%	4.5%	23.0%	5.5%
Archon	69.0%	2.0%	25.0%	4.0%

Temperature and density of these compositions can be computed as a function of velocity, using thermal modelling (section 6.1). Figure 6.7 shows the

velocity-density curve for these three compositions and several values for the iron content (Fe) for each composition. Increasing the relative amount of olivine decreases the overall density of the composition. Furthermore a decrease in iron content also leads to a decrease in density, at constant V_s . It is therefore possible to maintain the same velocity-density curve for various combinations of olivine and iron content. For instance primitive mantle with 11% iron has a similar velocity density curve as garnet lherzolite with iron content of 13% and archon with an iron content of 13.5%. Density decreases with roughly $0.13g/cm^3$ when the iron content is decreased by 1%, both for garnet lherzolite and for archon. The relation between temperature and composition is slightly more complex. Changing the composition from primitive mantle to garnet lherzolite, with the same iron content, leads to a decrease in temperature. When the iron content is lowered, the temperature increases. Archon shows a similar behavior.

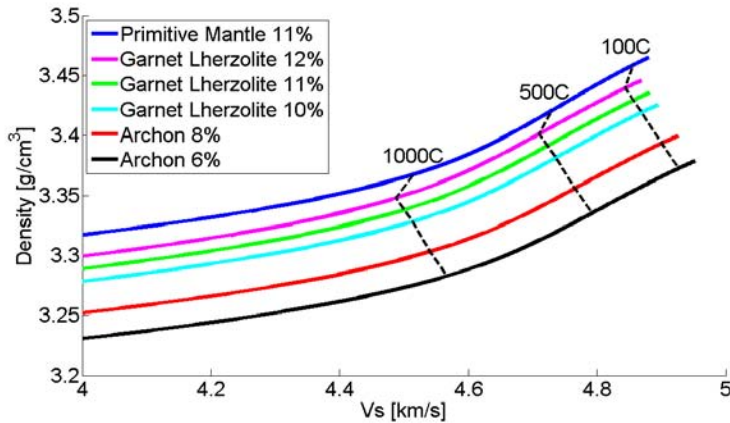


Figure 6.7: Effect of composition on density and temperature at given V_s and 100km depth (based on the relations described in section 6.1 [Goes et al., 2000, Cammarano et al., 2003])

6.4.2 Updating composition

In order to obtain a better fit between the modelled and observed gravity disturbances, the composition in the cratonic areas needs to be changed. Figure 6.6 is guiding in this process. Due 'lateral effects' described in section 6.2.2, adjusting the composition to obtain the required density change does not directly solve the discrepancy. However, iterating the process of updating composition, computing density using thermal modelling and consecutively computing the gravity disturbance and analysing the difference between the observed and modelled gravity disturbance (figure 6.1), leads to stable convergence.

The difference in gravity anomaly only provides a total mass difference in a vertical column of the earth, which can be related to figure 6.6 by equation 6.35, where the gravity anomaly was expressed as a required density change in

a $100km$ thick column of earth.

$$\Delta m_{req} = \Delta \rho_{grav} \times 100km \quad (6.35)$$

This mass difference can be spread over a vertical column of mantle material in infinitely many ways and a density change at each depth can also be achieved by infinitely many compositions. Therefore, formalized 'rules' need to be applied deciding how the mass change is to be distributed with depth and how the composition will be adjusted to accommodate the density changes in order to provide to robust solutions. These formalized 'rules' are given below and explained in more detail afterwards.

- Only adjust the composition above the lithosphere astenosphere boundary (LAB)
- Required mass change is spread evenly over the lithosphere
- Allow for only two possible compositional models, Garnet Lherzolite and Archon. Additional adjustments to density are made by varying the iron content of the composition

1. Provisional LAB If the mass change is accommodated entirely in the lithosphere, the density change integrated from the Moho (z_{Moho}) to the LAB (z_{LAB}), needs to equal the Δm_{req} , equation 6.36.

$$\Delta m_{req} = \int_{z_{Moho}}^{z_{LAB}} \rho(z), dz \quad (6.36)$$

Since the tomography model, and hence the derived mantle density model is available only for discrete depths (with increments of $50km$ for the tomography model used in this study), the integral of equation 6.36 can be discretised into the summation of equation 6.37, with $\Delta \rho_i$ the change in density in the i 'th layer and t_i the thickness of that layer, n_{LAB} (equation 6.38) is the deepest layer still residing in the lithosphere.

$$\Delta m_{req} = \sum_{i=1}^{i=n_{LAB}} \Delta \rho_i t_i \quad (6.37)$$

In order to make this integration, a provisional estimate of the LAB needs to be made. This crude first order approximation is made by determining in which layer the temperature first rises above $1500K$, equation 6.38. The $1500K$ temperature lies between the $1200^\circ C$ and $1300^\circ C$ boundaries often used to denote the bottom of the (thermal) lithosphere, e.g. Artemieva and Mooney [2001].

$$n_{LAB} = max(i \text{ where } T_i < 1500K) \quad (6.38)$$

2. Distribute Δm There are infinitely many combinations of $\Delta\rho_i$ that satisfy equation 6.37. Here, like in chapter 5, it is important that the chosen density distribution model is realistic and robust. A general, robust, model for the distribution of $\Delta\rho_i$ is given in figure 6.8a. In this general model, the required density change ($\Delta\rho_{req}$) is kept constant up to depth z_{change} , after which $\Delta\rho_{req}$ decreases linearly to 0 at depth z_{nLAB} . In a cratonic setting this is interpreted as the lithospheric mantle being depleted to depth z_{change} and then slowly becoming richer, until, at depth z_{nLAB} the mantle has the same composition as the surrounding (primitive) mantle. Two end-members of the general model exist. One is the case where $z_{change} = 0$, in which case the lithospheric mantle is most depleted at the top and becomes steadily richer with increasing depth. The other end-member is the case where $z_{change} = z_{nLAB}$, in which case the lithospheric mantle has a constant depletion up to depth z_{nLAB} , where there is a sharp transition from depleted to undepleted mantle.

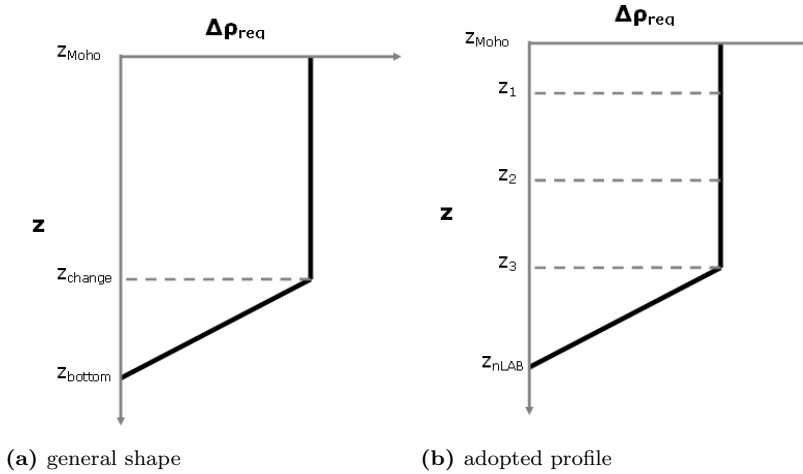


Figure 6.8: Distribution of required density changes with depth (see main text for further explanation)

The general model has been applied with $z_{change} = z_{nLAB-1}$ and $z_{bottom} = z_{nLAB}$ (equation 6.39). An example of the applied model where $n_{LAB} = 4$ is given in figure 6.8b.

$$\Delta\rho_{req,i} = \begin{cases} \frac{\Delta m_{req}}{(z_{nLAB} - z_{nLAB-1})/2 + (z_{nLAB-1} - z_{Moho})} & \text{if } i < n_{LAB} \\ 0 & \text{if } i \geq n_{LAB} \end{cases} \quad (6.39)$$

3. Adjust and choose composition The adjusted composition should have the desired density (equation 6.40), while respecting the observed V_s from the

tomography model. After $\Delta\rho_{req,k}$ ³ is determined, using equation 6.39, the composition is chosen (red block in figure 6.9). Next, the iron content is determined such that $\Delta\rho_{req,k}$ is satisfied (blue block in figure 6.9). Since the relation between composition, velocity and density, is non-linear, the iron content is determined iteratively.

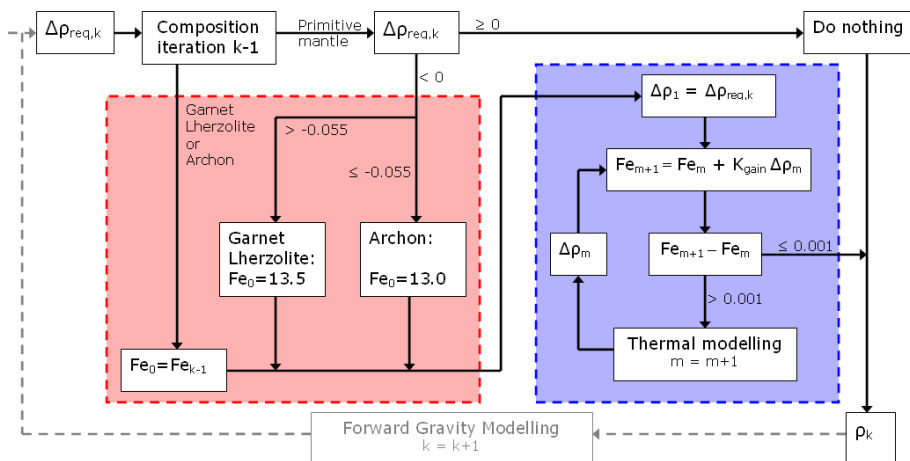


Figure 6.9: Decision tree for determining and updating lithospheric mantle composition

$$\rho_{k,i} = \rho_{k-1,i} + \Delta\rho_{req,k,i} \quad (6.40)$$

The first step in choosing the composition is recognizing what the composition has been in the previous iteration ($k - 1$). If the composition in the previous iteration is anything other than Primitive Mantle, simply use the same composition as in the previous iteration. The iron content of the previous iteration (Fe_{k-1}) is used as starting value in the second part of the composition adjustment (red block in figure 6.9). If the composition in the previous iteration was Primitive Mantle⁴, there are two possibilities. The first possibility is that $\Delta\rho_{req,k}$ is positive or zero. Since the density of the lithosphere can only be *lowered* by depleting its composition, a positive $\Delta\rho_{req,k}$ cannot be accommodated. In this case, composition is left unchanged. If $\Delta\rho_{req,k}$ is negative, the composition is changed to Archon (if $\Delta\rho_{req,k} \leq -0.055 gcm^{-3}$) or Garnet Lherzolite (if $-0.055 gcm^{-3} < \Delta\rho_{req,k} < 0 gcm^{-3}$). Since Garnet Lherzolite with a Fe of 0.13 has roughly the same velocity-density relation for cratonic areas, the initial iron content (Fe_0) is set to 0.13. For Archon Fe_0 is 0.135.

³Note that the index has changed between equation 6.39 and here. The index i , indicating the depth, z_i of the grid point under consideration, is omitted from here onwards. The index k instead indicates the number of the iteration over forward gravity modelling

⁴Note that in the initial run ($k = 0$) the composition is Primitive Mantle throughout the lithosphere, hence for $k = 1$ the previous composition will always be Primitive Mantle.

Determine Fe Once the composition is chosen, the amount of iron (Fe) needs to be determined. A guess for the Fe (Fe_m) is made based on the iron content in the previous composition (Fe_{m-1}) and the density difference that needs to be overcome $\Delta\rho_m$ (equation 6.41).

$$Fe_m = Fe_{m-1} + K_{gain}\Delta\rho_m \quad (6.41)$$

$$\Delta\rho_m = \Delta\rho_{req,k} - \Delta\rho_{achieved,m-1} \quad (6.42)$$

$\Delta\rho_m$ can be obtained by extracting from the required density change the achieved density change ($\Delta\rho_{achieved,m-1}$), equation 6.42. Since for $m = 1$ the achieved density change is 0, $\Delta\rho_1 = \Delta\rho_{req,k}$

K_{gain} in equation 6.41 is a so-called P-controller (e.g. Minorsky [1922]) converting a required density change into an estimated Fe change. In order for the iteration over m to converge, it is important that K_{gain} is accurate. If K_{gain} is too large, the iteration will not converge. If K_{gain} is too small, the iteration will converge to a wrong value. Since the density of a composition changes by roughly $0.13gcm^{-3}$ when Fe changes with 0.01 (section 6.4.1), K_{gain} is set to $\frac{1}{13}$.

The estimated Fe is used, together with the composition (Archon, Garnet Lherzolite or Primitive Mantle), in thermal modelling to obtain a new density estimate ($\rho_{k,m}$). This new density estimate is compared with the density estimated in the previous, $k - 1$, iteration (ρ_{k-1}), equation 6.43. The achieved density change forms the basis for a new estimate of Fe (Fe_{m+1}).

$$\Delta\rho_{achieved,m} = \rho_{k,m} - \rho_{k-1} \quad (6.43)$$

This process is repeated until convergence is reached for Fe , i.e. $Fe_m - Fe_{m-1} < 0.001$. When convergence is reached, usually after no more than four iterations, the composition is frozen and the last density estimate $\rho_{k,m}$ is used as the new density ρ_k . The new density ρ_k is used in forward gravity modelling to obtain a new modelled gravity disturbance and $\Delta\rho_{req,k+1}$, after which the whole process starts over again. The iteration over k is repeated until there are no changes in composition and the change in $Fe < 0.005$ for each gridpoint. The results of the analysis of the upper mantle are presented in section 6.5.

6.5 Results

Starting with Primitive Mantle (table 6.4) throughout the uppermost mantle, the density and temperature were computed (section 6.1). The densities obtained through the thermal modelling were used to compute a modelled gravity anomaly (section 6.2). This modelled anomaly was compared to the observed gravity anomaly. Any difference is interpreted to be caused by a difference in composition, connected to differences in density. By iteratively updating the composition, a fit to the gravity anomaly was obtained for the cratonic areas (section 6.4). The final model consists of Archon, Garnet Lherzolite and Primitive Mantle, figure 6.10a. It should be noted that Archon and Garnet Lherzolite

are only used in the lithospheric mantle ($T < 1500K$, section 6.4.2) and Primitive Mantle was used throughout the whole asthenospheric mantle.

It can be seen from the final fit of the gravity anomaly (figure 6.10c, expressed as a required density change $\Delta\rho_{req}$, equation 6.35) that updating the composition removed the misfit of the gravity disturbance (figure 6.6). The resulting model shows that the estimated iron content (Fe) changes rapidly in the cratonic areas, figure 6.10b.

Figure 6.12 shows that the mantle is coldest beneath the Siberian Craton and the East European Platform, being much colder than ambient up to depths of $150km$ for the Siberian Craton and even up to $200km$ for the East European Platform. The Indian craton shows a smaller cold root, which is mostly indiscernible at depths below $100km$. The lack of a cold lithospheric mantle root in the Sino-Korean craton can be caused by either the root being eroded away, or peeled off [Griffin et al., 1998, Zheng et al., 1998]. The mantle beneath the Alpine-Himalayan convergence zone is warmer than ambient, and shows up most pronounced at depths of $100km$ and $150km$. Densities corresponding with the thermal model are given in figure 6.12.

Temperatures in the cratonic areas are generally colder than in the study of Artemieva and Mooney [2001], with difference up to $200^{\circ}C$, though adjacent Lake Baikal has temperatures of up to $200^{\circ}C$ warmer. On average, temperatures as predicted in this study are almost $100^{\circ}C$ colder at depths of $100km$ and $150km$, but at depths of $200km$ temperatures are on average $30^{\circ}C$ warmer than in Artemieva and Mooney [2001]. An explanation for this difference could be that in this study a depleted composition is used in cratonic areas at depths up to $150km$ which generally lowers the temperature. In contrast, below the thermal LAB (figure 6.13) at $200km$, the primitive mantle composition (table 6.4) is used throughout the whole mantle.

Uncertainties in the temperature model are in the order of $100^{\circ}C$, provided the composition is accurately determined [Cammarano et al., 2003]. Erroneous composition could at most add another $100^{\circ}C$ to this uncertainty (see figure 6.7, where different compositions are compared).

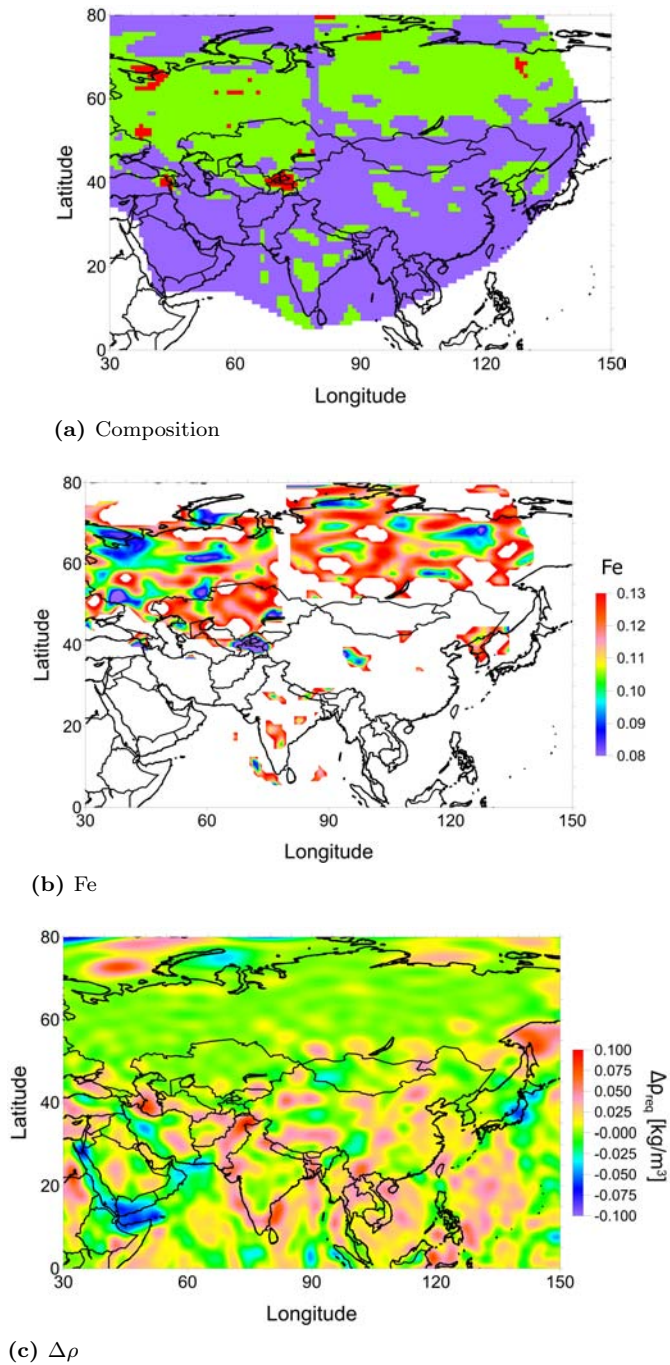
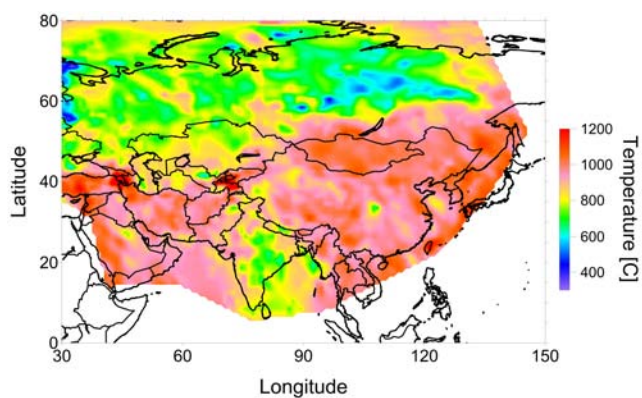
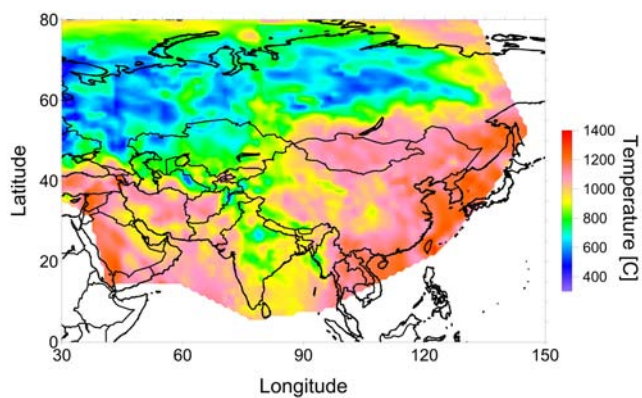


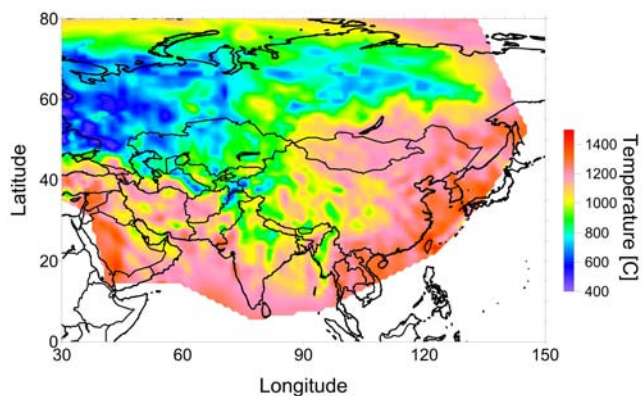
Figure 6.10: [a] Petrological composition (red = Archon, green = Garnet Lherzolite, purple = Primitive Mantle), [b] iron fraction (Fe) and [c] fit to the gravity anomalies after the final iteration



(a) 50km

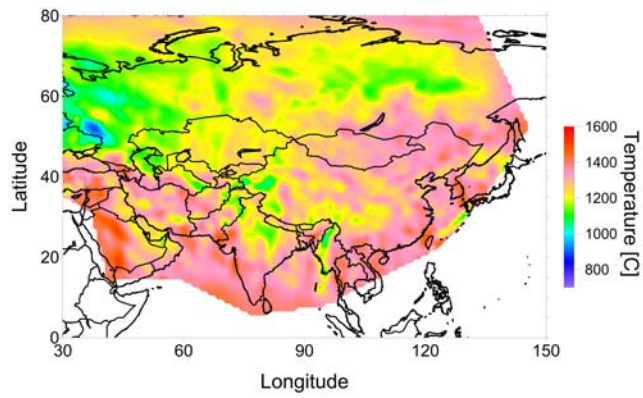


(b) 100km

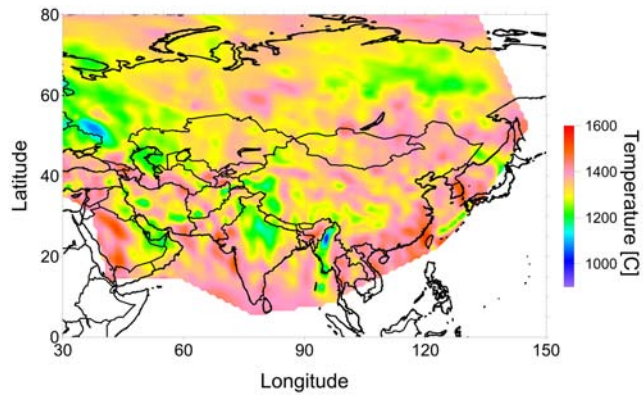


(c) 150km

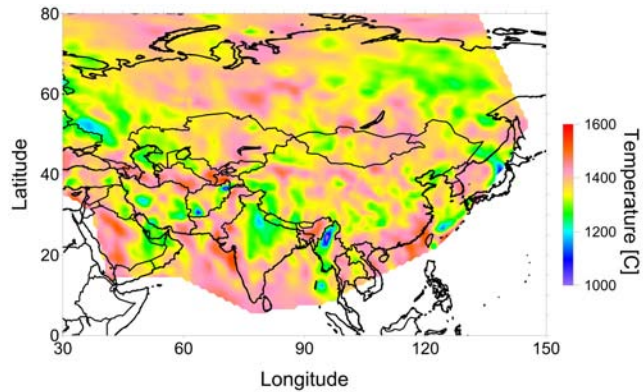
Figure 6.11: Estimated temperature in the uppermost mantle at various depth levels



(d) 200km

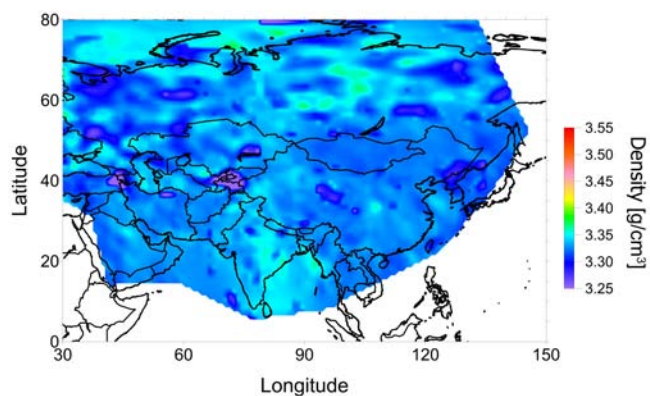


(e) 250km

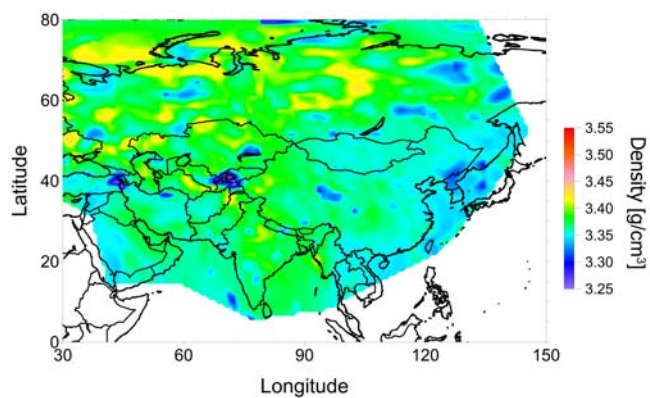


(f) 300km

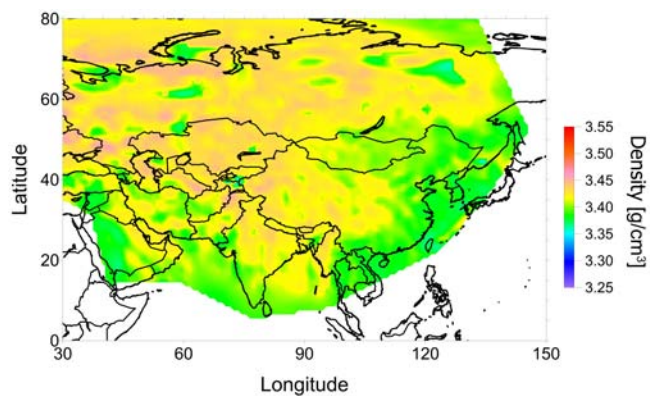
Figure 6.11: Estimated temperature in the uppermost mantle at various depth levels (continued)



(a) 50km

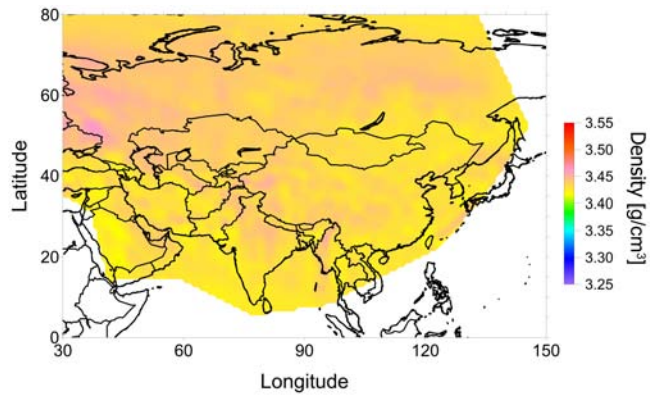


(b) 100km

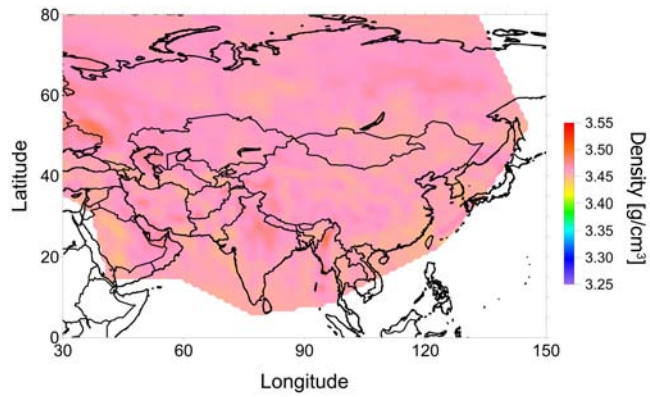


(c) 150km

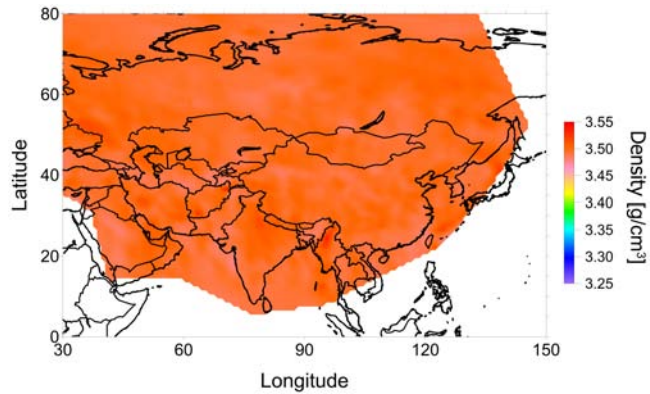
Figure 6.12: Inferred density structure in the uppermost mantle at various depth levels



(d) 200km



(e) 250km



(f) 300km

Figure 6.12: Inferred density structure in the uppermost mantle at various depth levels (continued)

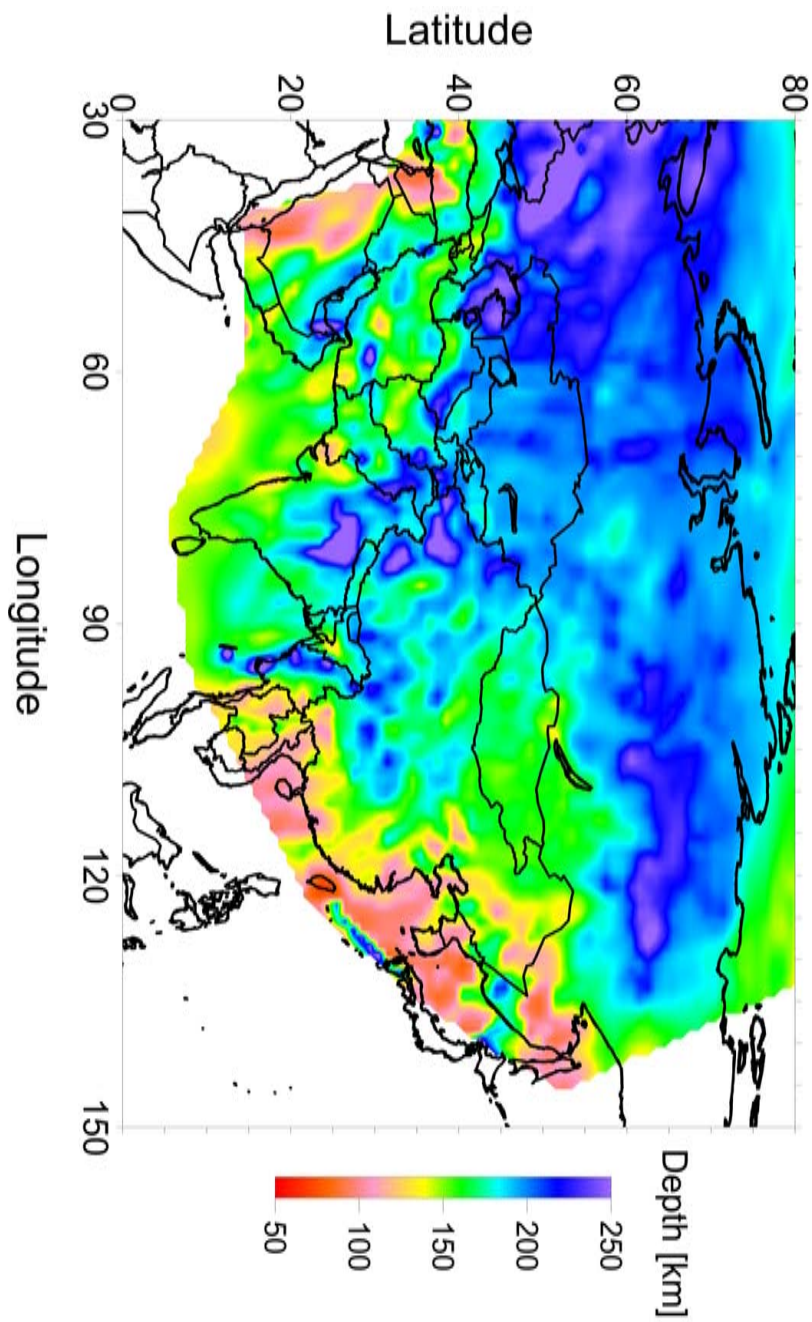


Figure 6.13: Estimated depth to the bottom of the lithosphere (portrayed as the 1200°C isotherm)



Models of lithospheric strength: A first assessment

The main results of this study are various high-resolution 3D models that provide an improved characterization of the continental lithosphere of Asia. After discussing the different data sets used in this thesis in chapter 2, a model for the sedimentary cover in the study area was presented in chapter 3. A new model for the depth to the Moho discontinuity was presented in chapter 4 and the distribution of pressure wave velocities in the crust was discussed in chapter 5. Using a combination of seismic tomographic studies and analysis of gravity anomalies led to a thermal and density model of the lithospheric mantle in chapter 6.

One of the main applications of the new high-resolution 3D-thermal density models presented in this thesis is the examination of the effect of a non-uniform mechanical lithosphere on the Eurasian intra-plate stress field and consequences for different modes of intra-continental deformation of the Asian lithosphere (e.g. Warners-Ruckstuhl et al. [2012, 2013]). This is important as limited available stress field indicator data do not provide information on stress magnitude and cover only part of Eurasia (figure 7.1, Heidbach et al. [2008]).

A first objective in such an analysis would be the assessment of lateral variations in lithospheric strength. In this final chapter a first, tentative step to assess such lateral variations in lithospheric strength is made by exploring the parameter space of some relatively straightforward models (section 7.1). Preliminary conclusions on the lateral heterogeneity in the lithospheric strength in Asia are drawn (section 7.2). A prime aim of this chapter is to illustrate and discuss the uncertainties involved in using such first order (approximate) models (section 7.3). An analysis of the causes of these uncertainties leads to recommendations for future studies (section 7.4).

7.1 Rheology of the lithosphere

The total integrated strength of the lithosphere is given by the integrand of equation 7.1 where σ_1 is the maximum principle stress and σ_3 the minimum principle stress.

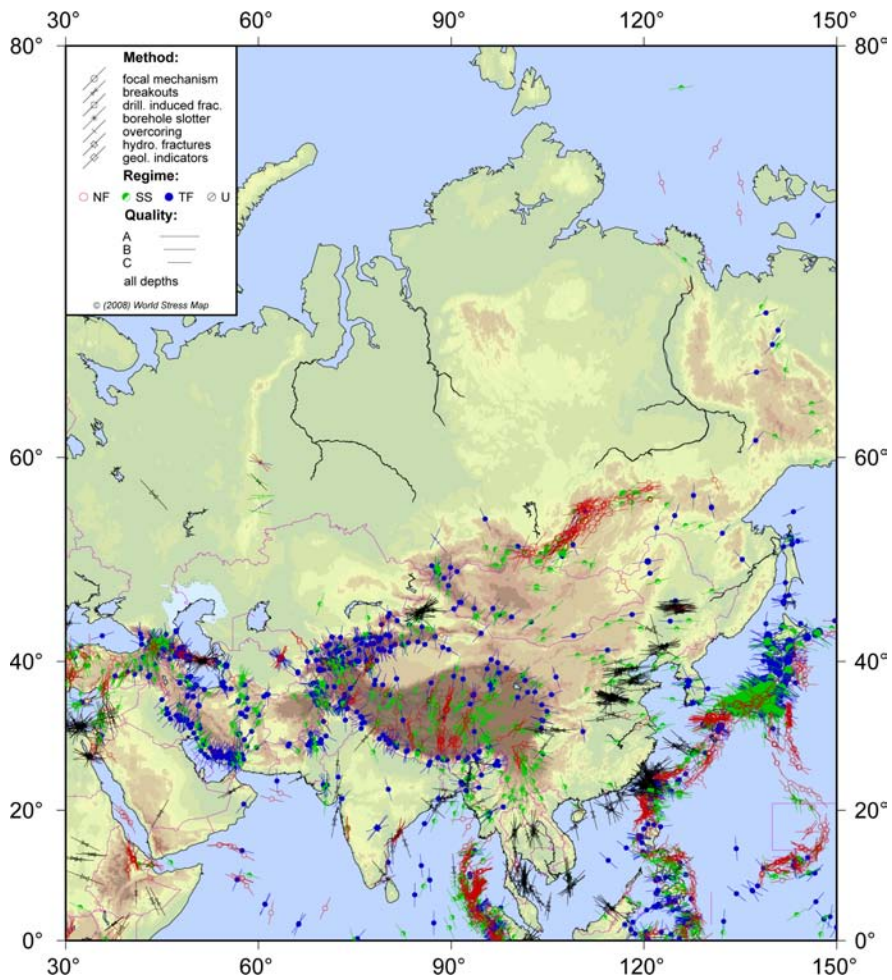


Figure 7.1: World Stress Map observations for Asia [Heidbach et al., 2008]

$$\sigma_L = \int_{z_{topo}}^{z_{LAB}} (\sigma_1 - \sigma_3) dz \quad (7.1)$$

The maximum allowable difference between the maximum and minimum principal stresses ($\sigma_1 - \sigma_3$) is determined by the dominant rock deformation mechanism at that depth, usually either brittle failure (section 7.1.1) or viscous creep (section 7.1.2).

7.1.1 Brittle failure

When the confining pressure and temperature are low, the predominant mode of failure is brittle failure. The yield criterion in the brittle regime can be described by Byerlee's law [Byerlee, 1978], written in terms of principal stress difference according to Ranalli [1987], equation 7.2.

$$\sigma_{Byerlee}(z) = \sigma_1 - \sigma_3 = \alpha_{byerlee} (1 - \lambda_{hpff}) \int_{z_{top}}^z \rho(\hat{z}) g d\hat{z} \quad (7.2)$$

In equation 7.2, $\rho(\hat{z})$ denotes density as a function of depth (z) and g is the gravitational acceleration. The parameter $\alpha_{byerlee}$ is dependent on the type of faulting, and is given in equation 7.3.

$$\alpha_{byerlee} = \begin{cases} \frac{\Gamma-1}{\Gamma} & \text{normal fault} \\ \Gamma-1 & \text{thrust fault} \end{cases} \quad (7.3)$$

Γ is given in equation 7.4 in which $\mu_{friction}$ is the (static) sliding friction coefficient.

$$\Gamma = \left(\sqrt{1 + \mu_{friction}^2} - \mu_{friction} \right)^{-2} \quad (7.4)$$

A typical value for $\mu_{friction}$ is 0.75 [Ranalli, 1987], but $\mu_{friction}$ can vary around this value. The influence of variations of $\mu_{friction}$ on the stress-depth relation is shown in figure 7.2a. The hydrostatic pore fluid factor λ_{hpff} can vary between 0 and 0.85, particularly in sedimentary rocks, and is assumed to be 0 at depths larger than 15km where rocks no longer have any porosity. The effect of variations λ_{hpff} on the Byerlee strength profile are displayed in figure 7.2b.

7.1.2 Viscous creep

Steady state creep in the ductile parts of the lithosphere is empirically described by a non-Newtonian power law, equation 7.5 [Kirby, 1983]. This powerlaw relates the critical principle stress difference ($\sigma_1 - \sigma_3$) needed to maintain a steady-state strain-rate to a power (n) of that strain-rate ($\dot{\epsilon}$), hence the name power law creep. In the power law, the constant (A_p), activation energy (E_p) and exponent (n) are material properties (table 7.1), generally assumed to be invariant with respect to temperature (T), pressure (P) and strain-rate ($\dot{\epsilon}$), in modelling studies of lithosphere deformation (e.g. Beekman [1994], Cloetingh and Burov [1996], Cloetingh et al. [2008]) and lithosphere strength (e.g. Tesauro et al. [2009]).

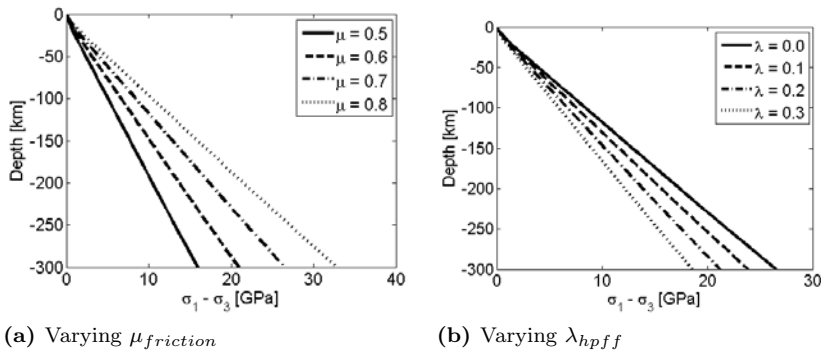


Figure 7.2: Brittle failure stress-depth relation, according to Byerlee’s law, using the pressure-depth relations from Preliminary Reference Earth Model (PREM) [Dziewonski and Anderson, 1981]

Table 7.1: Power law creep parameters

Mineral	dry (d)/ wet (w)	exponent n	activation energy E_p	constant A_p	Source
CPX	d	5.8	$330 * 10^3$	$2.51 * 10^{-43}$	Carter and Tsen [1987]
Garnet	d	2.22	$485 * 10^3$	$2.8 * 10^{-7}$	Ji and Martignole [1994]
Olivine	d	3.0	$510 * 10^3$	$7.00 * 10^{-14}$	Goetze and Evans [1979]
OPX	d	2.4	$293 * 10^3$	$1.56 * 10^{-15}$	Carter and Tsen [1987]

$$\sigma_{Power} = \sigma_1 - \sigma_3 = \left(\frac{\dot{\epsilon}}{A_p} \right)^{\frac{1}{n}} e^{\frac{E_p}{nR_{gas}T}} \quad (7.5)$$

Temperature-stress curves, using the parameters of table 7.1, show that large differences exist between the different minerals (figure 7.3a). However, since the composition of the lithospheric mantle is dominated by olivine (table 6.4), the differences between Archon, Garnet Lherzolite and Primitive Mantle are small (figure 7.3b).

The critical principle stress difference ($\sigma_1 - \sigma_3$) needed to maintain a steady state creep is not a material property in the sense that it solely depends on the material under consideration. Strain-rate ($\dot{\epsilon}$) has a significant influence on the critical ($\sigma_1 - \sigma_3$) (figure 7.4). Strain-rate is often not well constrained, especially at larger depths, and can generally vary between $\dot{\epsilon} = 10^{-14} s^{-1}$ and $\dot{\epsilon} = 10^{-17} s^{-1}$, but could be even slower in stable (cratonic) areas (values from the global strain-rate map [Kreemer et al., 2000] and Kreemer et al. [2003]). Despite these variations, a strain-rate of $\dot{\epsilon} = 10^{-16} s^{-1}$ is assumed to be characteristic

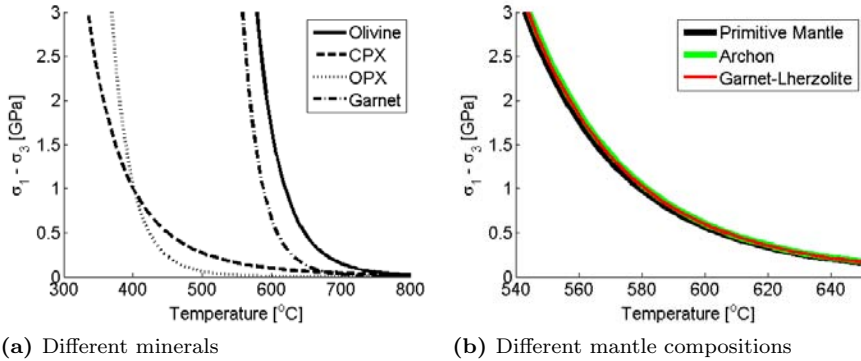


Figure 7.3: Temperature- $(\sigma_1 - \sigma_3)$ relation according to the power law, assuming a constant $\dot{\epsilon}$ of 10^{-16}s^{-1}

as bulk strain-rate for most continental lithosphere deformation processes (e.g. Carter and Tsenn [1987], Cloetingh et al. [2008], Tesauro et al. [2009]).

Inspecting figure 7.3 shows that the vertical transition from very strong lithospheric mantle ($> 1.5 \text{GPa}$) to weak lithosphere ($< 100 \text{MPa}$)¹ occurs over an interval of roughly 100°C (figure 7.5). This interval is relatively small, considering that the uncertainty of the temperature model also being roughly 100°C , assuming that the composition is sufficiently well resolved [Cammarrano et al., 2003]. This means that due to the uncertainty in the thermal modelling (figure 7.5), there exists a certain temperature range for which it is impossible to resolve whether the ductile lithosphere is either relatively strong or relatively weak (compared to the strength of the crust).

7.2 Strength of the Asian lithosphere

The strength-depth/temperature laws described in sections 7.1.1 and 7.1.2 can be applied to the thermal and density model for Asia presented in chapter 6. This leads to a maximum stress-depth profile for every grid point in the model. These $(\sigma_1 - \sigma_3)$ -depth profiles can be integrated using equation 7.1 to derive estimates for present-day integrated lithospheric strength. The resulting lithosphere strength map for Asia is presented in figure 7.6 for compressional and in figure 7.7 for tensile strength.

The integrated strength of the lithosphere can be split into crustal and mantle components (figure 7.8 for compression and figure 7.9 for tensile strength). Crustal thickness variations across Asia have a large influence on the integrated strength of the crust, see for example Tibet in figures 7.8a and 7.9a. The variations in integrated strength of the lithospheric mantle are related to temperature

¹For mantle lithosphere Tesauro et al. [2009] have $(\sigma_1 - \sigma_3)$ in excess of 1.5GPa only occurring in the East European Platform, values in the order of 100MPa occur under the Pyrenees, Alps and Appenines for instance

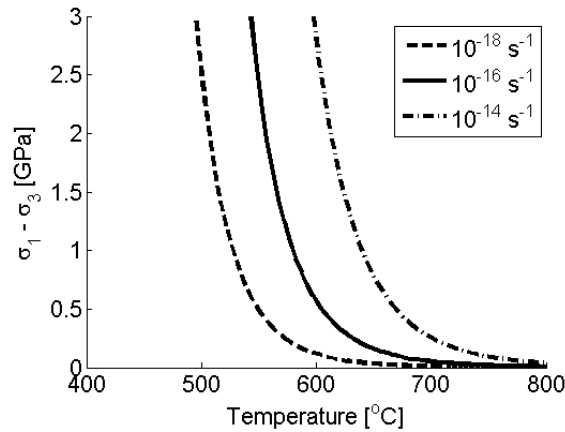


Figure 7.4: Dependence of the powerlaw on the strain-rate ($\dot{\epsilon}$)

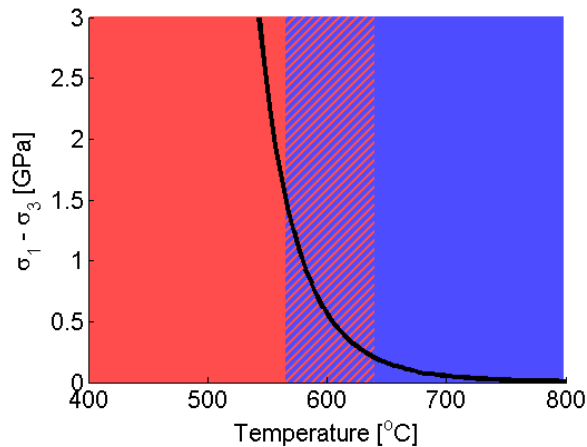


Figure 7.5: The transition from strong (red) to weak (blue) ductile lithosphere occurs over roughly 100°C taken with the uncertainty in the thermal modelling, this leads to a transition zone (striped) where it cannot be determined whether the lithosphere is strong or weak

variations (compare with figure 6.11), with a stronger lithospheric mantle in the north-west (concentrated around the Siberian Craton and East European Platform) and a weak lithospheric mantle in the south-east. Figure 7.10 shows the same integrated strength of the lithospheric mantle, with a colour scale focussing on the lower strengths.

Intra-plate earthquakes (thus excluding seismicity at plate boundaries and in down going lithospheric slabs) occur primary in the crust [International Seismological Centre, 2011]. Furthermore, figure 7.8b shows that these intra-plate earthquakes occur in areas with a relatively weak lithospheric mantle. This

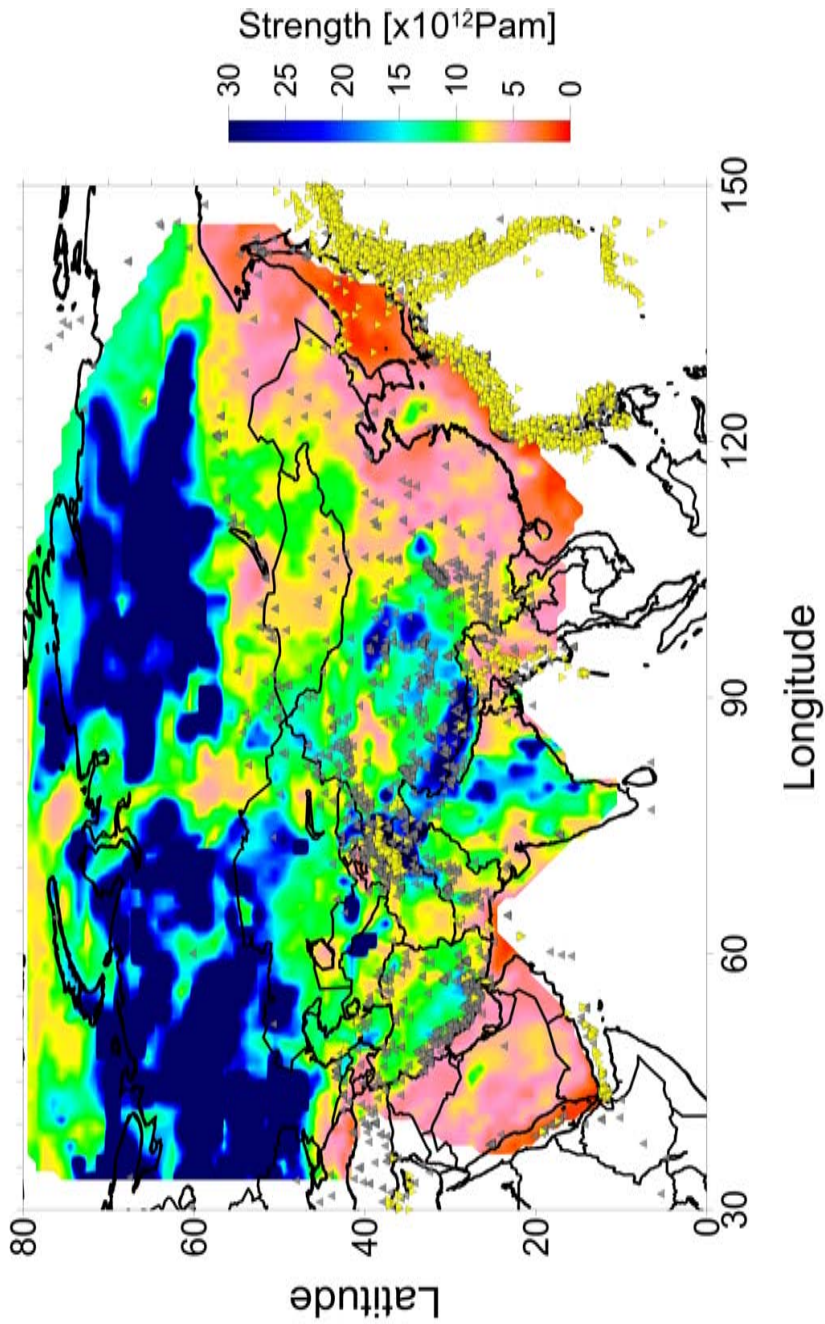


Figure 7.6: Integrated strength of the lithosphere under compression (triangles show earthquake locations for the period 2008-2012, with magnitude > 4 , grey = earthquakes in the crust, yellow = earthquakes below Moho depth [International Seismological Centre, 2011])

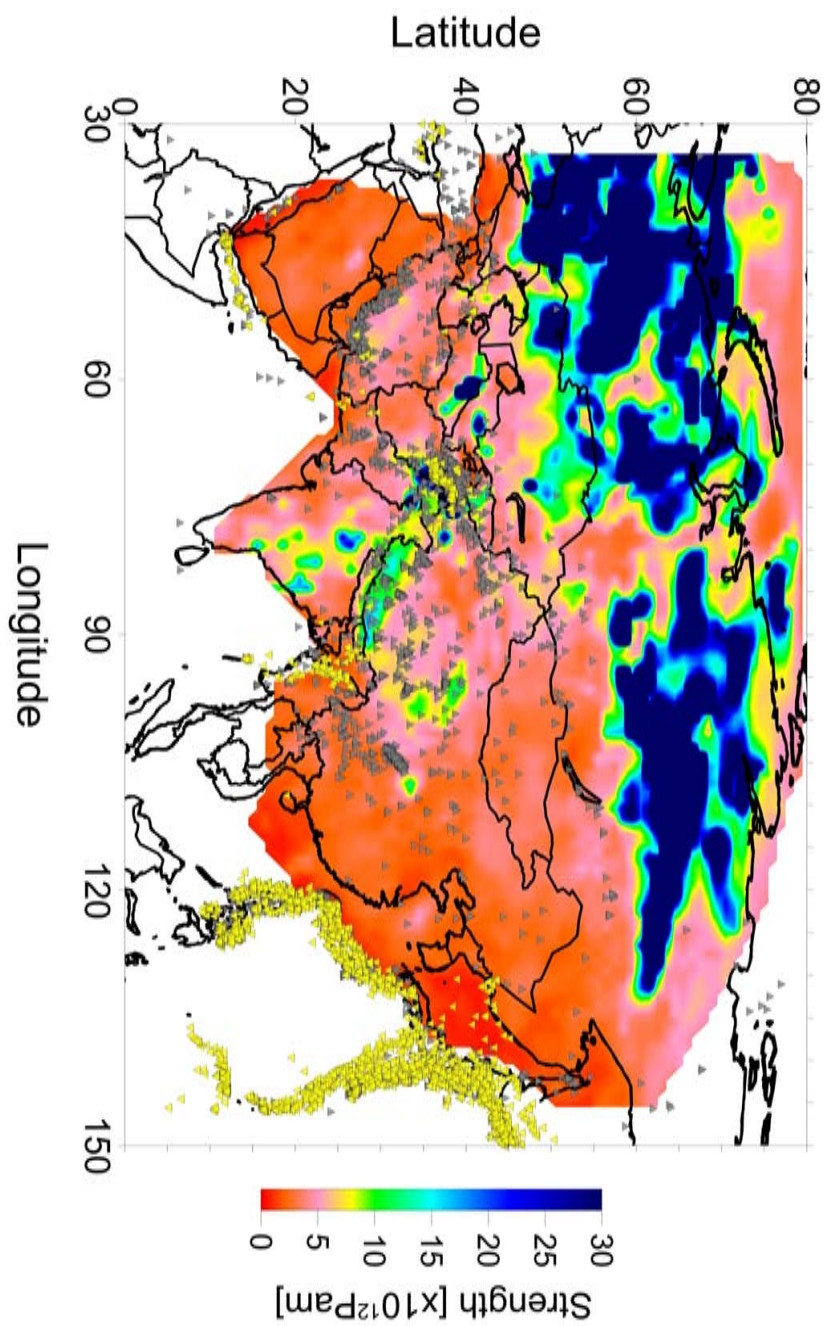
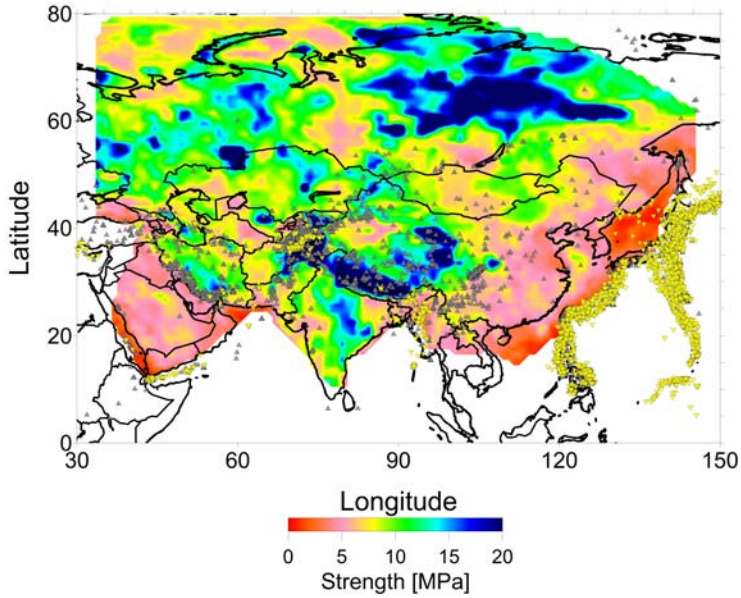
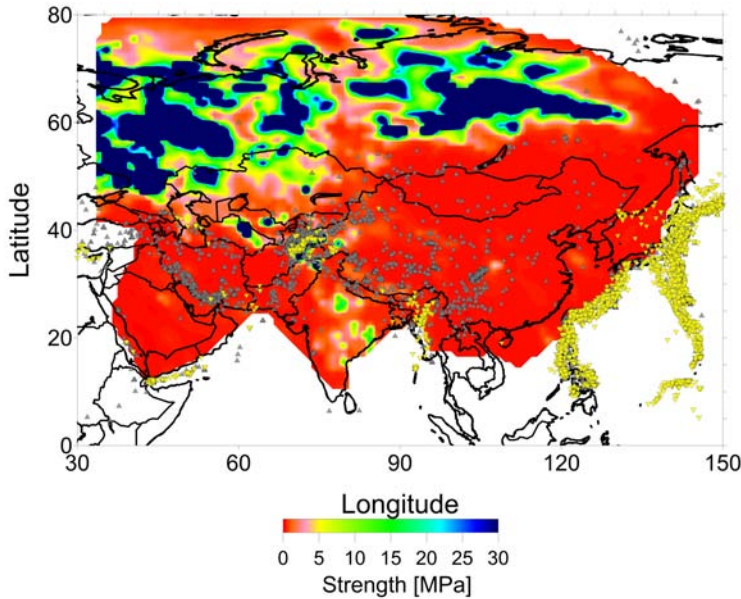


Figure 7.7: Integrated strength of the lithosphere in tension (triangles show earthquake locations for the period 2008-2012, with magnitude > 4 , grey = earthquakes in the crust, yellow = earthquakes below Moho depth [International Seismological Centre, 2011])

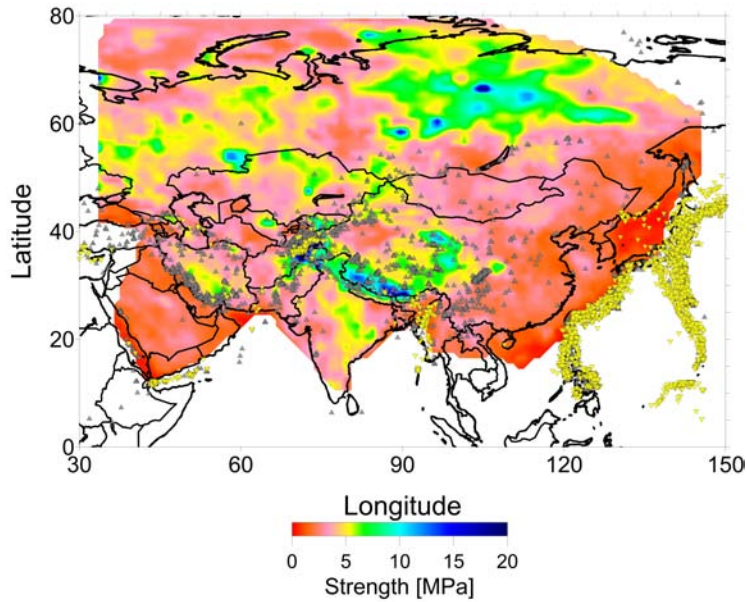


(a) crust

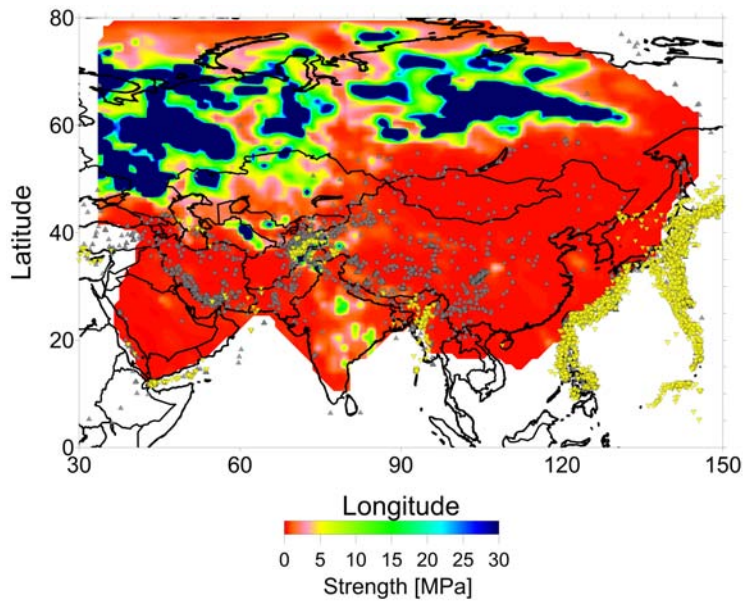


(b) lithospheric mantle

Figure 7.8: Integrated maximum lithospheric strength under compression in the crust (top panel) and lithospheric mantle (bottom panel) (triangles show earthquake locations for the period 2008-2012, with magnitude > 4 , grey = earthquakes in the crust, yellow = earthquakes below Moho depth [International Seismological Centre, 2011], please note different colour bars)



(a) crust



(b) lithospheric mantle

Figure 7.9: Integrated maximum lithospheric strength in tension in the crust (top panel) and lithospheric mantle (bottom panel) (triangles show earthquake locations for the period 2008-2012, with magnitude > 4 , grey = earthquakes in the crust, yellow = earthquakes below Moho depth [International Seismological Centre, 2011], please note different colour bars)

strong correlation can not be observed between earthquake locations and the integrated strength of the crust (figure 7.8a). An explanation for this correlation can be that in areas where the mantle lithosphere is weak, stresses concentrate in the crust and earthquakes occur (e.g. Cloetingh and Banda [1992]).

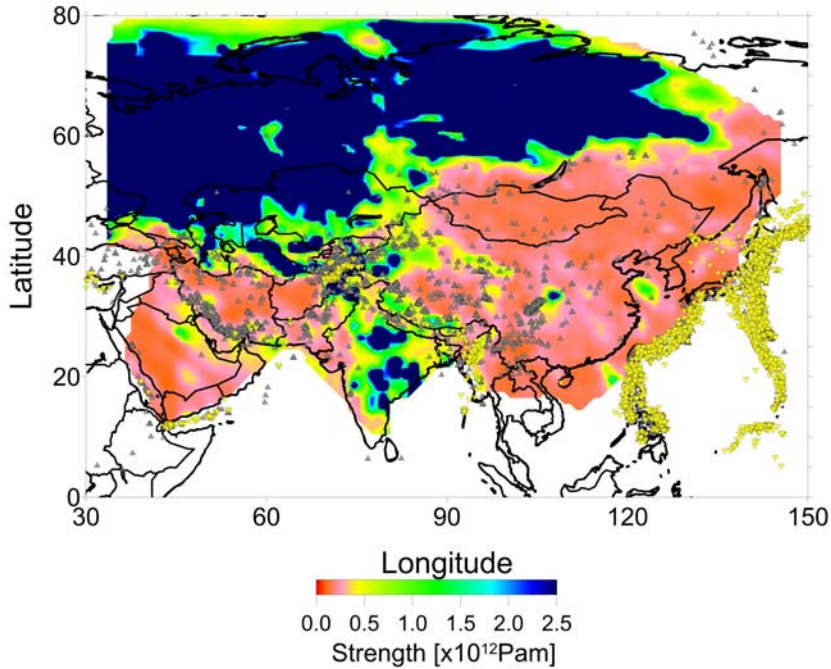


Figure 7.10: Integrated maximum lithospheric mantle strength under compression, with a colour bar different from figure 7.8b (triangles show earthquake locations for the period 2008-2012, with magnitude > 4 , grey = earthquakes in the crust, yellow = earthquakes below Moho depth [International Seismological Centre, 2011])

Areas with a weak lithospheric mantle are also the areas where the relative crustal strength (expressed as a percentage of the total strength of the lithosphere) is largest (figure 7.11). According to this model the lithospheric strength appears to behave according to the 'crème brûlée' model (e.g. Maggi et al. [2000], Jackson [2002b]) in these areas. The Siberian craton and the East European Platform and their surroundings on the other hand behave, in this model, according to the 'jelly sandwich' model (e.g. Handy and Brun [2004], Burov and Watts [2006]).

Representative $(\sigma_1 - \sigma_3)$ -depth profiles have been plotted for several areas (figure 7.12). These 1D vertical profiles again demonstrate the heterogeneous character of the Asian continental lithosphere. Large differences exist even between cratons. In the Siberian Craton most of the integrated strength is provided by the lithospheric mantle (figure 7.12a). This is less, though still considerable, in the Indian Craton (figure 7.12g). A lithospheric root seems to be missing

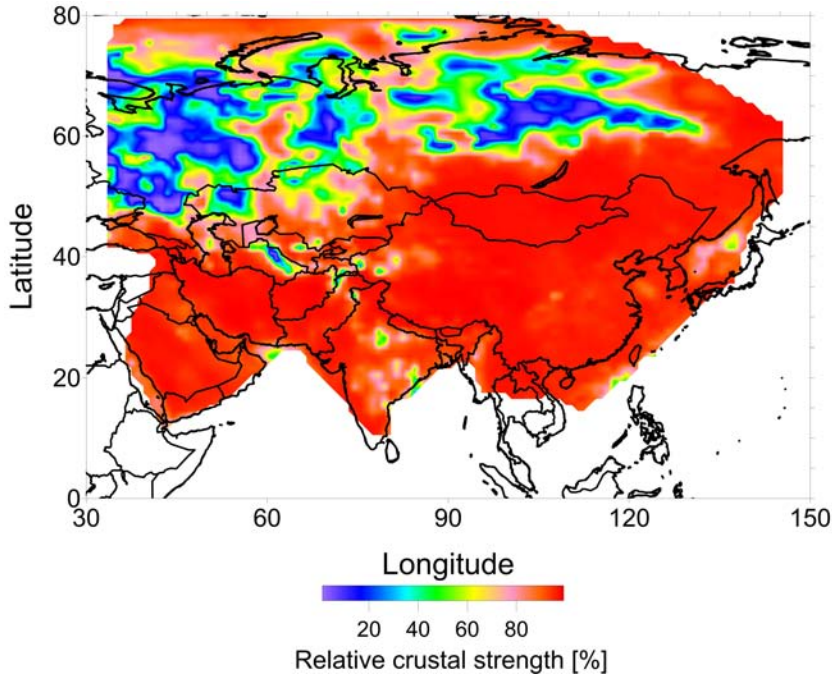


Figure 7.11: Proportion of the integrated crustal strength relative to the total integrated lithospheric strength

completely in the Sino-Korean Craton (7.12k), which is also acknowledged by Zheng et al. [1998], Griffin et al. [1998]. The absence of a cold lithospheric root could be a cause for instability of the Sino-Korean Craton [François et al., 2013].

The negative gradient between 75km and 150km in the temperature-depth curve for Tibet (figure 7.12j) may be caused by colder than ambient sinking slab material. Another explanation might be the assumption of an incorrect mantle composition, since the compositional changes based on observed gravity anomalies have not been applied in the Tibetan area (see chapter 6).

7.3 Uncertainties in strength modelling

Uncertainties in the various parameters in Byerlee’s law (equation 7.2) and the power law (equation 7.5), such as T , $\dot{\epsilon}$, λ_{hpff} and $\mu_{friction}$ can have significant effect on the $(\sigma_1 - \sigma_3)$ -depth profiles. This section discusses the uncertainties in the strength models presented in this chapter. Firstly, the effect of uncertainties in temperature are discussed for the whole of the Asian continent. Secondly, several more aspects of the uncertainty in the strength model are discussed by focussing on a Urals profile.

To assess the $100 - 200^\circ\text{C}$ uncertainties in the thermal model also the integrated lithospheric strength has been determined for a model where the mantle

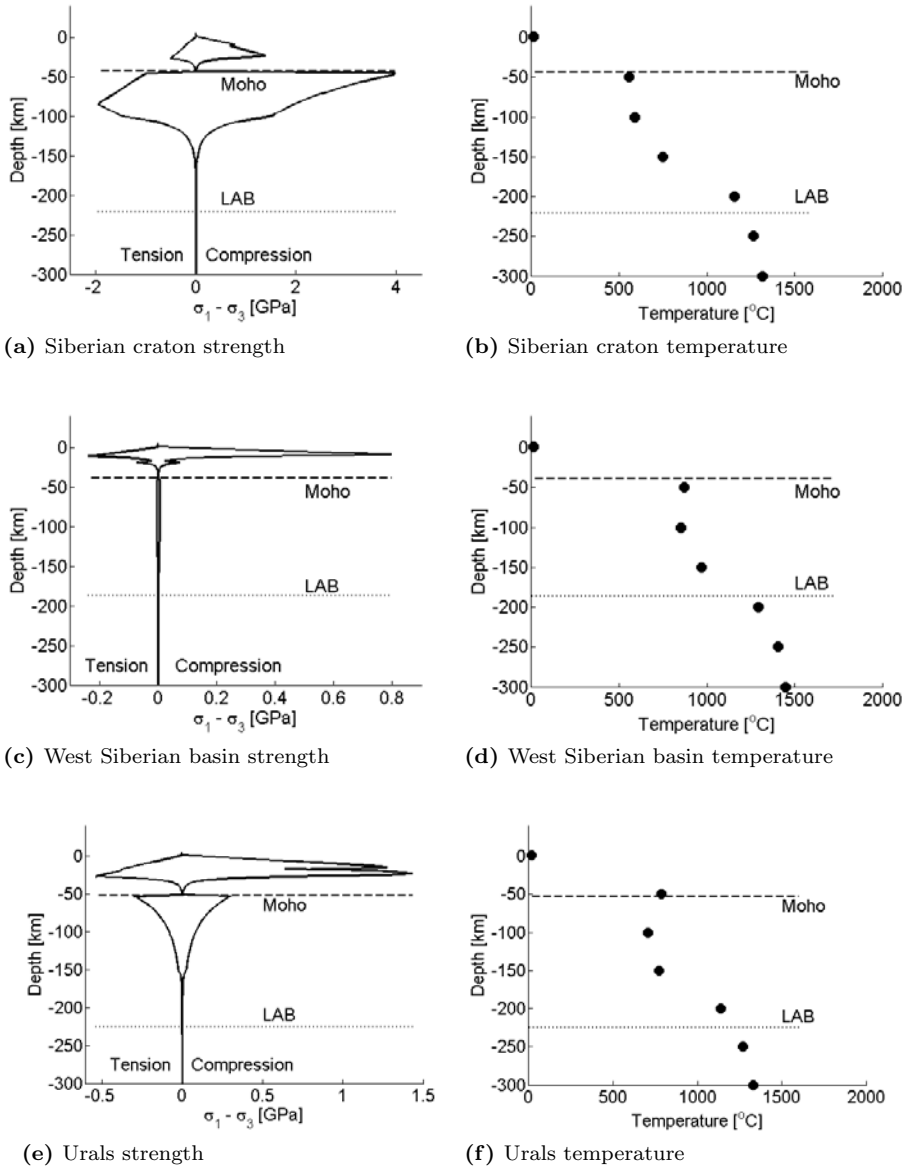
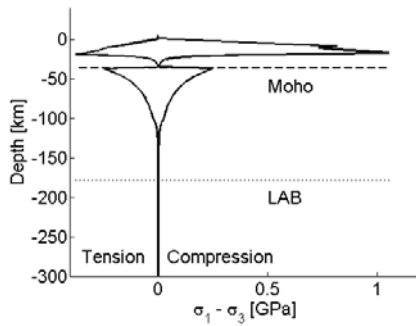
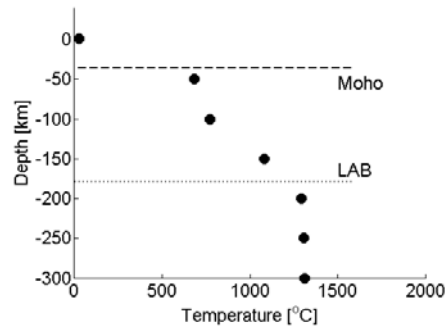


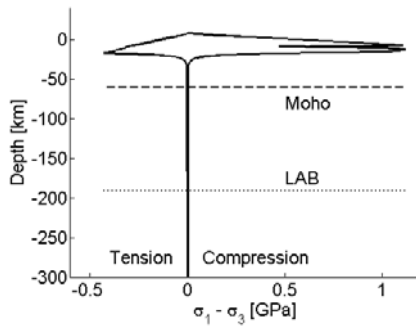
Figure 7.12: *Left:* 1D Strength profiles of the Asian lithosphere, with depth to Moho (dashed line) and thermal LAB (dotted line); *Right:* Temperature estimates inferred from tomography in 50km depth intervals (see chapter 6)



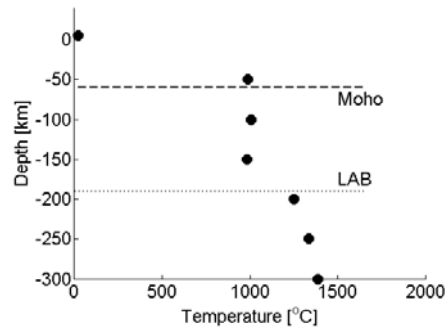
(g) India strength



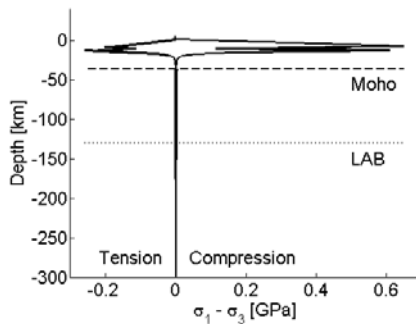
(h) India temperature



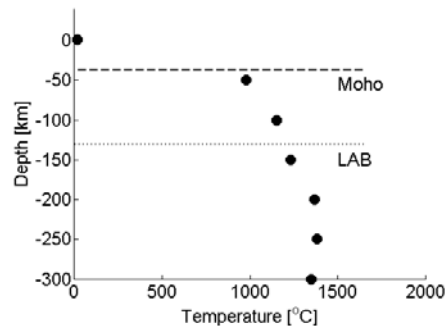
(i) Tibet strength



(j) Tibet temperature



(k) North-east China strength



(l) North-east China temperature

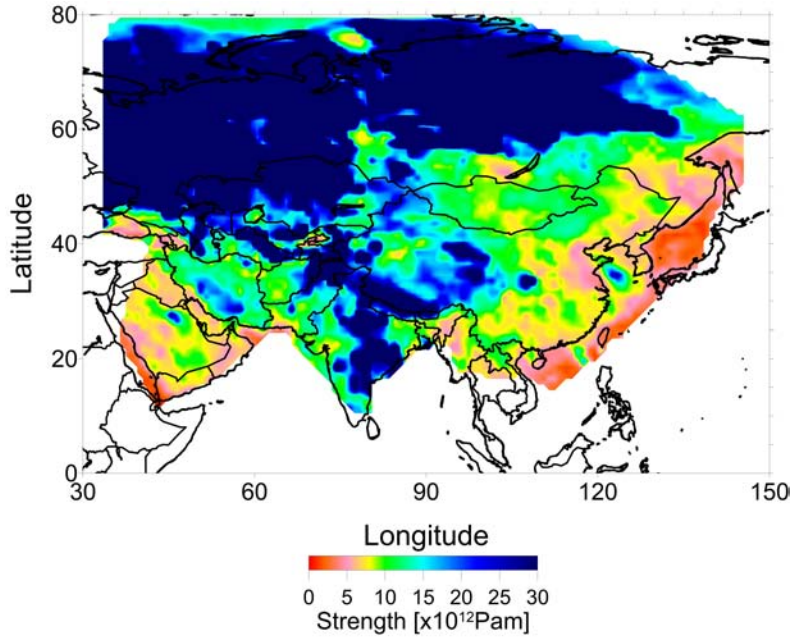
Figure 7.12: *Left:* 1D Strength profiles of the Asian lithosphere, with depth to Moho (dashed line) and thermal LAB (dotted line); *Right:* Temperature estimates inferred from tomography in 50km depth intervals (see chapter 6) (continued)

temperatures were reduced by 100°C (figure 7.13a) and a model where the mantle temperatures were elevated by 100°C (figure 7.13b). Comparing these three lithospheric strength models allows for a classification of the study area into three main types: strong lithosphere, weak lithosphere and indeterminate (figure 7.14).

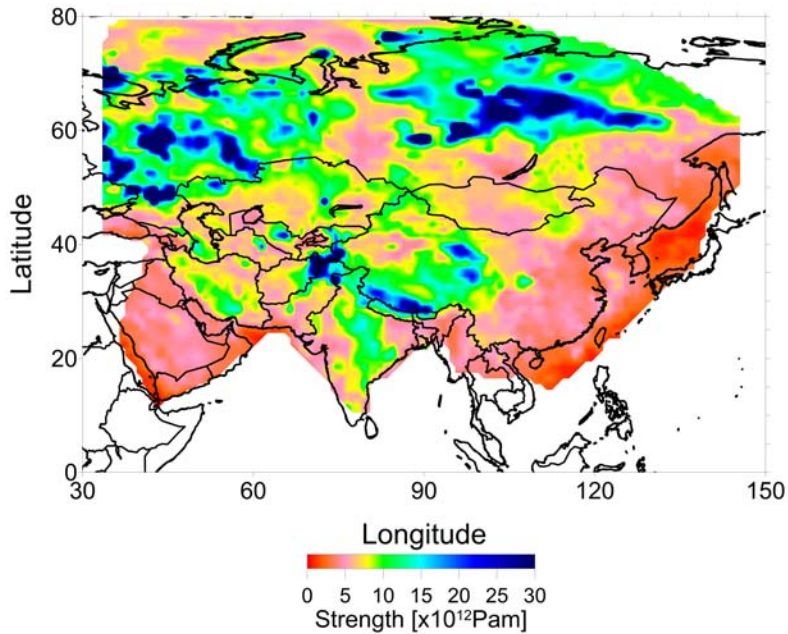
It should be noted that in the strength modelling presented here the crustal strength is overestimated, due to the assumed low λ_{hpff} and a relative high $\mu_{friction}$. This in turn leads to overestimation of the relative strength of the crust with respect to the mantle (figure 7.11). Furthermore, in this research a linear crustal temperature profile is assumed, increasing from an average surface temperature between 0°C and 30°C , depending on latitude, down to the Moho temperature which is extrapolated from the lithospheric mantle temperatures derived in chapter 6. This could either over- or underestimate actual crustal temperatures, adding to the uncertainty in crustal strength. An alternative approach would be to compute a crustal temperature profile based on surface heat flow and radiogenic heat production in the crust (following e.g. Artemieva and Mooney [2001] or more recently Van Wees et al. [2009]). However, variations in both surface heat flow and radiogenic heat production have large effects on the resulting crustal temperature profile, and especially the latter is not well constrained in Asia. Future regional studies should further investigate impact of spatial variations in radiogenic heat production in the crust and surface heat flow.

The effect of uncertainties in the strength parameters on the integrated lithospheric strength was tested for the Ural profile (figure 7.12e). Varying the temperature profile with 100°C has the most profound effect on the $(\sigma_1 - \sigma_3)$ -depth curve (figure 7.15a), though a variation in the strain-rate by plus or minus two orders of magnitude ($\dot{\epsilon} = 10^{-18}\text{s}^{-1}$, $\dot{\epsilon} = 10^{-16}\text{s}^{-1}$ and $\dot{\epsilon} = 10^{-14}\text{s}^{-1}$ respectively) also has a pronounced effect on the strength of the lithospheric mantle (figure 7.15b, see also table 7.4). Varying the (static) friction coefficient $\mu_{friction}$ between 0.5 and 0.75 (figure 7.15c) and the hydrostatic pore fluid factor λ_{hpff} between 0.0 and 0.4 (figure 7.15d) affects only the linear part of the $(\sigma_1 - \sigma_3)$ -depth curve determined by Byerlee's law. In the case of the Urals, Byerlee's law only affects the crust and hence changes in λ_{hpff} and $\mu_{friction}$ only influence the integrated strength of the crust (table 7.3). The impact of changes in λ_{hpff} and $\mu_{friction}$ then depends on the relative strength of the lithospheric mantle (table 7.4).

The integrated strength of the lithosphere for this Ural profile under varying parameters (table 7.2) shows the same behaviour as the separate profiles (figure 7.15). Variations in temperature (h) of $\pm 100^{\circ}\text{C}$ have the largest effect on the integrated strength of the lithosphere, followed by variations in the strain-rate ($\dot{\epsilon}$) of around two orders of magnitude, both of which affect the lithospheric mantle strength more than the crustal strength (provided the lithospheric mantle has some strength). Parameters $\mu_{friction}$ and λ_{hpff} only affect the lithospheric mantle if it is very strong, and otherwise only affect the crustal strength. Overall, the uncertainties in $\mu_{friction}$ and λ_{hpff} have less effect than uncertainties in T and $\dot{\epsilon}$.



(a) Mantle temperature decreased by 100°C



(b) Mantle temperature elevated by 100°C

Figure 7.13: Integrated strength of the lithosphere under compression with elevated or decreased mantle temperatures (using a linear temperature shift of $\pm 100^{\circ}\text{C}$ at the Moho interface and in the underlying mantle)

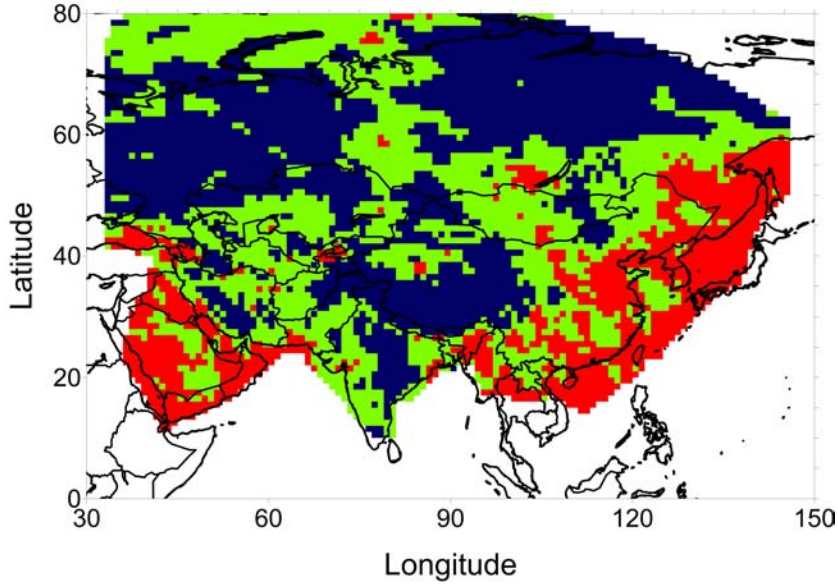


Figure 7.14: The Asian lithosphere classified into strong (red), weak (blue) and transition (green) lithosphere

Table 7.2: Integrated lithospheric strength [$\times 10^{12} Pam$] along a $(\sigma_1 - \sigma_3)$ -depth profile in the Urals under varying parameters

		$\mu_{friction} = 0.5$		$\mu_{friction} = 0.75$	
		$\lambda_{hpf} = 0.4$	$\lambda_{hpf} = 0.0$	$\lambda_{hpf} = 0.4$	$\lambda_{hpf} = 0.0$
$T + 100^\circ C$	$\dot{\epsilon} = 10^{-18} s^{-1}$	2.673	3.24	3.36	4.16
	$\dot{\epsilon} = 10^{-16} s^{-1}$	7.07	8.18	8.84	9.97
$T + 0^\circ C$	$\dot{\epsilon} = 10^{-18} s^{-1}$	11.05	14.59	15.54	20.28
	$\dot{\epsilon} = 10^{-16} s^{-1}$	23.37	29.62	31.18	40.33
$T - 100^\circ C$	$\dot{\epsilon} = 10^{-18} s^{-1}$	43.09	51.81	54.27	68.58
	$\dot{\epsilon} = 10^{-16} s^{-1}$	119.87	149.46	155.52	183.04

Table 7.3: Integrated crustal strength [$\times 10^{12} Pam$] along a $(\sigma_1 - \sigma_3)$ -depth profile in the Urals under varying parameters

		$\mu_{friction} = 0.5$		$\mu_{friction} = 0.75$	
		$\lambda_{hpf} = 0.4$	$\lambda_{hpf} = 0.0$	$\lambda_{hpf} = 0.4$	$\lambda_{hpf} = 0.0$
$T + 100^\circ C$	$\dot{\epsilon} = 10^{-18} s^{-1}$	2.24	2.81	2.93	3.73
	$\dot{\epsilon} = 10^{-16} s^{-1}$	5.40	6.51	6.82	8.30
$T + 0^\circ C$	$\dot{\epsilon} = 10^{-18} s^{-1}$	8.65	12.19	13.14	17.88
	$\dot{\epsilon} = 10^{-16} s^{-1}$	12.64	18.89	20.46	29.60
$T - 100^\circ C$	$\dot{\epsilon} = 10^{-18} s^{-1}$	15.76	24.48	26.93	41.24
	$\dot{\epsilon} = 10^{-16} s^{-1}$	19.72	30.60	33.38	51.72

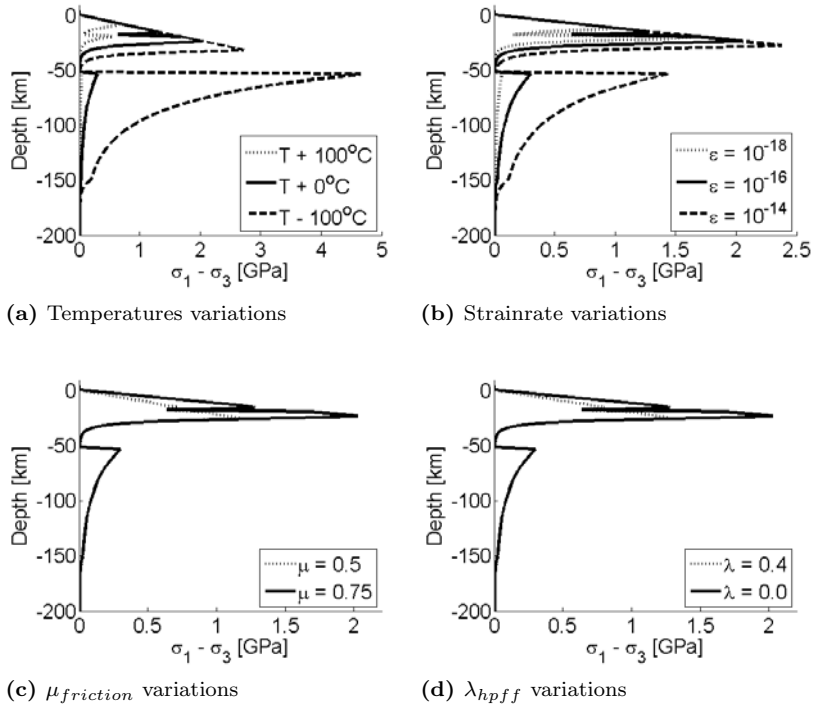


Figure 7.15: Sensitivity of lithospheric strength profiles in the Urals to variations in the parameters T , $\dot{\epsilon}$, λ_{hpff} , $\mu_{friction}$ (reference profile in black has $\dot{\epsilon} = 10^{-16} s^{-1}$, $\lambda_{hpff} = 0.0$, $\mu_{friction} = 0.4$ and T from chapter 6)

Table 7.4: Integrated lithospheric mantle strength [$\times 10^{12} Pam$] along a $(\sigma_1 - \sigma_3)$ -depth profile in the Urals under varying parameters

		$\mu_{friction} = 0.5$		$\mu_{friction} = 0.75$	
		$\lambda_{hpff} = 0.4$	$\lambda_{hpff} = 0.0$	$\lambda_{hpff} = 0.4$	$\lambda_{hpff} = 0.0$
$T + 100^\circ C$	$\dot{\epsilon} = 10^{-18} s^{-1}$	0.43	0.43	0.43	0.43
	$\dot{\epsilon} = 10^{-16} s^{-1}$	1.66	1.66	1.66	1.66
$T + 0^\circ C$	$\dot{\epsilon} = 10^{-18} s^{-1}$	2.40	2.40	2.40	2.40
	$\dot{\epsilon} = 10^{-16} s^{-1}$	10.72	10.72	10.72	10.72
$T - 100^\circ C$	$\dot{\epsilon} = 10^{-18} s^{-1}$	27.34	27.34	27.34	27.34
	$\dot{\epsilon} = 10^{-16} s^{-1}$	100.16	118.86	122.14	131.31

7.4 Future outlook

In the preceding paragraphs a first, tentative, assessment of the lithospheric strength in Asia has been presented. It was shown that temperature modelling plays a vital role in assessing lithospheric mantle strength. For certain transition zones (see figure 7.14) the accuracy of the temperature models, even using the new methodology presented in this thesis, is only sufficient for first order strength models. Future studies should therefore focus on further constraining temperatures in the lithospheric mantle, for example by further constraining the composition in 'hot areas' in the upper mantle. Also using all three dimensions of the earth's gravity gradient field measured by GOCE, whereas in this study only the principle (vertical) axis data was explicitly used, will lead to better models. Future missions like European Space Agency (ESA)'s Swarm mission [www.esa.int], measuring the Earth's magnetic field with unprecedented detail, as well as recent and ongoing developments in the field of seismology (such as ambient noise tomography, e.g. Wapenaar et al. [2011], Ruigrok and Wapenaar [2012], Wapenaar and Thorbecke [2013]) will provide additional input to determine composition and temperature in the lithosphere. Furthermore, in section 7.1.2 it is shown that strain-rate ($\dot{\epsilon}$) has a significant effect on the strength of the lithospheric mantle. Surface deformation studies, using e.g. GPS-measurements and/or InSAR data, could help to reduce the uncertainty in actual strain-rate, which is often not well constrained in current lithospheric strength models.

Intra-plate stress fields can also be significantly influenced by gravity-induced horizontal stresses that lead to ductile flow in the crust, the modelling of which also requires high resolution crustal thickness and density models [Tesauro et al., 2011]. Furthermore, assessment of dynamic topography (topography created by asthenospheric mantle processes such as mantle plumes and convection, e.g. Faccenna and Becker [2010]) also requires an accurate high resolution model of the crust [Boschi et al., 2010]. Improvement in the crustal models, such as the Moho-model and the crustal velocity model presented this thesis, can come through additional data, provided for instance by new field campaigns in sparsely covered areas like Arabia, India, the Tibetan region, Mongolia and the far east of Russia. Further progress can be made also by improving the modelling methodologies, such as including information on fault zones in the computation of large scale crustal models.

Data binning

A general way to fit a linear function to data is Least Squares (LS) estimation. In LS estimation, the sum of the squared residual misfit between a function and the data it has been fitted through is minimized. However, this does not mean that each misfit is minimized. For instance, if a cluster of data exists (many data points on a small interval), then the misfit of each data point in this cluster contributes to the total misfit. Thus an improved fit through the cluster can drastically lower the sum of squared misfits, even if the misfit of an single data point outside the cluster is significantly increased. In this case the cluster dominates the shape of the fitted function, and this is not always desirable. Data binning, which can be considered a method of weighing data, can be used to counter this effect. Basically, in data binning the relative weight of clusters is reduced in favour of single data points. Within this research, data binning is used both for determining the velocity-depth relationship in the sedimentary cover (function 3.3, section 3.1) and for determining the covariance models for OK (section 4.2 and appendix C).

In binning, original data values that fall within a given small interval, the bin, are replaced by a value representative of that interval. This so called replacement value is in this case the arithmetic mean of the original data values. The process of data binning is further explained in figure A.1. Without data binning, the original data (figure A.1a) are the observations through which function is fitted (figure A.1b). With data binning however, original data (figure A.1a) is first divided over depth bins of a certain width, 0.1km in this case (the horizontal red lines in figure A.1c). For each bin, the average value of the data (red dots in figure A.1c) is used as representative value. The function is then fitted through these representative values rather than through the original data (figure A.1d).

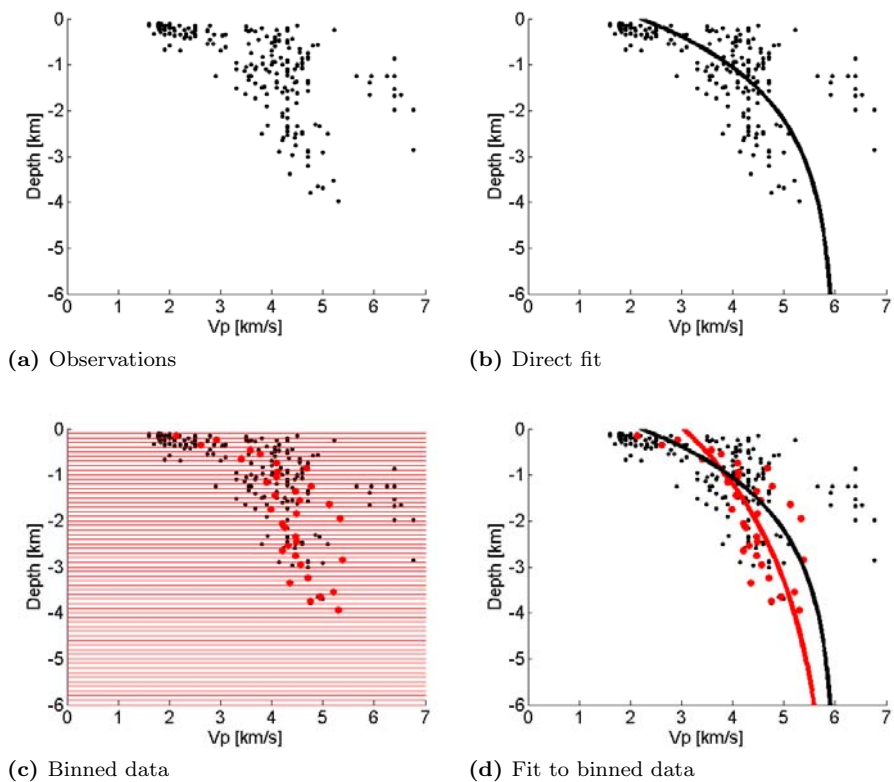


Figure A.1: The data binning method

Coefficient of determination

The coefficient of determination (R^2) is a measure of the quality of a fit, expressing how much of the variation of the data around the mean is explained by the fitted function. It is obtained by, subtracting from unity, the squared misfit around the fitted function (σ_{fit}^2) divided by the variance in the original data (σ_{data}^2), see equation B.1

$$R^2 = 1 - \frac{\sigma_{fit}^2}{\sigma_{data}^2} \quad (\text{B.1})$$

An R^2 of 1 implies that there is no misfit between the data and the fitted function, and thus that the function fully accounts for the variance in the data. An R^2 of 0 implies that the variance around the fitted function is as large as the variance in the original data. This in turn means that the mean of the data is just as good an explanation of the data as the fitted function. An R^2 of less than 0 means that the squared misfit is larger than the variance in the original data. This is impossible when strictly applying LS.

Some things should be remembered when working with coefficient of determination. The only thing R^2 does is express any residual misfit as a function of the variance in the original data. This means for example:

- R^2 measures the amount of variance explained by the fitted function, this is however, not a causal explanation.
- R^2 will be higher if the function fitted using LS has more regressors (degrees of freedom), thus it can not be used directly to compare two functions with a different amount of regressors.
- If there is only one data point, then the variance of the data is 0 (as is most likely the misfit around a fitted function) and R^2 can not be computed.
- If there are as many regressors in the fitted function as there are data, then the R^2 should come out at 1, however, this does not tell you anything about the quality of the fitted function. Adjusted R^2 attempts to take this into account.
- In a regression of a function of the form $y = ax + b$ where the regressor a turns out very small, R^2 will also be very small. Since $y = ax + b =$

b if $a \rightarrow 0$, the function $y = ax + b$ will almost be the same as a function for the mean (of the form $y = b$) for small a . As a consequence, variance around both the mean and the function will be almost the same, leading to an R^2 of almost 0. This does not mean that the regression is a bad one.

Ordinary Kriging

Ordinary Kriging (OK) is a powerful mathematical technique that can be used to interpolate data in an area with inhomogeneous data spreading, such as the depth to Moho or average V_p . OK is part of a group of geostatistical techniques called Kriging, named after Danie Gerhardus Krige. An extensive treatment of Kriging can be found in e.g Cressie [1993] or Wackernagel [1995]. This appendix briefly treats the principles of OK and focuses on its application in this research.

OK can be used to obtain an interpolated value $y(p_0)$ in a random field $Y(p)$. In this research the random field Y is depth to Moho (M) or the average V_p in the crust, and positions (p) are (lon, lat) pairs where an observation is available. The method is mathematically guaranteed to be a Best Linear Unbiased Estimator (BLUE).

In OK interpolations are obtained by **linearly** combining a finite number of nearby observations (i.e. $y(p_0) = \sum_{i=1}^n w_i y(p_i)$). By exploiting experimental covariances between the observations (see section C.2), the OK technique assigns weights, $[w_1, w_2, \dots, w_n]$ to observations $[y(p_1), y(p_2), \dots, y(p_n)]$, such that the error variance of the interpolation is minimized, resulting in the **best** estimate. The expectancy of the Kriging interpolation is the same as the expectancy of the observations (i.e. $\sum_{i=1}^n w_i = 1$), thus the estimate is **unbiased**.

C.1 Assumptions

Several assumptions are made with respect to the observations when using OK, of which the most important are:

- Wide sense stationarity
- Known (co)variogram
- Constant but unknown mean

The first two assumptions are implied by all varieties of Kriging, the third is specific to OK.

Wide sense stationarity implies that the mean and variance of the random field $Y(p)$ do not change in over time and position. When interpolating depth

to Moho or average V_p , it implies that both the mean and the variance should not change with a change in position of the interpolation point. In other words, the (co)variance between two observations should only depend on the distance between those locations, but not on their respective locations (i.e. neither the direction of the vector connecting the two observations nor the absolute locations of the observations). The observations in Asia are not stationary in the wide sense. However, by restricting the use of observations to those within a 10 degree radius of the interpolation location, wide sense stationarity is approximated.

The (co)variogram can only be properly known if enough observations exist and if the experimental (co)variances (see section C.2) regress well to the (co)variogram model used. For this reason, within this research, it has been determined that at least 11 observations are required to reliably estimate a (co)variance model (11 observations lead to 66 (co)variance-pairs).

A constant mean is part of the stationarity principle. However, OK does not require that this mean is known (as for instance Simple Kriging does).

C.2 Experimental covariogram and covariogram model

The covariogram model, or the covariance function lies at the base of any Kriging estimate. The covariance function shows how well observations are correlated in space and/or time and thus help determine both the optimal distribution of weights over the observations, as well as estimate the expected variance of the resulting estimated value.

Experimental covariance is the actual covariance in a finite set of observations ($[y(p_1), y(p_2), \dots, y(p_n)]$), i.e. the covariance is extracted from experience. The experimental covariance (cov) between two observations can be expressed as in C.1

$$\text{cov}(y(p_i), y(p_j)) = (y(p_i) - \bar{y})(y(p_j) - \bar{y}) \quad (\text{C.1})$$

with

$$\bar{y} = \frac{1}{n} \sum_{i=1}^n y(p_i) \quad (\text{C.2})$$

The experimental covariance can be computed for each pair of observations, including the covariance between an observation and itself ($\text{cov}(y(p_i), y(p_i))$). These covariances can be ordered according to the distance between the observations, $d(p_i, p_j)$. The result is an experimental covariogram, which after binning (see appendix A) looks like figure C.1.

An experimental covariance function ($\text{Cov}(d)$) can be fitted through the experimental covariances. This covariance function has to be positive definite in

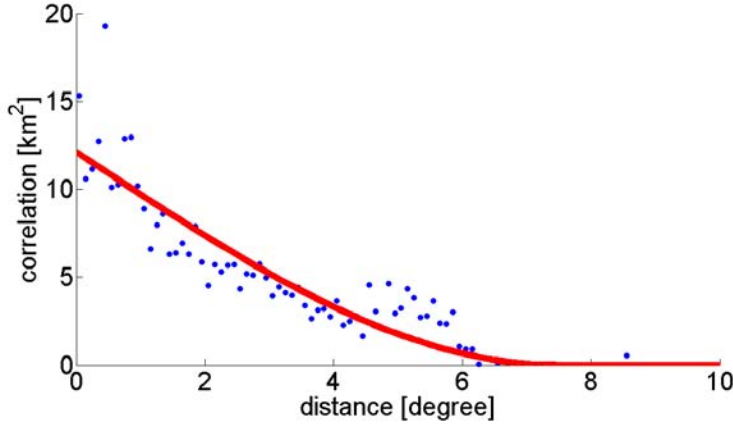


Figure C.1: Sample experimental covariogram (blue dots denote binned experimental covariances and the red line is the fitted covariance function)

order to be admissible to OK. Some admissible covariance functions are the exponential, gaussian and spherical covariance functions, given in equations C.3, C.4 and C.5 respectively.

$$\text{Cov}_{\text{expo}}(r) = c_0 e^{-\frac{3r}{c_{\text{range}}}} \quad (\text{C.3})$$

$$\text{Cov}_{\text{gauss}}(r) = c_0 e^{-\left(\frac{3r}{c_{\text{range}}}\right)^2} \quad (\text{C.4})$$

$$\text{Cov}_{\text{sph}}(r) = c_0 \left(1 - \frac{3r}{2c_{\text{range}}} + \frac{r^3}{2c_{\text{range}}^3} \right) \quad (\text{C.5})$$

These covariance functions are controlled by two parameters. The first, c_0 , is the variance of the used observations around their mean (equation C.6). The second, c_{range} , defines the distance at which the covariance approximates 0.

$$\begin{aligned} \text{Cov}(0) &= \frac{1}{n} \sum_{i=1}^n (y(p_i) - \bar{y})(y(p_i) - \bar{y}) \\ &= \frac{1}{n} \sum_{i=1}^n (y(p_i) - \bar{y})^2 \\ &= \text{var}(Y(p)) \end{aligned} \quad (\text{C.6})$$

Different covariance functions have different smoothness properties, influencing the smoothness of the final interpolation. In this research, both for the depth Moho and the average V_p interpolation, a spherical covariance function (Cov_{sph}) was chosen, since this leads to the smoothest estimation.

C.3 The Ordinary Kriging scheme

Once a proper covariance function has been obtained, the OK can start. The OK-scheme consists of three steps:

- Determine variance-covariance matrix and proximity vector
- Determine Kriging weights for observations
- Estimate value at required location

The variance-covariance-matrix (C_n) is constructed first (equation C.7). The covariance (C_{ij}) between two observations i and j is determined by evaluating the covariance function, $\text{Cov}(d)$ for d_{ij} , the distance between the two observations. Similarly, the expected covariance between the observations and the estimated value (C_{i0}) is determined by evaluating the covariance function for the distance d_{i0} between observation i and the evaluation point (0). These expected covariances are then stored in the proximity vector, D_n (equation C.8).

$$C_n = \begin{pmatrix} C_{11} & \dots & C_{1n} \\ \vdots & \ddots & \vdots \\ C_{n1} & \dots & C_{nn} \end{pmatrix} \quad (\text{C.7})$$

$$D_n = \begin{pmatrix} C_{10} \\ \vdots \\ C_{n0} \end{pmatrix} \quad (\text{C.8})$$

The weight matrix (W_n) can be determined by expanding the variance-covariance-matrix and the proximity vector to include the Lagrange multiplier (λ) (equation C.9).

$$\begin{pmatrix} w_1 \\ \vdots \\ w_n \\ \lambda \end{pmatrix} = \begin{pmatrix} C_{11} & \dots & C_{1n} & 1 \\ \vdots & \ddots & \vdots & \vdots \\ C_{n1} & \dots & C_{nn} & 1 \\ 1 & \dots & 1 & 0 \end{pmatrix}^{-1} \begin{pmatrix} C_{10} \\ \vdots \\ C_{n0} \\ 1 \end{pmatrix} \quad (\text{C.9})$$

The estimation of the value y at p_0 can now be computed by linearly combining the weights and observations, equation C.10.

$$y(p_0) = \sum_{i=1}^n w_i y(p_i) \quad (\text{C.10})$$

A large advantage of OK is that the variance of the estimate (i.e. expected uncertainty of the answer) can easily be estimated, based on the variance in the data in combination with the weight and proximity vectors, using equation C.11:

$$\text{Var}(y(p_0)) = C_{11} - (W_n' D_n + \lambda) \quad (\text{C.11})$$

C.4 Considerations on the use of Ordinary Kriging

OK, like any mathematical technique, has its limitations. The three most important points to consider when using OK are listed below.

Better non-linear or biased methods. While OK has been proven to be BLUE, there could exist biased and/or non-linear techniques that give a better solution to the problem at hand than OK.

Variogram needs to be accurate. The properties best and unbiased hold only on the premise that the right (co)variance function is used. If the (co)variance function is inaccurate, these properties are lost, but the interpolation is generally still good.

Little or no spatial dependence lead to estimating the mean. When the interpolation point is far away from observations - far being defined as c_{range} being greater or equal to the distance to the nearest observations - no correlation between the interpolation point and the observations is inferred. The interpolated value will then simply become the average of the used observations and the variance will be the variance of the data (c_0). When interpolating the depth to Moho (chapter 4) far away from available observations, the residual depth to Moho (section 4.2) will become the average residual depth to Moho for that area. When topographic adjustment is restored (section 4.3), the restored depth to Moho will just reflect topography. However, since these areas also show the largest expected uncertainty (equation C.11), this is not deemed problematic.

Nomenclature

- α thermal expansion coefficient, in g/cm^3K . 66
- $\alpha_{byerlee}$ Byerlee coefficient, dependend on the (static) sliding friction coefficient and type of faulting. 95
- ΔV_{ml} pressure wave velocity increase between middle and lower crust, in km/s . 49, 50, 52
- ΔV_{um} pressure wave velocity increase between upper and middle crust, in km/s . 49, 50, 52
- ϵ strain. 68, 69
- $\dot{\epsilon}$ strainrate, in s^{-1} . 95–98, 104, 107, 109–111
- κ bulk modulus, in Pa . 63–66, 70, 71, 125
- κ_0 bulk modulus at surface conditions ($T = 293K$ and $P = 0GPa$), in Pa . 65–67
- λ Lagrange multiplier, in OK. 120
- λ_{hpf} hydrostatic pore fluid factor, in Byerlee’s law. 95, 96, 104, 107, 109, 110
- λ_{vol} volume fraction of constituent mineral in composite. 70
- λ_{wave} wavelength on a sphere, in km . 14
- μ shear modulus, in Pa . 63–66, 70, 71, 125
- μ_0 shear modulus at surface conditions ($T = 293K$ and $P = 0GPa$), in Pa . 65–67
- $\mu_{friction}$ (static) friction coefficient (used in Byerlee’s law). 95, 96, 104, 107, 109, 110
- ρ density, in g/cm^3 . 22, 25, 58, 63–66, 68, 71, 72, 76, 81, 95
- ρ_0 density at surface conditions ($T = 293K$ and $P = 0GPa$), in g/cm^3 . 65–67
- $\rho_{lowercrust}$ average density of the lower crust, taken as $2.85g/cm^3$. 37
- ρ_{mantle} average density of the mantle, taken as $3.32g/cm^3$. 37
- ρ_{sed} average density of sedimentary column, in g/cm^3 . 37

- $\rho_{uppercrust}$ average density of the upper crust, taken as $2.67g/cm^3$. 37
- ρ_{water} average density of the salt water, taken as $1.00g/cm^3$. 37
- σ stress in *MPa*. 93
- σ_{std} standard deviation or square root of the variance, same unit as physical quantity it is the standard deviation of. 38, 40, 44, 50, 51, 53
- σ_{data} square root of variance of data around the mean, same unit as data. 115
- σ_{fit} square root of squared residual misfit between data and function, unit is the same as data it is applied to. 50, 51, 115
- ψ Green's function in gravitational attraction. 72, 73
- ω seismic frequency, in *Hz*. 71
- A* normalization factor used in anelastic correction of anharmonic velocities. 71
- a* frequency dependence of the attenuation. 71
- A_p Power law constant [$Pa^{-n}s^{-1}$]. 95, 96
- c_0 covariance at distance $d = 0$, used as parameter in spherical covariance model, unit is same as Cov it relates to. 38, 119, 121
- c_{anel} Anelastic correction factor to wave velocity. 63, 70
- C_{ij} covariance between two observations i and j , based on covariance function (Cov). 120
- C_n variance-covariance matrix of size $n \times n$. 120
- c_{range} distance at which the covariance becomes $cov = 0$, used as parameter in spherical covariance model, unit is same as d . 38, 119, 121
- Cov** positive definite covariance model, as function of distance d fitted to experimental covariances. Units are the square of the unit of the observations to which they relate. 38, 118–120, 124
- cov** experimental covariance as a function of distance (d) between observations. Units are the square of the unit of the observations to which they relate. 38, 118
- d distance between two observations, in $^\circ$. 38, 50, 118, 120, 124
- D_n proximity vector of size $n \times 1$. 120
- E_p Activation energy used in power law creep [J/mol]. 95, 96
- Fe* Iron content in composition (value between 0 and 1). 82–84

- G Gravitational constant, $6.67384 \times 10^{-8} \text{m}^3/\text{kg}\text{s}^2$. 72
- g Gravitational acceleration, in m/s^2 . 72, 95
- g_{temp} Homologous temperature scaling. 71
- h topography, in km , positive axis upward. 37, 107
- h_{adj} adjusted topography, in km , positive axis upward. 37
- K_{gain} Gain factor (P-controller). 83
- M depth to Moho, in km from mean sea level. 38, 117
- M_{obs} observed depth to Moho, in km from mean sea level. 12, 13, 36, 37
- M_{res} residual depth to Moho, in km from mean sea level. 37, 38
- M_w wave modulus, in GPa ($M_w = \kappa + \frac{4}{3}\mu$ for pressure waves and $M_w = \mu$ for shear waves. 68, 69
- n value of the power in the power law [Kirby, 1983], determined empirically. 95, 96
- n_{obs} number of observations. 28
- P pressure in Pa . 64, 65, 95, 123
- p position. 117, 118, 120, 126
- P_0 surface pressure, OPa . 66–68
- Q wave attenuation factor. 70, 71
- Q_κ bulk attenuation factor. 71
- Q_μ rigidity attenuation factor. 70, 71
- R radius on a sphere, in $^\circ$. 38
- r linear distance between to points. 72
- R_{max} maximum search radius on a sphere, in $^\circ$. 50
- R^2 measure of how much of the data is explained by the fitted function. 26, 28, 56, 115, 116
- T temperature in K . 64–66, 71, 95, 104, 107, 109, 110, 123
- T_0 surface temperature, 293K . 66, 67
- t_{crust} thickness of the crust, from basement to Moho, in km . 46

- t_{layer} thickness of a crustal layer, in km . 13
- t_{lower}^{rel} relative thickness of lower crust. 56
- T_{melt} melt temperature of minerals, at depth. 71
- t_{middle}^{rel} relative thickness of middle crust. 56
- t_{sed} thickness of sedimentary layer, in km . 37
- t_{upper}^{rel} relative thickness of upper crust. 56
- t_{water} depth of water layer, in km . 37
- U Gravitational potential, in m^2/s^2 . 72
- V velocity, in km/s . 12, 13, 26, 49–51
- v volume, in m^3 , used in section 6.2. 72
- V_{anh} anharmonic wave velocity, in km/s . 63
- V_{lower} pressure wave velocity in the lower crust, in km/s . 56, 57
- V_{max} maximum velocity in sedimentary layer, in km/s . 26, 28
- V_{middle} pressure wave velocity in the middle crust, in km/s . 56, 57
- V_{obs} observed wave velocity, in km/s . 64, 65, 71
- V_p pressure wave velocity, in km/s . 13, 25, 26, 32, 36, 58, 64, 117–119
- V_s shear wave velocity, in km/s . 13, 14, 64, 79, 81
- V_{surf} seismic velocity at the surface, in km/s . 26, 28
- V_{syn} synthetic wave velocity, in km/s . 64, 65
- V_{upper} pressure wave velocity in the upper crust, in km/s . 49, 50, 52, 56, 57
- W weight given to an observation. 50
- W_n weight matrix used in Ordinary Kriging. 120
- X composition of lithospheric mantle. 64
- Y random function. 117, 126
- y sample outcomes at location p_i of random variables $Y(p_i)$. 117, 118, 120
- z depth from mean sealevel, in km . 12, 13, 26, 49–51, 53, 95
- z_{ml} depth to boundary between middle and lower, in km . 49–52

\bar{z} normalized depth (0 at basement and 1 at Moho). 49

z_{top} depth to the top of a layer, in *km*. 13

z_{um} depth to boundary between upper and middle crust, in *km*. 49–52

$z_{V_{max}}$ indicates how fast the wave velocity approaches V_{max} in sediments, in *km*. 26, 28

About the author

Ward Stolk was born on the 20th of February 1985. He attended primary school De Wegwijzer before obtaining a Gymnasium-diploma at Corderius College in 2003. It was at this high school that his interest in science and philosophy developed, and with his final science project he earned, together with Adriaan Kleinhout, first prize in the physics section of the 10th International Conference for Young Scientists (ICYS). Ward continued his education studying Aerospace Engineering at Delft University of Technology, earning his Bachelor of Science degree in 2006. His master specialisation in Earth Observation brought him to internships at the GeoForschungsZentrum (GFZ) Potsdam and the geomatics department of the University of Calgary. In 2009 he obtained his Master of Science degree with honours, on a master thesis titled: 'An evaluation of the use of radial basis functions for mass change estimates at high latitudes'. Also in 2009 he obtained a Bachelor of Arts degree in Philosophy from the VU University in Amsterdam.

Through his internship at GFZ he landed a PhD-position at Sierd Cloetingh's group of Tectonics at the VU University. During his PhD-research he presented at several conferences, including EGU, AGU, IUGG and IGC. Furthermore he was invited to give lectures at a workshop 'Geophysical Characteristics and Modelling of the Lithosphere' at the China University of Geosciences in Wuhan, in the summer of 2011. In 2012 he moved with the Tectonics research group to Utrecht University, where he defends this thesis on September 9, 2013.

Bibliography

- J.C. Afonso, M. Fernàndez, G. Ranalli, W.L. Griffin, and J.A.D. Connolly. Integrated geophysical-petrological modeling of the lithosphere and sublithospheric upper mantle: Methodology and applications. *Geochemistry Geophysics Geosystems*, 9(5), 2008.
- K. Al Hosani, F. Roure, R. Ellison, and S. Lokier, editors. *Lithosphere Dynamics and Sedimentary Basins: The Arabian Plate and Analogues*. Springer, 2013. ISBN 978-3-642-30609-9, 474pp.
- C. Amante and B.W. Eakins. ETOPO1 1 Arc-Minute Global Relief Model: Procedures, Data Sources and Analysis. Technical report, NOAA Technical Memorandum NESDIS NGDC-24, 2009.
- I.M. Artemieva. The continental lithosphere: Reconciling thermal, seismic and petrological data. *Lithos*, 109:23–46, 2009.
- I.M. Artemieva. *The Lithosphere; An Interdisciplinary Approach*. Cambridge University Press, Cambridge, UK, 2011. 773pp.
- I.M. Artemieva and W.D. Mooney. Thermal thickness and evolution of Precambrian lithosphere: A global study. *Journal of Geophysical Research*, 106(8): 16,387–16,414, 2001.
- M.E. Artemjev and M.K. Kaban. Density inhomogeneities, isostasy and flexural rigidity of the lithosphere in the Transcaspien region. *Tectonophysics*, 240: 281–297, 1994.
- M.E. Artemjev, M.K. Kaban, V.A. Kucherinenko, G.V. Demjanov, and V.A. Taranov. Subcrustal density inhomogeneities of Northern Eurasia as derived from the gravity data and isostatic models of the lithosphere. *Tectonophysics*, 240:249–280, 1994.
- C. Ayala, G.S. Kimbell, D. Brown, P. Ayarza, and Y.P. Menshikov. Magnetic evidence for the geometry and evolution of the eastern margin of the East European Craton in the Southern Urals. *Tectonophysics*, 320:31–44, 2000.
- C. Bassin, G. Laske, and G. Masters. The current limites of resolution for surface wave tomography in North America. *EOS Trans AGU*, 81(F897), 2000.
- F. Beekman. *Tectonic modelling of thick-skinned compressional intraplate deformation*. PhD thesis, Vrije Universiteit Amsterdam, 1994. ISBN = 90-9007426-0.

BIBLIOGRAPHY

- V.V. Belousov, N.I. Pavlenkova, and Kvyatkovskaya G.N. *Deep structure of the USSR territory*. Publishing House Nauka, Moscow, 1991. in Russian.
- R.J. Blakely. *Potential Theory in Gravity & Magnetic Applications*. Cambridge University Press, 1995. 441pp.
- L. Boschi, C. Facenna, and T.W. Becker. Mantle structure and dynamic topography in the Mediterranean Basin. *Geophysical Research Letters*, 37:L20303, 2010.
- T.M. Brocher. Compressional and Shear Wave Velocity Versus Depth in the San Francisco Bay Area, California: Rules for USGS Bay Area Velocity Model 05.0.0. Technical report, U.S. Geological Survey, 2005. Open-File Report 05-1317.
- D. Brown. The growth and destruction of continental crust during arc-continent collision in the Southern Urals. *Tectonophysics*, 433:39–51, 2009.
- D. Brown, C. Juhlin, A. Tryggvason, D. Steer, P. Ayarza, M. Beckholmen, A. Rybalka, and Bliznetsov M. The Crustal Architecture of the Southern and Middle Urals From the URSEIS, ESRU and Alapaev Reflection Seismic Surveys. In D. Brown, C. Juhlin, and V. Puchkov, editors, *Mountain Building in the Urals; Pangea to Present*, volume 132 of *Geophysical Monograph Series*, pages 33–48. American Geophysical Union, Washington, 2002.
- D. Brown, V. Puchkov, J. Alvarez-Marron, F. Bea, and A. Perez-Estaun. Tectonic processes in the South and Middle Uralides: An overview. In D. Gee and R. Stephenson, editors, *European Lithosphere Dynamics*, pages 409–419. Geological Society Memoir, 2006.
- M-F. Brunet, Y.A. Volozh, M.P. Antipov, and L.I. Lobkovsky. The geodynamic evolution of the Precaspian Basin (Kazakhstan) along a north-south section. *Tectonophysics*, 313:85–106, 1999.
- M.-F. Brunet, M.V. Korotaev, A.V. Ershov, and A.M. Nikishin. The South Caspian basin: a review of its evolution from subsidence modelling. *Sedimentary Geology*, 156:119–148, 2003.
- E. Burov. Rheology and strength of the lithosphere. *Marine and Petroleum Geology*, 28:1402–1443, 2011.
- E.B. Burov and A.B. Watts. The long-term strength of continental lithosphere: "jelly sandwich" or "crème brûlée"? *GSA Today*, 16(1):4–10, 2006.
- E.B. Burov, L.I. Lobkovsky, S. Cloetingh, and A.M. Nikishin. Continental lithosphere folding in Central Asia (Part II): constraints from gravity and topography. *Tectonophysics*, 226:73–87, 1993.
- J. Byerlee. Friction of Rocks. *Pure and Applied Geophysics*, 116(4-5):615–626, 1978.

- F. Cammarano, S. Goes, P. Vacher, and D. Giardini. Inferring upper-mantle temperatures from seismic velocities. *Physics of the Earth and Planetary Interiors*, 138:197–222, 2003.
- N.L. Carter and M.C. Tsenn. Flow properties of continental lithosphere. *Tectonophysics*, 136:27–63, 1987.
- D.S. Chapman. Thermal gradients in the continental crust. In J.B. Dawson, editor, *The Nature of the Lower Continental Crust*, volume 24 of *Special Publications*, pages 63–70. Geological Society, London, 1986.
- N.I. Christensen and W.D. Mooney. Seismic velocity structure and composition of the continental crust: A global view. *Journal of Geophysical Research*, 100 (B7):9761–9788, 1995.
- D-H. Chung. Elastic moduli of single crystal and polycrystalline MgO. *Philosophical Magazine*, 8(89):833–841, 1963.
- S. Cloetingh and E. Banda. Mechanical structure. In D. Blundell, S. Mueller, and R. Friedman, editors, *The European Geotraverse; A continent revealed*, chapter 4.2, pages 80–91. Cambridge University Press, 1992.
- S. Cloetingh and E.B. Burov. Thermomechanical structure of European continental lithosphere: constraints from rheological profiles and EET estimates. *Geophysical Journal International*, 124:695–723, 1996.
- S. Cloetingh and E.B. Burov. Lithospheric folding and sedimentary basin evolution: a review and analysis of formation mechanisms. *Basin Research*, 23: 257–290, 2011.
- S. Cloetingh, E. Burov, and A. Poliakov. Lithosphere folding: Primary response to compression? (from central Asia to Paris basin). *Tectonics*, 18(6):1064–1083, 1999.
- S. Cloetingh, E.B. Burov, F. Beekman, B. Andeweg, P.A.M. Andriessen, D. Garcias-Castellanos, G. De Vicente, and R. Vegas. Lithospheric folding in Iberia. *Tectonics*, 21:1041, 2002.
- S. Cloetingh, P.A. Ziegler, F. Beekman, P.A.M. Andriessen, L. Matenco, G. Bada, D. D. Garcia-Castellanos, N. Hardebol, P. Dèzes, and D. Sokoutis. Lithospheric memory, state of stress and rheology: neotectonic controls on Europe’s intraplate continental topography. *Quaternary Science Reviews*, 24 (3-4):241–301, 2005.
- S. Cloetingh, F. Beekman, P.A. Ziegler, J-D. van Wees, and D. Sokoutis. Post-rift compressional reactivation potential of passive margins and extensional basins. *Geological Society London, Special Publications*, 306:27–70, 2008.
- N. Cressie. *Statistics for spatial data*. Wiley, New York, 1993. 928pp.

BIBLIOGRAPHY

- G.F. Davies and A.M. Dziewonsky. Homogeneity and constitution of the earth's lower mantle and outer core. *Physics of the Earth and Planetary Interiors*, 10:336–343, 1975.
- D. Delvaux, R. Moeys, G. Stapel, C. Petit, K. Levi, A. Miroshnichenko, V. Ruzhich, and V. San'kov. Paleostress reconstructions and geodynamics of the Baikal region, Central Asia, Part2. Cenezoic rifting. *Tectonophysics*, 282:1–38, 1997.
- D. Delvaux, S. Cloetingh, F. Beekman, D. Sokoutis, E. Burov, M. Kaban, M.M. Buslov, and K.E. Abdrakhmatov. Basin evolution in a folding lithosphere: Examples from the Altai-Sayan and Tien Shan belts. *Tectonophysics*, 2013. in press.
- D.L. Divins. Total Sediment Thickness of the World's Oceans & Marginal Seas. Technical report, NOAA NGDC, 'Boulder, CO, 2003.
- T.S. Duffy and D.L. Anderson. Seismic velocities in mantle minerals the mineralogy of the upper mantle. *Journal of Geophysical Research*, 94(B2):1895–1912, 1989.
- A.M. Dziewonski and D.L. Anderson. Preliminary reference Earth model. *Physics of the Earth and Planetary Interior*, 25:297–356, 1981.
- S.S. Egan, J. Mosar, M.-F. Brunet, and T. Kangarli. Subsidence and uplift mechanisms within the South Caspian Basin: insights from the onshore and offshore Azerbaijan region. *Geological Society Special Publication*, 312:219–240, 2009.
- A.V. Egorkin. Crustal structure from seismic long-profiles. In V.V. Belousov, editor, *Deep Structure of the Territory of the USSR*, pages 118–134. Nauka, Moscow, 1991.
- A.V. Egorkin. Velocity structure, composition and discrimination of crustal provinces in the former Soviet Union. *Tectonophysics*, 298(4):395–404, 1998.
- A.V. Ershov, M.-F. Brunet, A.M. Nikishin, S.N. Bolotov, B.P. Nazarevich, and M.V. Korotaev. Northern Caucasus basin: thermal history and synthesis of subsidence models. *Sedimentary Geology*, 156:95–118, 2003.
- Production Research Company Exxon. Tectonic map of the world. Technical report, American Association of Petroleum Geologists Foundation, Tulsa, OK, 1985.
- C. Faccenna and T.W. Becker. Shaping mobile belts by small-scale convection. *Nature*, 465:602–605, 2010.
- Y. Fei. *Mineral physics and crystallography, a handbook of physical constants*, chapter Thermal expansion, pages 29–44. AGU references shelf 2. American Geophysical Union, 1995.

- R. Forsberg and C. Tscherning. Topographic effects in gravity modelling for BVP. In F. Sansfio and R. Rummel, editors, *Geodetic Boundary Value Problems in View of the One Centimeter Geoid*, number 65 in Lecture Notes in Earth Sciences, pages 241–272. Springer, Berlin - Heidelberg - New York, 1997.
- C. Förste, S. Bruinsma, R. Shako, J.-C. Marty, F. Flechtner, O. Abrikosov, C. Dahle, J.-M. Lemoine, K.H. Neumayer, R. Biancale, F. Barthelmes, R. König, and G. Balmino. EIGEN-6 - A new combined global gravity field model including GOCE data from the collaboration of GFZ-Potsdam and GRGS-Toulouse. In *Geophysical Research Abstracts*, volume 13, 2011. EGU2011-3242-2, EGU General Assembly.
- T. François, E Burov, B. Meyer, and P. Agard. Surface topography as key constraint on thermo-rheological structure of stable cratons. *Tectonophysics*, 2013. in press.
- S. Gac, R.S. Huismans, Y.Y. Podlachikov, and J.I. Faleide. On the origin of the ultradeep East Barents Sea basin. *Journal of Geophysical Research*, 117: B0440, 2012.
- G.H.F. Gardner, L.W. Gardner, and A.R. Gregory. Formation velocity and density - The diagnostic basics for stratigraphic traps. *Geophysics*, 39:770–780, 1984.
- GEON. Unpublished report of DSS profiles in the former Soviet Union. Centre of Regional Geophysical and Geoecological (Russian Ministry of Geology), 1989.
- GEON. Unpublished report of DSS profiles in the former Soviet Union. Centre of Regional Geophysical and Geoecological (Russian Ministry of Geology), 1992.
- S. Goes, R. Govers, and P. Vacher. Shallow mantle temperatures under Europe from P and S wave tomography. *Journal of Geophysical Research*, 105(B5): 11,153 – 11,169, May 2000.
- C. Goetze and B. Evans. Stress and temperature in the bending lithosphere as constrained by experimental rock mechanics. *Geophysical Journal of the Royal Astronomical Society*, 59:463–478, 1979.
- W. L. Griffin, Z. Andi, S. Y. O'Reilly, and C. G. Ryan. Phanerozoic evolution of the lithosphere beneath the Sino-Korean craton. In M.F.J. Flower, S-L. Chung, C-H. Lo, and T-Y. Lee, editors, *Mantle Dynamics and Plate Interactions in East Asia*, volume 27 of *Geodynamic Series*, pages 107–126. American Geophysical Union, 1998.
- W.L. Griffin, C.G. Ryan, F.V. Kaminsky, S.Y. O'Reilly, L.M. Natapov, T.T. Win, P.D. Kinny, and I.P. Ilupin. The Siberian lithosphere traverse: mantle terranes and the assembly of the Siberian Craton. *Tectonophysics*, 310:1–35, 1999.
- W.L. Griffin, S.Y. O'Reilly, N. Abe, S. Aulbach, R.M. Davies, N.J. Pearson, B.J. Doyle, and K. Kivi. The origin and evolution of archean lithospheric mantle. *Precambrian Research*, 127:19–41, 2003.

BIBLIOGRAPHY

- B. Guest, A. Guest, and G. Axen. Late Tertiary tectonic evolution of northern Iran: a case for simple crustal folding. *Global Planetary Change*, 58:435–453, 2007.
- M.R. Handy and J-P. Brun. Seismicity, structure and strength of the continental lithosphere. *Earth and Planetary Science Letters*, 223:427–441, 2004.
- O. Heidbach, M. Tingay, A. Barth, J. Reinecker, D. Kurfess, and B. Müller. The World Stress Map database release 2008, 2008. doi:10.1594/GFZ.WSM.Rel2008.
- R. Hill. The Elastic Behaviour of a Crystalline Aggregate. *Proceedings of the Physical Society, Section A*, 65(5):349–354, 1952.
- M.M. Hirschmann. Mantle solidus: Experimental constraints and the effects of peridotite composition. *Geochemistry, Geophysics, Geosystems*, 1, 2000.
- International Seismological Centre. International Seismological Centre On-line Bulletin, 2011. <http://www.isc.ac.uk>.
- R.C. Jachens and B.C. Moring. Maps of the thickness of Cenozoic deposits and the isostatic residual gravity over basement for Nevada. Technical report, U.S. Geological Survey, 1990. Open-File Report 90-404, 15p.
- H.R. Jackson. Arctic refraction catalogue. Technical report, Geological Survey of Canada, 2002a. URL <http://www.nrcan.gc.ca/earth-sciences/products-services/geoscience-data-repository/11818>.
- I. Jackson, M.S. Paterson, and J.D. Fitz Gerald. Seismic wave dispersion and attenuation in heim dunite: an experimental study. *Geophysical Journal International*, 108:517 – 534, 1992.
- J. Jackson. Strength of the continental lithosphere: Time to abandon the jelly sandwich? *GSA Today*, September 2002b.
- S. Ji and J. Martignole. Ductility of garnet as an indicator of extremely high temperature deformation. *Journal of Structural Geology*, 16(7):985–996, 1994.
- T.H. Jordan. Mineralogies, densities and seismic velocities of garnet lherzolites and their geophysical implications. In F.R. Boyd and H.O.A. Myer, editors, *The Mantle Sample, Inclusions in Kimberlites and Other Volcanics*, pages 1–14. American Geophysical Union, Washington D.C., 1979.
- M. Kaban. A gravity model of the north eurasia crust and upper mantle: 1. mantle and isostatic residual gravity anomalies. *Russian Journal of Earth Sciences*, 3(2):143–163, 2001. (Maintained and distributed by AGU, <http://www.agu.org/wps/rjes/>).
- M. Kaban, W. Stolk, F. Beekman, and S. Cloetingh. Density structure of the crust and upper mantle of Asia. In *International Symposium on Gravity, Geoid and Height Systems GGHS, October 9-12, 2012, Venice, Italy*, 2012. (S7-038).

- M. K. Kaban, P. Schwintzer, and C. Reigber. A new isostatic model of the lithosphere and gravity field. *Journal of Geodesy*, 78(6):368–385, 2004.
- M.K. Kaban. Estimation of the effect of distant zones in gravity modeling of the lithosphere. In *EGU General Assembly, Vienna, 13 - 18 April 2008, Geophysical Research Abstracts*, volume 10, 2008. A-05174.
- M.K. Kaban and W.D. Mooney. Density structure of the lithosphere in the southwestern United States and its tectonic significance. *Journal of Geophysical Research*, 106(B1):721–739, 2001.
- M.K. Kaban, M.E. Artemjev, A.I. Karaev, and A.P. Belov. The deep structure and geodynamics of the tectonic features in Turkmenistan and adjacent areas; gravity evidence. *Geotectonics*, 32(4):323–332, 1998.
- M.K. Kaban, P. Schwintzer, I.M. Artemieva, and W.D. Mooney. Density of the continental roots: compositional and thermal contributions. *Earth and Planetary Science Letters*, 209:53–69, 2003.
- M.K. Kaban, I. Rogozhina, A. Baranov, V. Trubitsyn, and M. Rothacher. First steps toward a comprehensive snap-shot model of the dynamic solid Earth. In *EGU General Assembly, Vienna, 19 - 24 April 2009, Geophysical Research Abstracts*, volume 11, 2009. EGU2009-2533.
- M.K. Kaban, M. Tesauro, and S. Cloetingh. An integrated gravity model for Europe’s crust and upper mantle. *Earth and Planetary Science Letters*, 296:195–209, 2010.
- S. Karato. Importance of anelasticity in the interpretation of seismic tomography. *Geophysical Research Letters*, 20:1623–1626, 1993.
- N.I. Khalevin, V.V. Kolmogorova, and F.F. Yunusov. The crust and the upper mantle at the axial zone of the Ural Mountains from multiwave seismic data. *Physics of the Solid Earth*, 23(7):535–544, 1987.
- S.H. Kirby. Rheology of the lithosphere. *Reviews of geophysics and space physics*, 21(6):1458–1487, 1983.
- I. Koulakov. High-frequency P and S velocity anomalies in the upper mantle beneath Asia from inversion of worldwide traveltime data. *Journal of Geophysical Research: Solid Earth*, 116(B4):301, 2011.
- C. Kreemer, A.J. Haines, W.E. Holt, G. Blewitt, and D. Lavalée. On the determination of a global strain rate model. *Earth Planets Space*, 52:765–770, 2000.
- C. Kreemer, W.E. Holt, and A.J. Haines. An integrated global model of present-day plate motions and plate boundary deformation. *Geophysical Journal International*, 154:8–34, 2003.

BIBLIOGRAPHY

- V.E. Langenheim and R.C. Jachens. Thickness of Cenozoic deposits and ground-water storage capacity of the westernmost part of the Las Vegas Valley, Nevada, inferred from gravity data. Technical report, U.S. Geological Survey, 1996. Open-File Report 96-259, 29p.
- K.M. Larson, R. Bürgmann, R. Bilham, and J.T. Freymeuller. Kinematics of the India-Eurasia collision zone from GPS measurements. *Journal of Geophysical Research*, 104(B1):1077–1093, 1999.
- G. Laske and G. Masters. A Global Digital Map of Sediment Thickness. *EOS Transactions AGU*, 78:F483, 1997.
- S. Li, W.D. Mooney, and J. Fan. Crustal structure of mainland China from deep seismic sounding data. *Tectonophysics*, 420:239–252, 2006.
- M. Liu, W.D. Mooney, S. Li, N. Okaya, and S. Detweiler. Crustal structure of the northeastern margin of the Tibetan plateau from Songpan-Ganzi terrane to the Ordos basin. *Tectonophysics*, 420:253–266, 2006.
- N.A. Logatchev and N.A. Florensov. The Baikal system of rift valleys. *Tectonophysics*, 45:1–13, 1978.
- W.J. Ludwig, J.E. Nafe, and C.L. Drake. Seismic refraction. In A.E. Maxwell, editor, *The Sea*, volume 4, pages 53–84. Wiley-Interscience, New York, 1970.
- A. Maggi, J.A. Jackson, D. McKenzie, and Priestley K. Earthquake focal depths, effective elastic thickness, and the strength of the continental lithosphere. *Geology*, 28:495–498, 2000.
- W.F. McDonough. Constraints on the composition of the continental lithospheric mantle. *Earth and Planetary Science Letters*, 101:1–18, 1990.
- N. Minorsky. Directional stability of automatically steered bodies. *Journal of the American Society for Naval Engineers*, 34:280–309, 1922.
- P. Molnar and P. Tapponnier. Cenezoic tectonics of asia: Effects of a continental collision. *Science*, 189(4201):419–426, 1975.
- W.D. Mooney. Crust and lithospheric structure - Global crustal structure. In B. Romanowicz, A. Dziewonski, and G. Schubert, editors, *Treatise on Geophysics*, volume 1, pages 361–417. Elsevier, Amsterdam, 2007.
- W.D. Mooney and M.K. Kaban. The North American upper mantle: Density, composition, and evolution. *Journal of Geophysical Research*, 115:B12424, 2010.
- W.D. Mooney, G. Laske, and T.G. Masters. CRUST 5.1: A global crustal model at $5^\circ \times 5^\circ$. *Journal of Geophysical Research*, 103(B1):727–747, 1998.
- C. Nielsen and H. Thybo. No Moho uplift below the Baikal Rift Zone: Evidence from a seismic refraction profile across southern Lake Baikal. *Journal of Geophysical Research*, 114:B08306, 2009.

- A.M. Nikishin, S. Cloetingh, L.I. Lobkovsky, E.B. Burov, and A.C. Lankreier. Continental lithosphere folding in Central Asia (Part I) constraints from geological observations. *Tectonophysics*, 226:59–72, 1993.
- A. Paul, D. Hatzfeld, A. Kaviani, M. Tatar, and C. Péquegnat. Seismic imaging of the lithospheric structure of the Zagros mountain belt (Iran). *Geological Society, London, Special Publications*, 330:5–18, 2010.
- C. Petit and J. Déverchère. Structure and evolution of the Baikal Rift: A Synthesis. *Geochemistry Geophysics Geosystems*, 7(11), 2006.
- D. Plouff. Gravity and magnetic fields of polygonal prisms and application to magnetic corrections. *Geophysics*, 41(4):727–741, 1976.
- M. Pubellier, N. Chamot-Rooke, F. Ego, J.C. Guezou, E. Konstantinovskaya, A. Rabaute, J. Ali, J. Aitchison, C. Aubourg, J. Charvet, M. Fournier, R. Hbert, G. Ivanov, L. Jolivet, C. Lepvrier, G. Mascle, I. Pospelov, J.C. Ringenbach, S. Shokalsky, M. Sosson, J. Verges, and Wang C. Structural Map of Eastern Eurasia, Commission for the Geological Map of the World, 1:12.500.000 scale, 2008.
- V. Puchkov. Paleozoic evolution of the east european continental margin involved in the uralide orogeny. In D. Brown, C. Juhlin, and V. Puchkov, editors, *Mountain Building in the Uralides; Pangea to the Present*, volume 132 of *Geophysical Monograph*, pages 9–31. American Geophysical Union, 2002.
- G. Ranalli. *Rheology of the Earth; Deformation and flow processes in geophysics and geodynamics*. Allen and Unwin, Boston, MA, 1987. 366pp.
- J. Raphson. *Analysis aequationum universalis*. London, 1690.
- A. Reuss. Berechnung der Fliegrenze von Mischkristallen auf Grund der Plastizitätsbedingung für Einkristalle. *Zeitschrift für Angewandte Mathematik und Mechanik*, 9:49–58, 1929.
- J. Ritsema, A. Deuss, H. J. van Heijst, and J. H. Woodhouse. S40RTS: a degree-40 shear-velocity model for the mantle from new Rayleigh wave dispersion, teleseismic traveltimes and normal-mode splitting function measurements. *Geophysical Journal International*, 184:1223–1236, 2011.
- O. Ritzmann and J.I. Faleide. The crust and mantle lithosphere in the Barents Sea - Kara Sea region. *Tectonophysics*, 470:89–104, 2007.
- D.B. Rowley. Age of initiation of collision between India and Asia: A review of stratigraphic data. *Earth and Planetary Science Letters*, 145:1–13, 1996.
- E. Ruigrok and K. Wapenaar. Global-phase seismic interferometry unveils p-wave reflectivity below the himalayas and tibet. *Geophysical Research Letters*, 39:L11303, 2012.

BIBLIOGRAPHY

- A.M.C. Sengör, B.A. Natal'in, and V.S. Burtman. Evolution of the Altaid tectonic collage and Paleozoic crustal growth in Eurasia. *Nature*, 364:299–307, 1993.
- J.H.W. Smit, S.A.P.L. Cloetingh, E. Burov, M. Tesauro, D. Sokoutis, and M Kaban. Interference of lithospheric folding in western Central Asia by simultaneous Indian and Arabian plate indentation. *Tectonophysics*, 2013. in press.
- V.B. Sollogub, A. Guterch, and D. Prosen. *Structure of the Earths Crust in Central and Eastern Europe from Data of Geophysical Investigations*. Naukova Dumka, Kyiv, 1980. in Russian.
- F.D. Stacey. *Physics of the Earth*. Brookfield Press, Brisbane, 3rd edition, 1992.
- R. Stadlander, J. Mechie, and A. Schulze. Deep structure of the southern Ural mountains as derived from wide-angle seismic data. *Geophysical Journal International*, 137:501–515, 1999.
- W. Stolk, M. Kaban, F. Beekman, M. Tesauro, W.D. Mooney, and S. Cloetingh. High resolution regional crustal models from irregularly distributed data: Application to Asia and adjacent areas. *Tectonophysics*, 2013. in press, <http://dx.doi.org/10.1016/j.tecto.2013.01.022>.
- V.N. Strakhov, T.V. Romaniuk, and N.K. Frolova. Method of direct gravity problem solution for modeling of global and regional gravity anomalies. In *New methods of the gravity and magnetic anomaly interpretation*, pages 118–235. Institute for Physics of the Earth, 1989.
- W.M. Telford, L.P. Geldart, R.E. Sheriff, and D.A. Keys. *Applied Geophysics*. Cambridge University Press, 1981.
- M. Tesauro. *An integrated study of the structure and thermomechanical properties of the European lithosphere*. PhD thesis, VU University, Amsterdam, 2009. ISBN = 978-90-9024061-9.
- M. Tesauro, M.K. Kaban, S.A.P.L. Cloetingh, N.J. Hardebol, and F. Beekman. 3D strength and gravity anomalies of the European lithosphere. *Earth and Planetary Science Letters*, 263:56–73, 2007.
- M Tesauro, M.K. Kaban, and S.A.P.L. Cloetingh. EuCRUST-07: A new reference model for the European crust. *Geophysical Research Letters*, 35, 2008.
- M. Tesauro, M.K. Kaban, and S.A.P.L. Cloetingh. A new thermal and rheological model of the European lithosphere. *Tectonophysics*, 476(3-4):478–495, 2009.
- M. Tesauro, E.B. Burov, Kaban. M.K., and S.A.P.L. Cloetingh. Ductile crustal flow in Europe's lithosphere. *Earth and Planetary Science Letters*, 312:254–265, 2011.

- M. Tesauero, M.K. Kaban, and S.A.P.L. Cloetingh. Global strength and elastic thickness of the lithosphere. *Global and Planetary Change*, 2012. (in press) doi:10.1016/j.gloplacha.2011.12.003.
- H. Thybo and C. Nielsen. Magma-compensated crustal thinning in continental rift zones. *Nature*, 457:873–876, 2009.
- USGS. Geologic Province and Thermo-Tectonic Age Maps. <http://earthquake.usgs.gov/research/structure/crust/database.php>, 1997.
- P. Vacher, A. Mocquet, and C. Sotin. Computation of seismic profiles from mineral physics: the importance of the non-olivine components for explaining the 660 km depth discontinuity. *Physics of the Earth and Planetary Interiors*, 106:275–298, 1998.
- J.D. Van Wees, F. Van Bergen, M. Nepveu, F. Beekman, S. Cloetingh, and D. Bonté. Probabilistic tectonic heat flow modeling for basin maturations: Assessment method and applications. *Marine and Petroleum Geology*, 26: 536–551, 2009.
- M.L. Verba, L.A. Daragan-Sushchova, and A.D. Pavlenkin. Riftogenic structures of the western arctic shelf investigated by refraction studies. *International Geology Review*, 34(8):753–764, 1992.
- W. Voigt. *Lehrbuch der Kristallphysik*. Teubner, Leipzig, 1928.
- I.S. Vol’vovskii and B.S. Vol’vovskii. *Cross-sections of the earth’s crust in the territory of the USSR, plotted from deep seismic soundings*. Sovetskoe Radio, Moscow, 1975. Translated from: Razrezy Zemnoy Kory Territorii SSSR po Dannym Glubinnogo Seismicheskogo Zondirovaniya.
- H. Wackernagel. *Multivariate Geostatistics - An Introduction with Applications*. Springer, Berlin, 1995.
- J. Wallis. *A Treatise of Algebra both Historical and Practical*. London, 1685.
- K. Wapenaar and J. Thorbecke. On the Retrieval of the Directional Scattering Matrix from Directional Noise. *SIAM Journal on Imaging Sciences*, 6:322–340, 2013.
- K. Wapenaar, E. Ruigrok, J. van der Neut, and D. Draganov. Improved surface-wave retrieval from ambient seismic noise by multi-dimensional deconvolution. *Geophysical Research Letters*, 38:L01313, 2011.
- K.N. Warners-Ruckstuhl, R. Govers, and Wortel. R. Lithospheremantle coupling and the dynamics of the Eurasian Plate. *Geophysical Journal International*, 189:1253–1276, 2012.
- K.N. Warners-Ruckstuhl, R. Govers, and Wortel. R. Tethyan collision forces and the stress field of the Eurasian Plate. *Geophysical Journal International*, 2013. doi: 10.1093/gji/ggt219.

BIBLIOGRAPHY

- L.T. White and G.S. Lister. The collision of India with Asia. *Journal of Geodynamics*, 56-57:7-17, 2012.
- T.P. Yegorova and V.I. Starostenko. Large-scale three-dimensional gravity analysis of the lithosphere below the transition zone from Western Europe to the East European Platform. *Tectonophysics*, 314:83-100, 1999.
- S. Youngsheng, S.V. Krylov, Y. Baojun, L. Cai, D. Shixue, L. Tiechen, L. Jingzhi, X. Xingzhui, Z.R. Mishen'kina, G.V. Petrik, I.F. Shelud'ko, Seleznev V.S., and V.M. Solov'ev. Deep Seismic Sounding of the Lithosphere on the Baikal-Northeastern China International Transect. *Russian Geology and Geophysics*, 37:1-13, 1996.
- Z. Zhang and S. Klemperer. Crustal structure of the Tethyan Himalaya, southern Tibet: new constraints from old wide-angle seismic data. *Geophysical Journal International*, 181(3):1247-1260, 2010.
- Z. Zhang, S. Klemperer, Z. Bai, Y. Chen, and J. Teng. Crustal structure of the Paleozoic Kunlun orogeny from an active-source seismic profile between Moba and Guide in East Tibet, China. *Gondwana Research*, 19:994-1007, 2011.
- J. Zheng, S. Y. O'Reilly, W. L. Griffin, F. Lu, and M. Zhang. Nature and Evolution of Cenozoic Lithospheric Mantle beneath Shandong Peninsula, Sino-Korean Craton, Eastern China. *International Geology Review*, 40(6):471-499, 1998.
- S.M. Zverev and I.P. Kosminskaya. *Seismic models of the Lithosphere for the major geostructures on the territory of the USSR*. Publishing House Nauka, Moscow, 1980. in Russian.